Mode-Matching Analysis of Whispering-Gallery-Mode Cavities

by

Xuan Du
B.Eng., Xi'An JiaoTong University, 2010

A Thesis Submitted in Partial Fulfillment of the
Requirements for the Degree of

MASTER OF APPLIED SCIENCE

in the Department of Electrical and Computer Engineering

Mode-Matching Analysis of Whispering-Gallery-Mode Cavities

by

Xuan Du
B.Eng., Xi'An JiaoTong University, 2010

Supervisory Committee

Dr. Tao Lu, Supervisor
(Department of Electrical and Computer Engineering)

Dr. Poman So, Departmental Member
(Department of Electrical and Computer Engineering)

Supervisory Committee

Dr. Tao Lu, Supervisor
(Department of Electrical and Computer Engineering)

Dr. Poman So, Departmental Member
(Department of Electrical and Computer Engineering)

ABSTRACT

This thesis presents a full-vectorial mode matching method for whispering gallery microcavity analysis. With this technique, optical properties such as resonance wavelength, quality factor and electromagnetic field distribution of an arbitrarily shaped microcavity can be computed with high accuracy. To illustrate this, a mode matching analysis that involves a single propagating whispering gallery mode is performed on a microtoroid in the presence of individual nonplasmonic nanoparticle on its surface. This method is also extended to the analysis of cavity adsorbed by a plasmonic nanoparticle at a wavelength close to plasmon resonance where the resulting field distortion invalidates other approaches. The simulation demonstrates high efficiency and is in close agreement with experimental measurements reported in previous work. Furthermore, we extend our mode matching analysis to the case where multiple whispering gallery modes are involved in the course of light propagation. The new formalism is performed on a cavity-waveguide coupling system to investigate the light delivery from a tapered optical waveguide to a microcavity at high precision. A novel hybrid integration scheme to implement an ultra-high quality factor microcavity on a silicon-on-insulator platform is proposed based on the related modelling results.

Contents

List of Figures

ACKNOWLEDGEMENTS

I would like to express my gratitude to my supervisor Dr. Tao Lu of the University of Victoria for his encouragement, guidance and helpful suggestions through my graduate studies. I would also like to thank my colleagues WenYan Yu, Serge Vincent, Amin Cheraghi Shirazi, Niloofar Sadeghi and LeYuan Pan for their suggestions and assistance.

DEDICATION

To my family

Chapter 1

Introduction

The whispering gallery in St. Paul's Cathedral Church, London, has been known for its phantom phenomenon to deliver a whisper tens of meters away since its consecration in 1708. Such phenomenon, later explained by Lord Rayleigh [1] in 1878, is a result of low energy loss occurred during the propagation of sound wave along the gallery wall in a manner similar to light propagating in a modern optical waveguide. Thanks to the rapid advancement of micro/nano fabrication technologies, an optical mimic of the whispering gallery, named as whispering gallery mode (WGM) microcavity, has emerged as a powerful photonic device since last centaury [2, 3, 4, 5]. In an optical WGM microcavity, photons circulate along the cavity edge. When the round trip time the photon travels coincides with an integer multiple of the photon oscillation period, resonance occurs. Under the resonance condition, a WGM microcavity can confine photons within a volume as small as thousands of cubic microns in the proximity of the cavity edge for a long time typically exceeding 1 microsecond [6, 7]. In the event when a nanoparticle adsorbs to the cavity surface, the photon will travel at a longer path. This causes a detectable shift of cavity resonance wavelength. This unique feature can be utilized for nanosensing [8, 9]. In addition, it has been recently reported that a localized surface plasmon resonance (LSPR) can largely enhance the sensitivity of a microcavity [10, 11] by increasing the field intensity around bound plasmonic particles. To design and optimize such plasmonic structures on WGM cavities, numeric modelling tools are in need. In addition, light needs to be delivered to a WGM cavity through eg. a tapered waveguide [12]. An efficient and robust coupling scheme between a well-designed tapered waveguide structure and a cavity plays a critical role in integrating a cavity on a silicon photonic platform. To develop such scheme, a suitable numeric tool is also required [13].

In the past, researchers have developed several numeric tools to meet the necessity of WGM investigation. The first step in the numeric interrogation of a WGM cavity is to develop a tool that can calculate the electro-magnetic field distribution of an unperturbed whispering gallery mode and corresponding parameters such as the resonance wavelength and quality factor (Q). Such tool is known as a WGM mode solver. Up to date, a finite element method (FEM) mode solver [14] is among the most popular ones to simulate the mode of an ideal or perfectly axisymmetric WGM cavity with high accuracy while a less accurate finite different mode solver is also available for its simplicity of implementation[15, 16]. In the second step, changes of the optical properties need to be estimated when the cavity is perturbed by, eg. a nano particle or a tapered waveguide. In the case when the perturbation does not significantly alter the field distribution of an unperturbed cavity, a perturbation approach is sufficient to predict the changes [17, 18]. This technique yields highly accurate results for simulating the resonance wavelength shift caused by individual dielectric nanoparticles binding onto the surface of a mcircavity. However, it is less accurate for the design of cavity enhanced plasmonic nano-antennas, in which case the local field is strongly distorted by the local surface plasmon. Such inaccuracy is worsened when the cavity resonance wavelength is close to the resonance wavelength of the plasmonic structure on the cavity. Alternatively, one may choose first-principle techniques that directly solve Maxwell's equations in all three dimensions. However, such techniques require extensive computational resources compared to the mode solver based techniques due to the increase in grid points by one dimension.

Mode-Matching Method (MMM), typically formulated in a Cartesian coordinate system, is a computational electro-magnetics modeling technique that simulates the propagation of wave by expanding the electro-magnetic field onto the eigen modes in the local cross section. It has been widely used in modeling and designing straight waveguide discontinuities, junctions, and filters in Cartesian coordinates [19, 20]. In MMM, the optical structure is divided into a number of slices along the propagation axis (typically longitudinal). In each slice, the electromagnetic field is expanded onto a complete orthonormal set of eigen modes of the local cross section. Scattering matrix is computed by applying the continuous relation between two neighboring slices. In this work, we partition a WGM system along the azimuthal direction and obtain full-vector WGM modes at each slice. Mode matching between neighbouring slices is then performed in a cylindrical coordinate to emulate the wave propagation in the WGM cavity. Optical properties such as the resonance wavelength and quality

factor are calculated accordingly.

In this thesis, a less accurate yet highly efficient single mode-matching formulas for a whispering gallery mode-nanoparticle (WGM-NP) hybrid system is first presented. A multi-mode MMM formulas is then illustrated in the case where multiple WGMs are involved in the light propagation. With this technique, we demonstrated that a robust whispering gallery mode-silicon on insulator waveguide (WGM-SOI) coupling scheme is achievable.

1.1 Thesis Outline

The thesis is structured as follows:

Chapter 2 provides a basic theory of whispering gallery modes, their applications followed by an introduction of whispering gallery mode simulation history.

Chapter 3 demonstrates a mode-matching-method in cylindrical coordinates that involves a single WGM. An example of a WGM cavity with surface binding particles is analyzed with the developed formulation. Simulation results are presented, discussed and compared with published measurements.

Chapter 4 demonstrates a multi-mode mode-matching-method by considering the mutual coupling between modal field. A test case of a WGM-SOI waveguide system is analyzed.

Chapter 5 concludes the thesis and the main contribution to the area.

Chapter 2

Background

The term whispering gallery refers to the whispering gallery under the dome of St. Paul's Cathedral in London (Fig. 2.1(a) [21]). It is famous for the acoustic phenomenon that a whisper against any point of the gallery wall can be heard on the opposite side as far as 34 meters away. Such phenomenon has also been shown by many other monuments, such as the Temple of Heaven in Beijing and the (Fig. 2.1(b) [22]) Gol Gumbaz in Bijapur. It was first studied by Lord Rayleigh [1] and he concluded that the acoustic wave travels along the curved surface of the whispering gallery wall in a manner nowadays known as waveguiding effects. While in free space, propagating acoustic wave decays proportionally to the square of the distance, in the whispering gallery, the wave decays only directly proportionally to the distance, making it possible to be heard tens of meters away.

(a) (b)

Figure 2.1: Whispering gallery monuments. (a) The whispering gallery under the dome of St. Paul's Cathedral in London. (b) The whispering gallery of the Imperial Vault in the Temple of Heaven in Beijing.

In the 20^{th} century, electromagnetic whispering gallery mode was found in dielectric spheres and cylinders. As early as in 1980s[4], researchers started to investigate optical whispering gallery resonators and their applications [23, 24]. Light circulates inside a whispering-gallery cavity with total internal reflection. The cavity can confine light so well that a Q-factor as large as 10^8 is achievable [5, 25]. Currently, studies of whispering gallery mode cavities are on research hotbeds for their unique combination of ultra-high Q-factor, small mode volume, ease of fabrication and on-chip integration to silicon photonic platforms.

In this section, the basic theory of the whispering gallery mode is presented from a view of classic electrodynamics, followed by an introduction of the fundamental parameters of WGM optical cavities. Applications of WGM cavities and cavity enhanced localized surface plasmon hybrid sensors will be introduced. Finally, a review of the history of the simulation of the WGM cavities will be given, together with a detailed introduction of two most widely used models.

2.1 Whispering-Gallery-Mode Microcavities

2.1.1 Whispering Gallery Mode

Whispering-gallery-mode cavities confine photons for a long time (exceeding 1 microsecond [5]). The general principles of a WGM cavity can be explained by the geometrical optics. As illustrated in Fig. 2.2, WGM cavity with a refractive index n_1 is surrounded by medium with a refractive index of $n_2 < n_1$. When the light incidents at an angle larger than the critical angle defined by Snell's law:

$$\theta_c = sin^{-1}(\frac{n_2}{n_1}) \tag{2.1}$$

total internal reflection will occur and the ray will experience no loss from refraction. If the optical path length the ray travels after a full loop coincides an integer times of its free space wavelength, constructive interference occurs and high optical power will build up.

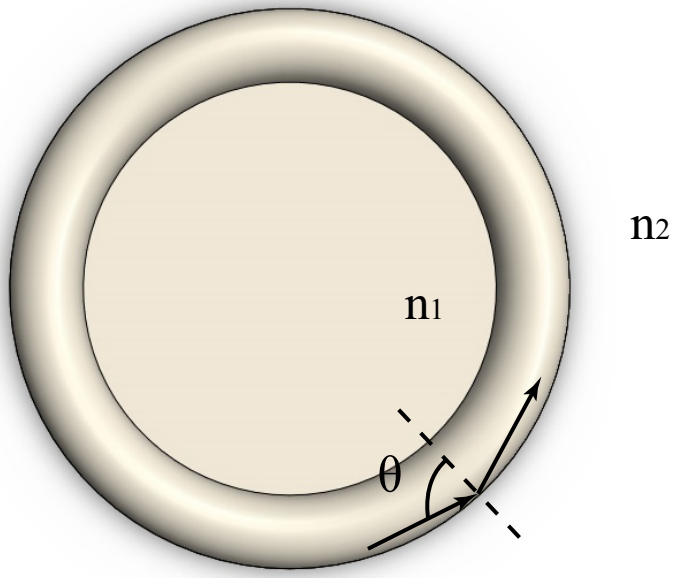

Figure 2.2: Schematic illustration of total internal reflection at the interface of a dielectric WGM cavity and the surrounding medium, as described by ray optics.

While the geometrical optics view gives an intuitive picture, a more quantitative description of the WGM is given by the Maxwell's Equations:

$$\begin{cases} \nabla \cdot \mathbf{D} = 0 & \text{(2.2a)} \\ \nabla \times \mathbf{E} = -\dfrac{\partial \mathbf{B}}{\partial t} & \text{(2.2b)} \\ \nabla \cdot \mathbf{B} = 0 & \text{(2.2c)} \\ \nabla \times \mathbf{H} = \dfrac{\partial \mathbf{D}}{\partial t} & \text{(2.2d)} \end{cases}$$

Here we assume there are no free charges and current density inside the cavity. It is demonstrated in [26] that by including the appropriate boundary conditions, the source-free Maxwell's Equations can describe a general resonator driven by sources. The electrical field $\mathbf{E}$, electrical displacement field $\mathbf{D}$, magnetic field $\mathbf{B}$, and magnetic field strength $\mathbf{H}$ in (2.2) are related to each other by the permittivity $\epsilon = \epsilon_0 \epsilon_r$ and permeability $\mu = \mu_0 \mu_r$ according to:

$$\begin{aligned} \mathbf{D} &= \epsilon \mathbf{E} \\ \mathbf{B} &= \mu \mathbf{H} \end{aligned} \tag{2.3}$$

Taking curl of (2.2b) and (2.2d) we obtain:

$$\nabla \times \nabla \times \left\{ \begin{array}{c} \mathbf{E} \\ \mathbf{H} \end{array} \right\} = -\mu\epsilon \frac{\partial^2}{\partial t^2} \left\{ \begin{array}{c} \mathbf{E} \\ \mathbf{H} \end{array} \right\} \tag{2.4}$$

Using the identities $\nabla \times \nabla \times \mathbf{A} = \nabla(\nabla \cdot \mathbf{A}) - \nabla^2 \mathbf{A}$ in the absence of external stimuli $\nabla \cdot \mathbf{D} = 0$, $\nabla \cdot \mathbf{B} = 0$, (2.4) becomes

$$\nabla^2 \left\{ \begin{array}{c} \mathbf{E} \\ \mathbf{H} \end{array} \right\} = \mu\epsilon \frac{\partial^2}{\partial t^2} \left\{ \begin{array}{c} \mathbf{E} \\ \mathbf{H} \end{array} \right\} \tag{2.5}$$

$\mathbf{E}$ and $\mathbf{H}$ are functions of time and space and can be solved by separation of variables. To illustrate this approach, we assume the field is monochromatic and the dielectric constants are independent of time,

$$\{\mathbf{E}(\vec{r}, t), \mathbf{H}(\vec{r}, t)\} = \{\mathbf{E}(\vec{r}), \mathbf{H}(\vec{r})\} \, e^{j\omega t} \tag{2.6}$$

This leads to the Helmhöltz equation:

$$\left[\nabla^2 + n^2(\vec{r}) k_0^2\right] \left\{ \begin{array}{c} \mathbf{E}(\vec{r}) \\ \mathbf{H}(\vec{r}) \end{array} \right\} = \vec{0} \tag{2.7}$$

$k_0 = \omega/c$ is the vacuum wave number and $n(\vec{r})$ is the complex refractive index profile whose imaginary part denotes material loss. We also assume all the materials are non-magnetic such that $\mu = \mu_0$. Inspired by the axisymmetry of the cavity geometry, a cylindrical coordinate system concentric with the cavity as shown in Fig.2.3 is adopted.

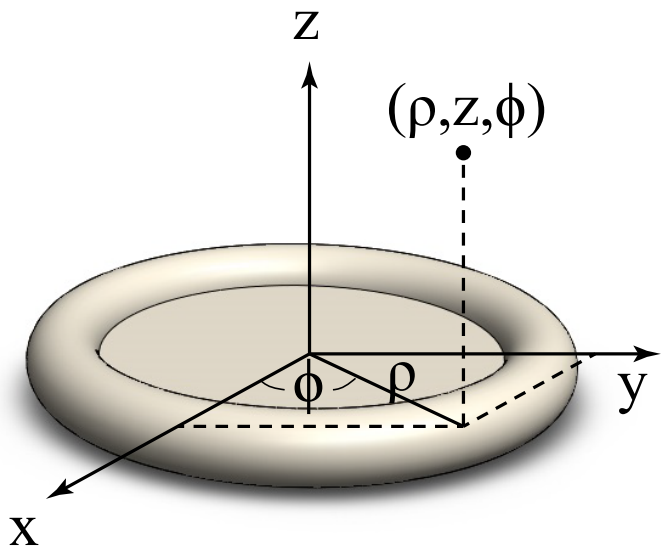

Figure 2.3: A cylindrical coordinate system used to describe the whispering gallery mode mathematically.

The Helmhöltz equation in the cylindrical coordinate system is:

$$\left[\frac{\partial^2}{\partial\rho^2}+\frac{1}{\rho}\frac{1}{\partial\rho}+\frac{1}{\rho^2}\frac{\partial^2}{\partial\phi^2}+\frac{\partial^2}{\partial z^2}+n^2(\vec{r})k_0^2\right]\left\{\begin{array}{c}\mathbf{E}(\rho,z,\phi)\\ \mathbf{H}(\rho,z,\phi)\end{array}\right\}=\mathbf{0} \tag{2.8}$$

For an ideal WGM cavity, its refractive index profile is independent of the azimuthal angle ϕ,

$$n(\vec{r})=n(\rho,z) \tag{2.9}$$

We may further separate the transverse and azimuthal dependence of the field as:

$$\left\{\begin{array}{c}\mathbf{E}(\rho,z,\phi)\\ \mathbf{H}(\rho,z,\phi)\end{array}\right\}=\left\{\begin{array}{c}\mathbf{E}(\rho,z)\\ \mathbf{H}(\rho,z)\end{array}\right\}V(\phi) \tag{2.10}$$

Substitute (2.10) into (2.8) we can obtain:

$$\frac{1}{V(\phi)}\frac{\partial^2}{\partial\phi^2}V(\phi) = \text{constant} \equiv m^2 \tag{2.11}$$

Thus, the WGM is characterized by:

$$\left\{ \begin{array}{c} \mathbf{E}(\rho,z,\phi) \\ \mathbf{H}(\rho,z,\phi) \end{array} \right\} = \left\{ \begin{array}{c} \mathbf{E}(\rho,z) \\ \mathbf{H}(\rho,z) \end{array} \right\} e^{jm\phi} \tag{2.12}$$

(2.12) is analogous to a straight waveguide mode in Cartisian coordinates: $\mathbf{E}(x,y,z) = \mathbf{E}(x,y)e^{j\beta z}$ in which case β is the propagation constant of the guiding mode along z direction. In our case, m is the azimuthal mode order, which in general is a complex number $\tilde{m} = m_r + jm_i$. The real part of m corresponds to the phase change of the mode over certain ϕ angle and the imaginary part of m corresponds to the cavity loss. Similar to the geometrical optics analysis, when m_r is an integer number $m_r = M$, mode returns to the same place with the same phase after one round trip and constructive interference will build up inside the cavity.

2.1.2 Orthogonal Condition

To demonstrate the orthogonality of WGMs, we start with the second vector Green's theorem:

$$\int [\mathbf{B}\cdot\nabla\times(\nabla\times\mathbf{A}) - \mathbf{A}\cdot\nabla\times(\nabla\times\mathbf{B})]dV = \oint [\mathbf{A}\times(\nabla\times\mathbf{B}) - \mathbf{B}\times(\nabla\times\mathbf{A})]\cdot d\mathbf{S} \tag{2.13}$$

We make the substitution,

$$\mathbf{A} = \hat{\mathbf{e}}_\nu,\ \mathbf{B} = \hat{\mathbf{e}}_\mu^* \tag{2.14}$$

$\hat{\mathbf{e}}_\nu$ and $\hat{\mathbf{e}}_\mu$ are two solutions to (2.8) and the integration in (2.13) is carried out over the entire volume.

Generally speaking, the boundary S of the problem can be divided into a perfect electric conductor (PEC) S' and a perfect magnetic conductor (PMC) S" [26],

$$\begin{array}{c} \mathbf{n}\times\mathbf{E} = \mathbf{0},\ \mathbf{n}\cdot\mathbf{H} = 0 \ on\ \text{S'} \\ \mathbf{n}\cdot\mathbf{E} = 0,\ \mathbf{n}\times\mathbf{H} = \mathbf{0} \ on\ \text{S"} \end{array} \tag{2.15}$$

On the PEC S', $\hat{\mathbf{e}}_\nu$ is normal to the surface. Thus $\hat{\mathbf{e}}_\nu \times (\nabla \times \hat{\mathbf{e}}_\mu^*)$ is tangential and the surface integral goes to zeros. On the PMC S", $\nabla \times \hat{\mathbf{e}}_\nu$, which is proportional to the magnetic field, is normal to the surface thus the integral equals to zeros as well. As a result, the surface integral on the right-hand-side of (2.13) vanishes:

$$\oint [\hat{\mathbf{e}}_\nu \times (\nabla \times \hat{\mathbf{e}}_\mu^*) - \hat{\mathbf{e}}_\mu^* \times (\nabla \times \hat{\mathbf{e}}_\nu)] \cdot d\mathbf{S} = 0 \tag{2.16}$$

On the right hand side, substitute (2.7) we obtains,

$$\int [\hat{\mathbf{e}}_\mu^* \cdot \nabla \times (\nabla \times \hat{\mathbf{e}}_\nu) - \hat{\mathbf{e}}_\nu \cdot \nabla \times (\nabla \times \hat{\mathbf{e}}_\mu^*) = \int [\hat{\mathbf{e}}_\mu^* \cdot \frac{\omega_\nu^2}{c^2} \epsilon_r \hat{\mathbf{e}}_\nu - \hat{\mathbf{e}}_\nu \cdot \frac{\omega_\mu^2}{c^2} \epsilon_r \hat{\mathbf{e}}_\mu^*] dV \tag{2.17}$$

where ω_μ and ω_ν are the angular eigen-frequencies of the two modes and $\epsilon_r = n^2$ is the relative permittivity profile. By Combining (2.16) and (2.17) we reach:

$$\frac{\omega_\nu^2 - \omega_\mu^2}{c^2} \int \epsilon_r \hat{\mathbf{e}}_\nu \cdot \hat{\mathbf{e}}_\mu^* dV = 0 \tag{2.18}$$

and conclude that,

$$\int \epsilon_r \hat{\mathbf{e}}_\nu \cdot \hat{\mathbf{e}}_\mu^* dV = 0, \ \omega_\nu \neq \omega_\mu \tag{2.19}$$

Mode patterns with different eigen-frequencies are orthogonal in the sense of (2.19). If there is a case that two modes have the same eigen-frequency ω, it is called degeneracy. However, one can always construct an orthogonal mode set even in a degenerate case by linearly combining the degenerate modes. The orthogonal mode set can be further normalized so that the energy stored in each mode is unity. Finally, the orthonormality of the WGMs are expressed as,

$$\frac{1}{2} \int \epsilon_r \epsilon_0 \hat{\mathbf{e}}_\nu \cdot \hat{\mathbf{e}}_\mu^* = \delta_{\nu\mu} \tag{2.20}$$

2.1.3 Resonator Parameters

Quality Factor

Quality factor is one of the most important parameters that describes the performance of any resonators. It is a dimensionless parameter that describes the loss property:

$$Q = \omega_0 \frac{\text{Energy Stored}}{\text{Power Loss}} = \omega_0 \tau = \frac{\omega_0}{\Delta\omega_{FWHM}} \tag{2.21}$$

ω_0 is the resonance angular frequency and τ is the cavity ring down lifetime (the amount of time it takes for the field intensity inside the cavity to decay by a factor of e). $\Delta\omega_{FWHM} = 1/\tau$ is the full width at half maximum of the resonance peak that describes the linewidth or the 'uncertainty' of the resonance frequency.

Usually, a Q-factor between 10^3 and 10^6 is called a 'high Q-factor' and a Q-factor larger than 10^7 (which was predicted [27] and observed [28] for optical WGM micro-resonators) is called 'ultra-high'.

(2.21) can be interpreted in several ways. Firstly, Q-factor measures the characteristic time of the exponential field decay in terms of the oscillation time. This means that for higher Q-factors energy can be stored in the cavity for a longer time.

On the other hand, Q-factor quantifies the field intensity stored inside the cavity at equilibrium in terms of the power pumped into the resonator from an external source in the time of one full oscillation. This means for a higher Q-factor, with the same pumping power level one can achieve higher circulating field intensity. Ultra-high Q optical resonators can thus possess extremely strong field intensity even with moderate pumping power (in the range of milliwatts) which provides an optimistic way to study extreme nonlinear optical effects.

Q-factor is a description of the loss mechanism of the cavity. Field attenuation, on the other hand, can also be described by complex refractive indices or, in terms of the WGM characteristic equation (2.12), by complex angular frequencies $\hat{\omega}$ or complex mode numbers $\hat{m}$ [29, 30],

$$Q = \frac{\text{Re}[\tilde{\omega}]}{2\text{Im}[\tilde{\omega}]} = \frac{\text{Re}[\tilde{m}]}{2\text{Im}[\tilde{m}]} \tag{2.22}$$

The Q factor of a WGM resonator can be decomposed into the contribution from different loss mechanisms,

$$\frac{1}{Q_{total}} = \frac{1}{Q_{abs}} + \frac{1}{Q_{rad}} + \frac{1}{Q_{sc}} + \frac{1}{Q_{ss}} + \frac{1}{Q_{coup}} \tag{2.23}$$

where Q_{total} is the total Q factor. Terms in (2.23) are known as follows.

Q_{abs} comes from the absorption loss, or material loss that arises from the intrinsic absorption of electromagnetic wave from the medium. For WGM cavities with relative large diameters (around 100 μm) as are mostly used in our lab, Q_{abs} is demonstrated

to be the most critical factor to the total Q-factor [13]. Q_{abs} can be quantified by [13],

$$Q_{abs} = \frac{w\pi n}{\lambda\alpha} \tag{2.24}$$

where α is the attenuation coefficient of the material. For silica ring resonators, material loss from silica is at a low level. The attenuation coefficient of fused silica is 6 dB/km at a 633-nm wavelength and 0.35 dB/km at a 1550-nm wavelength (left axis of Fig. 2.4). WGM micro-resonators in air were demonstrated to be able to reach a Q factor as high as 10^{10} at a wavelength of 633-nm [27] under ideal condition. In reality, however, due to the moisture layer developed at the cavity surface, Q may drop to below 10^9 under lab condition. When the resonator is placed in aqueous solution, the Q-factor will further drop as a result of enhanced absorption by surrounding (cf. Fig. 2.4). Typically, the highest Q-factor of a WGM microcavity in water is around 10^8 at a 633-nm wavelength and several 10^6 at a 970-nm wavelength.

Q_{rad}, known as the radiation loss or bending loss, arises from the fact that the total internal reflection at the curved interface is never complete and will result in a transmitting mode on the low refractive index side. Q_{rad} is strongly related to the radius of the cavity. Usually a larger cavity radius results in smaller radiation loss and thus larger Q_{rad}.

Q_{sc} is the quality factor that origins from the surface contamination (for example due to adsorbed water layer). Q_{ss} is the surface scattering loss due to surface imperfection in the form of surface roughness.

Q_{abs}, Q_{rad}, Q_{sc}, and Q_{ss} together make the intrinsic Q-factor of the cavity and $Q_{coupling}$ is usually known as the external Q-factor. $Q_{coupling}$ corresponds to the loss the system suffers when coupled to an external mode (i.e. a waveguide that delivers light in and out of the cavity).

Mode Volume

Mode volume is defined as the ratio of the total energy stored inside the cavity and the maximum of the energy intensity [29]. It approximates the volume of the space that photons are packed at the edge of the cavity.

$$V = \frac{\int \epsilon \mathbf{E} \cdot \mathbf{E}^* dV}{\max\{\epsilon \mathbf{E} \cdot \mathbf{E}^*\}} \tag{2.25}$$

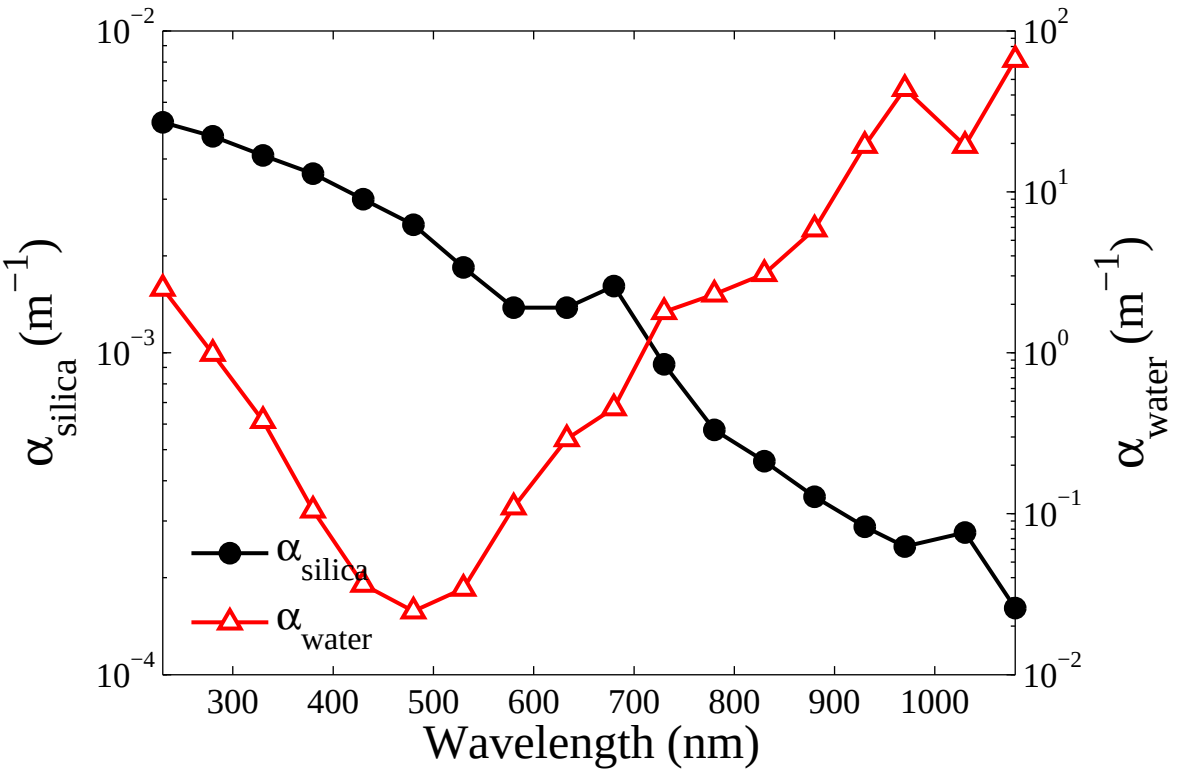

Figure 2.4: Attenuation Coefficients of silica (left) and water (right).

Mode volume is related to the lasing characteristics of a resonator as both the spontaneous emission and the stimulated emission is inversely proportional to the mode volume [31]. A small mode volume is desirable for biosensing applications.

2.2 Optical Coupling

The most commonly used input/output coupling scheme for WGM cavities is evanescent coupling. Evanescent coupling is achieved by placing a waveguide structure that possesses evanescent field close to the cavity so that the light tunnels to the cavity as shown in Fig. 2.5. Evanescent coupling can be much more efficient than free wave coupling. The most efficient way to evanescently couple light with a WGM resonator is by using a tapered fiber [32, 12]. A tapered fiber is an optical fiber that is thinned in one part (in the coupling region) through a process of heating and stretching.

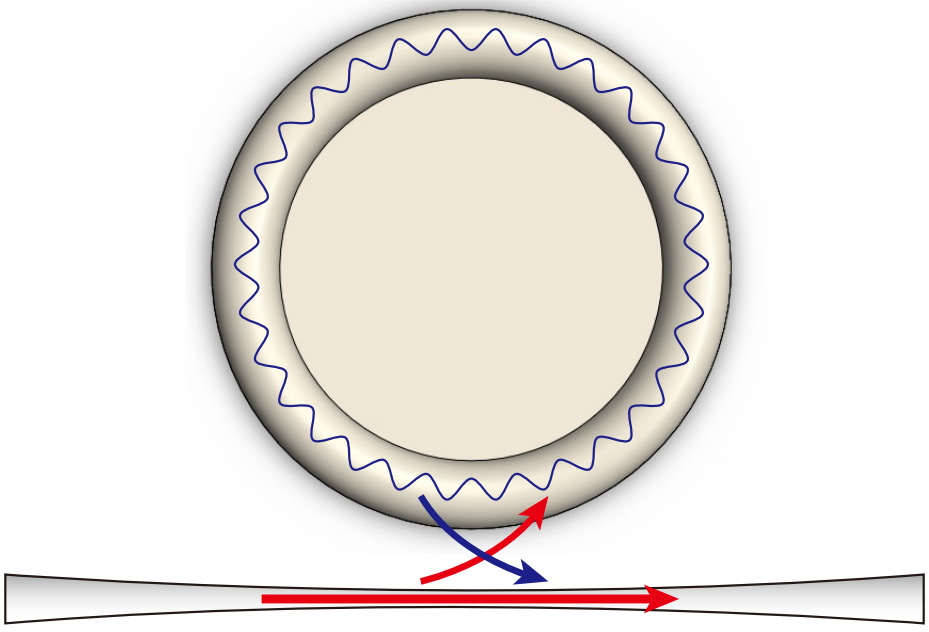

Figure 2.5: A schematic drawing of evanescent coupling between an optical fiber and a ring resonator.

Additionally, the critical coupling condition has to be satisfied to gain efficient coupling. The condition of critical coupling is a fundamental property of a matched waveguide-cavity system which requires that the intrinsic loss of the cavity equals to the coupling loss. This way at the output end a transmission of zeros will be observed

when the cavity is on resonance and all the power pumped to the waveguide will be coupled to the cavity.

2.3 Localized Surface Plasmon

2.3.1 Surface Plasmon Polaritons

Surface plasmon polaritons (SPPs) are commonly described as an electromagnetic excitation that propagates along the interface between a metal and a dielectric. Fig. 2.6 shows a popular schematic of SPPs. z>0 is filled with a dielectric with a permittivity of ϵ_d while the other half space is filled with a metal of ϵ_m. In the visible regime, ϵ_m is a complex number with a negative real part $Re[\epsilon_m] < 0$. The imaginary part of ϵ_m is small compared with its real part, standing for the lossy property of metal that arises from free-electron and interband damping [33]. For a typical metal that is going to be under investigation in this work, gold, the relative permittivity at a 633-nm wavelength is $-11.753 + 1.260j$ [34]. Thus there is a flip of sign of the real dielectric constant across the metal-dielectric interface which will cause a phase change of π. The SPP arises from the coupling of the electromagnetic wave to the oscillation of the conductor's electron plasmons. As shown in Fig. 2.6, the free electrons in the metal creates a positive and negative charge distribution and forms a polarized propagating wave. SPPs exist only for TM polarization [35].

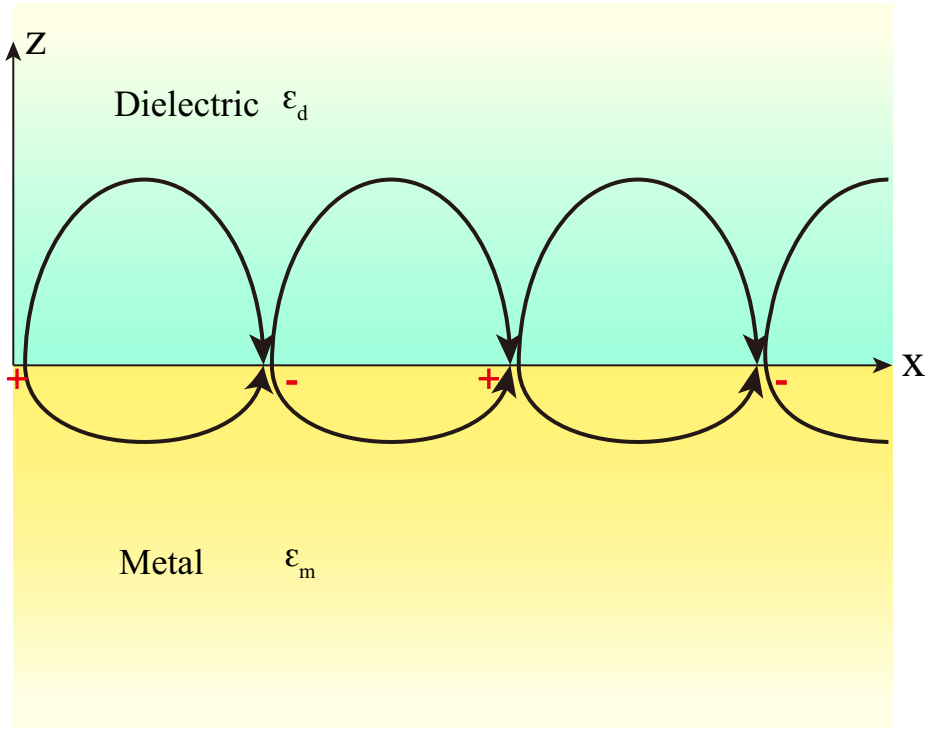

Figure 2.6: Schematic illustration of a surface plasmon polariton along the interface of a metal and a dielectric

Assuming the TM mode has only a y magnetic component, it can be obtained by solving the Helmhöltz equation (2.7) along the interface [33]:

$$\begin{aligned} H_y(x,z,t) &= e^{j\beta x - k_d x} e^{j\omega t}, \quad z > 0 \\ H_y(x,z,t) &= e^{j\beta x + k_m x} e^{j\omega t}, \quad z < 0 \end{aligned} \tag{2.26}$$

where $k_{d,m}$ is the decaying term of the wave away from the interface and β is the propagation constant along the interface. The rest of the field (The E field) can be solved combining (2.26) and the Maxwell's equations (2.2). The expression of the propagation constant β is called the dispersion relation of SPPs [35],

$$\beta = k_0 \sqrt{\frac{\epsilon_m \epsilon_d}{\epsilon_m + \epsilon_d}} \tag{2.27}$$

(2.27) describes a propagating mode for $\epsilon_m < -\epsilon_d$, neglecting the small imaginary part of ϵ_m. The propagation constant β gives an effective refractive index, $n_{eff} = \beta/k_0$ that is larger than that of the dielectric. This indicates that the wavelength of an SPP is smaller than that of a plane wave in the dielectric. In the limit of considering only a negative, real ϵ_m, β approaches infinite when $\epsilon_m + \epsilon_d$ reaches 0. In such a

case, the mode has a group velocity of 0 and can be viewed as electrostatic, called surface plasmon (SP). In a real case that ϵ_m is complex, traveling SPPs are damping. The propagation length is $L = (2Im[\beta])^{-1}$ [33], commonly $10 \sim 100$ μm in visible regime [33].

2.3.2 Localized Surface Plasmons

While SPP is a propagating electromagnetics wave coupled to the electron plasmons of the conductor, localized surface plasmon (LSP) is the non-propagating excitation of electrons coupled to the electromagnetic field. LSP can arise naturally from the scattering problem of nano-scale metal particles. Fig. 2.7 shows the scattering problem of a nano-scale metallic sphere with a radius a placed in a homogeneous isotropic dielectric medium. The permittivity for the medium and for the sphere are ϵ_m and ϵ_p respectively. Again, ϵ_p is a dispersive complex number with a negative real part. Such a nano-scale optical scattering problem of a sphere can be solved analytically by applying the quasi-static approximation, provided that $a << \lambda$. When the particle size is much smaller than the wavelength, the phase difference of the harmonically oscillating electromagnetic field across the particle can be neglected. Thus the scattering problem can be simplified as an electrostatic problem to solve the Laplace equation of the electric potential (2.28). The quasi-static approximation is adequate for nano-scale particles of sizes below 100-nm.

$$\begin{aligned} \nabla^2 \Phi &= 0 \\ \mathbf{E} &= -\nabla \Phi \end{aligned} \tag{2.28}$$

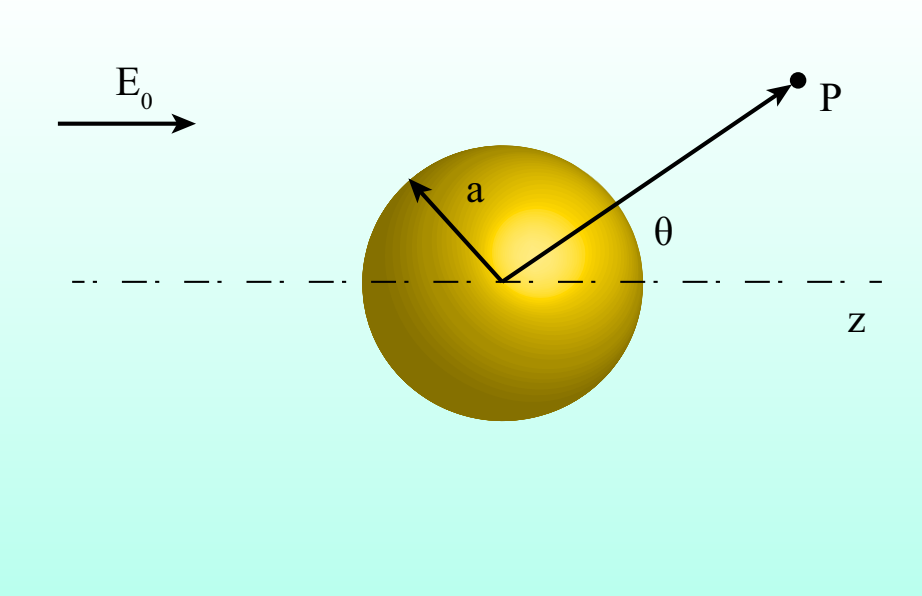

Figure 2.7: Schematic illustration of a nanosphere placed in an electrostatic field

The harmonic time dependence can then be added to the calculated field distribution. In Fig. 2.7 we assume the bead is placed in a static electric field $\mathbf{E}_{in} = E_0\hat{\mathbf{z}}$ and is located at the origin. Taking advantage of its geometrical symmetry and applying the continuous relation at the metal dielectric interface, (2.28) has the following solutions [36],

$$\begin{cases} \Phi = -\dfrac{3\epsilon_m}{\epsilon_p + \epsilon_m} E_0 r cos\theta, \quad r \leq a & \text{(2.29a)} \\ \Phi = -E_0 r cos\theta + \dfrac{\epsilon_p - \epsilon_m}{\epsilon_p + 2\epsilon_m} E_0 a^3 \dfrac{cos\theta}{r^2}, \quad r > a & \text{(2.29b)} \end{cases}$$

We notice that $\Phi_{r>a}$ describes the superposition of the input field and a dipole placed at the center of the sphere. The dipole moment $\mathbf{p}$ can be achieved by rewriting (2.29b) as,

$$\begin{cases} \Phi = -\mathbf{E}_{in} \cdot \mathbf{r} + \dfrac{\mathbf{p} \cdot \mathbf{r}}{4\pi\epsilon_m r^3}, \quad r > a & \text{(2.30a)} \\ \mathbf{p} = 4\pi\epsilon_m a^3 \dfrac{\epsilon_p - \epsilon_m}{\epsilon_p + 2\epsilon_m} \mathbf{E}_{in} & \text{(2.30b)} \end{cases}$$

Thus a dipole moment arises inside the sphere upon the applied field. Introducing

the definition of excess polarizability α,

$$\mathbf{p} = \alpha \mathbf{E} \tag{2.31}$$

we obtain,

$$\alpha = 4\pi\epsilon_m a^3 \frac{\epsilon_p - \epsilon_m}{\epsilon_p + 2\epsilon_m} \tag{2.32}$$

In (2.32) the real parts of ϵ_p and ϵ_m are opposite in sign and the imaginary part of $[\epsilon_p]$ is negligible, we can see that the excess polarizability α will reach a resonance when $\mathrm{Re}[\epsilon_p(\omega)] = -2\epsilon_m$. Fig. 2.8 and Fig. 2.9 shows the calculated spectral excess polarizabilities of a gold and silver spheres with 25-nm radii in water using (2.32). The optical constants of gold and silver are taken from [34] and that of water is taken from [37]. The curve of the gold bead experiences a maximum around 540-nm wavelength while that of the silver gold bead has a peak around 380-nm. The LSP resonance of a gold bead in water is located closer to the visible regime. The LSP resonance is independent of the size of the particle.

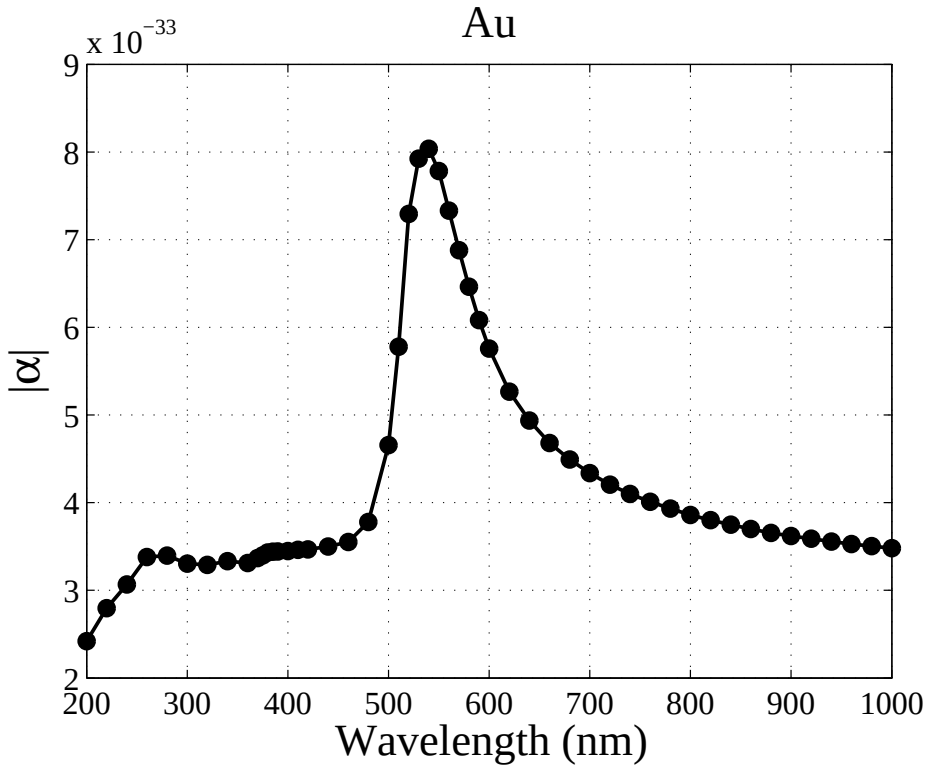

Figure 2.8: The excess polarizability of a gold nanosphere at different wavelengths.

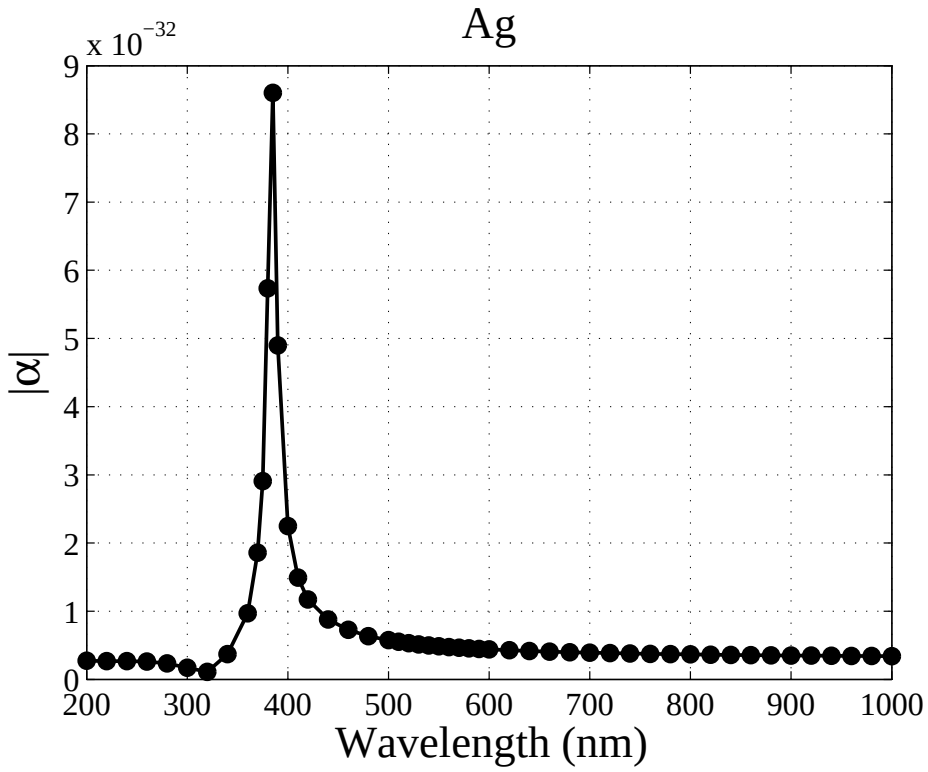

Figure 2.9: The excess polarizability of a silver nanosphere at different wavelengths.

A full-vector FEM simulation of the optical scattering of a 25-nm radius gold bead in water at a 540-nm wavelength is displayed in Fig. 2.10. Fig. 2.10(a) shows the modeling of the bead. The gold bead is placed at the origin and surrounded by water. A perfectly matched layer (PML) is placed outside the computing window (computing sphere in this case) to absorb any outgoing wave. A plane wave $\mathbf{E}_{in} = \hat{\mathbf{z}}\exp[j(\omega t+\beta y)]$ illuminates the computing window. The electric field intensity $|\mathbf{E}|^2$, the transverse electric field E_z and E_x are displayed in Fig. 2.10(b), (c) and (d), respectively. The longitudinal electric field component E_y is much smaller than the transverse field thus is not plotted in the figure. It can be seen from Fig. 2.10(b) that the field at the surface of the bead is enhanced about 7 times with respect to the incident wave. Such enhancement can be further amplified by cascading smaller and smaller particles and over 1,000 times electric field enhancement has been calculated in previous work [38].

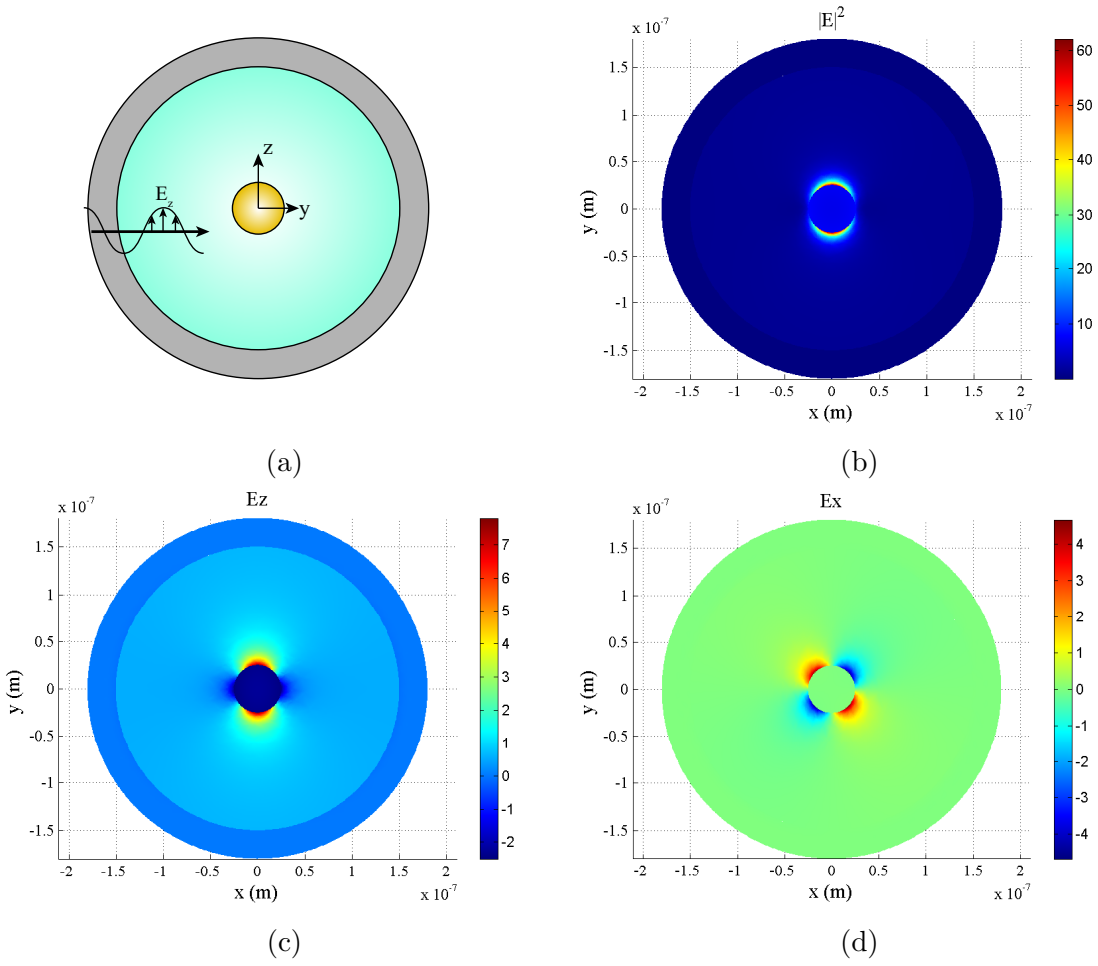

Figure 2.10: (a) 3-D modeling of a 25-nm radius gold bead sitting in water. A PML is set up at the outer boundary of the computing window to absorb outgoing waves. (b)(c)(d) Scattering patterns (electric field intensity $|E|^2$, transverse field components E_z and E_x, respectively) of the gold bead when a plane wave $\mathbf{E}_{in} = \hat{\mathbf{z}}\exp[j(\omega t + \beta y)]$ illuminates the bead.

2.3.3 Cavity Enhanced Surface Plasmons

As shown in previous sections, SPPs and LSP are evanescently bound to the surface of metal and they are extremely sensitive to surface perturbation. SPPs and LSP can be used to detect the molecular adsorption to the surface. SPP resonance sensing has been widely used in chemical and biological species detection [39]. Meanwhile, LSP resonance sensing has small detection volume and is able to detect local environment. This also reduces the limit of its application and gives greater flexibility [40].

On the other hand, the fact that SPP and LSP strongly enhance the near-field

intensity on a metal conductor surface makes them widely applicable in areas such as nonlinear optics [41], surface Raman-enhanced Raman spectroscopy [42, 43], optical trapping and manipulation [44], and enhanced fluorescence and absorption [45].

In order to detect individual aqueous-borne bio-nanoparticles such as virus and protein (10-nm size), recently it has been proposed to combine LSPs with an ultra-high Q whispering-gallery mode sensor to enhance the detection signal [46, 11]. A hybrid photonic-plasmonic whispering-gallery mode occurs when a plasmonic nanoparticle 'antenna' bound to the cavity surface and the cavity is tuned close to plasmon resonance of the nano antenna. While the cavity still maintains a high Q factor (10^6) [47, 10], the nano antenna creates hot spots that attract the bio-nanoparticle in the solution [48, 46]. Due to the strong local field enhancement of the LSP, the bound bio-nanoparticle will be more strongly polarized compared to a 'pure' WGM sensor and a more significant resonance shift of the hybrid cavity will be witnessed. Currently, most commonly used nano antenna configurations for hybrid WGM-LSP biosensors are gold nanospheres and silica-core gold nanoshells. Gold nanospheres are easy to prepare and a sensitivity enhancement of $4 - 9 \times 10^4$ is predicted [49]. On the other hand, the LSP resonance of a plasmonic nanoshell with a dielectric core is tunable by the shell thickness thus more flexibility can be achieved [50].

2.4 WGM Cavity Analysis Techniques

Experiments are related to physics laws, which are expressed in terms of equations. On the other hand, computational simulations of the equations can predict the properties of an unrealized experiment and largely reduce the experimental effort.

There have been efforts to simulate the WGM cavities for decades. By 'separating the variables', one can obtain analytical solutions of WGM cavities of certain shapes, like spherical [51] and cylindrical WGM cavities [52]. For an arbitrary shaped axisymmetric cavity, one has to solve the Maxwell's equations (2.2) numerically. Several numerical techniques have been developed so far to accurately simulate the WGM cavities including, 1) the finite difference time domain (FDTD) method [53], 2) the boundary element method (BEM) [54, 55, 56, 57, 58], 3) the Ritz-Rayleigh variational methods [59, 60], and 4) the generalized Lorenz-Mie theory method [18].

The finite element method (FEM) is a numerical technique to transform the partial differential equation into a set of linear algebraic equations to obtain approximate solutions. Since the method first came out in 1943 by Courant [61] and first applied

to microwave engineering in 1969 [62], it has become a powerful numerical technique in computational electromagnetics. Nowadays, FEM is widely used as a design tool for antennas and microwave devices.

With the transverse approximation, solutions of the WGMs can be obtained using FEM by solving the scalar Helmhöltz equation [63]. Under such approximation, the field (either the electric field or the magnetic field) is assumed to be polarized along the rotational axis of the cavity ($\hat{\mathbf{z}}$ direction). Since then, efforts have also been made for more accurate, full-vector solutions [64, 65]. Taking advantage of the azimuthal dependence of a WGM, $\mathbf{E}(\rho, \phi, z) = \mathbf{E}(\rho, z)e^{jM\phi}$, the modal can be reduced to 2D and thus is highly efficient.

In this section, the mode analysis method of a widely used full-vector weak-form FEM modal proposed by Mark Oxborrow [14] for a perfectly axisymmetric dielectric cavity is going to be introduced. The model can be easily configured in a commercial software COMSOL Multiphysics. An example of simulating a silica microtoroid in water (as in our lab environment) will be presented.

Furthermore, the wave analysis methods developed for WGM cavities with an axial asymmetry will be introduced. An example of the first order perturbation method, which will be used as a comparison in later chapters, will be demonstrated in details.

2.4.1 Mode Analysis Techniques

In this section, we consider the perfectly axial-symmetric whispering-gallery-mode cavities with an example of a microtoroid (Fig. 2.11) sitting in aqueous environment that possesses no defections (slightly elliptical shape, surface roughness, etc.).

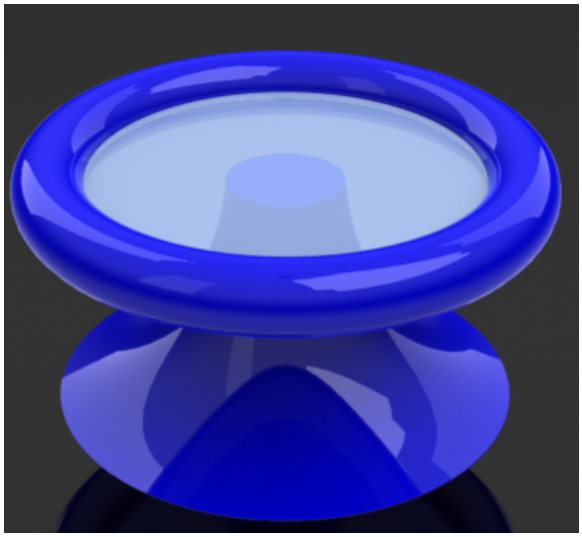

Figure 2.11: A silica toroidal microcavity with a perfect axial symmetry.

The electromagnetic field inside the cavity is governed by the sourceless Maxwell's equations (2.2). The cavity material and its surrounding medium is assumed to be isotropic and non-magnetic. As a result, the magnetic field across all the interfaces is continuous and it is more convenient to solve for the magnetic field $\mathbf{H}$. $\mathbf{H}$ is governed by the Helmhöltz equation (2.7),

$$\nabla \times (\frac{1}{\epsilon_r}\nabla \times \mathbf{H}) - \alpha\nabla(\nabla \cdot \mathbf{H}) + \frac{1}{c^2}\frac{\partial^2 \mathbf{H}}{\partial t^2} = 0 \tag{2.33}$$

where ϵ_r is the relative permittivity. An extra term $-\alpha\nabla(\nabla \cdot \mathbf{H})$ is the penalty term to suppress the spurious solutions. Spurious solutions are a set of fake modes that arise in FEM simulation from the 'local gauge invariance' [66], a feature of the curl operator. Spurious modes are found to have non-zero magnetic divergences [67], thus the magnetic divergence term $\nabla \cdot \mathbf{H}$ is used to suppress the spurious solutions. The constant α acts as the weight of the penalty term with reference to the other two terms.

Then Galerkin's method of weighted residuals is used by introducing a 'test' field strength $\tilde{\mathbf{H}}^*$. Dot product (2.33) with $\tilde{\mathbf{H}}^*$ and perform a volume integral over the whole space one obtains,

$$\int_V [(\nabla \times \tilde{\mathbf{H}}^*)\frac{1}{\epsilon_r}(\nabla \times \mathbf{H}) - \alpha(\nabla \cdot \tilde{\mathbf{H}}^*)(\nabla \cdot \mathbf{H}) + \frac{1}{c^2}\tilde{\mathbf{H}}^* \cdot \frac{\partial^2 \mathbf{H}}{\partial t^2}]dV = 0 \tag{2.34}$$

For a whispering-gallery-mode, **H** can be written in the form of,

$$\mathbf{H}(\mathbf{r}) = e^{jM\phi}\{H_\rho(\rho, z), jH_\phi(\rho, z), H_z(\rho, z)\} \tag{2.35}$$

That is to say, there are three unknown quantities to be solved on the $\rho - z$ plane. The problem is reduced from 3-D to 2-D. As the azimuthal component is 90 degrees out of phase with the transverse components, an extra $j \equiv \sqrt{-1}$ is inserted to the H_ϕ term so all the solved quantities are real. By substituting (2.35) into (2.34) we got the scalar partial differential equations need to be solved which are ready for a direct configuration into the commercial software COMSOL Multiphysics.

In COMSOL, the piecewise inhomogeneous refractive index profile is defined by setting different sub-domains. The physical constants (refractive indices, optical constants, attenuation coefficients, etc.) as well as the governing equations of each domain are configured individually. Besides, one need to define the boundary conditions of the structure. As shown in Fig. 2.12. Geometry boundaries are divided into segments with labels. Continuous boundary condition is applied to the silica-water interface 4, 6, 9, 10, 11 and 12. For the computing window boundaries 1, 2, 3, 5, 7, and 8, a 'radiation match' boundary condition [14] is applied. Alternatively, one can use a perfectly matched layer (PML) [68] to absorb the outgoing waves when necessary.

When the modal is configured properly and ready to be solved, the whole structure will be broken down into triangular meshes (Fig. 2.13). Since the accuracy of FEM is associated with the approximate representation of the solution on the mesh, adaptive mesh is adopted to optimize the mesh size and element orders to improve modal accuracy and efficiency. First, an initial mesh is generated. Then the refined mesh is created by solving the PDE on the initial mesh. When solving the PDE, the residuals in the equations are computed for all mesh elements. A refinement of the mesh is generated based on the local error indicator. The aim is to refine the mesh most where errors are largest. Fig. 2.13(b) shows a typical adaptive mesh solution by COMSOL based on the fundamental WGM mode of the toroid.

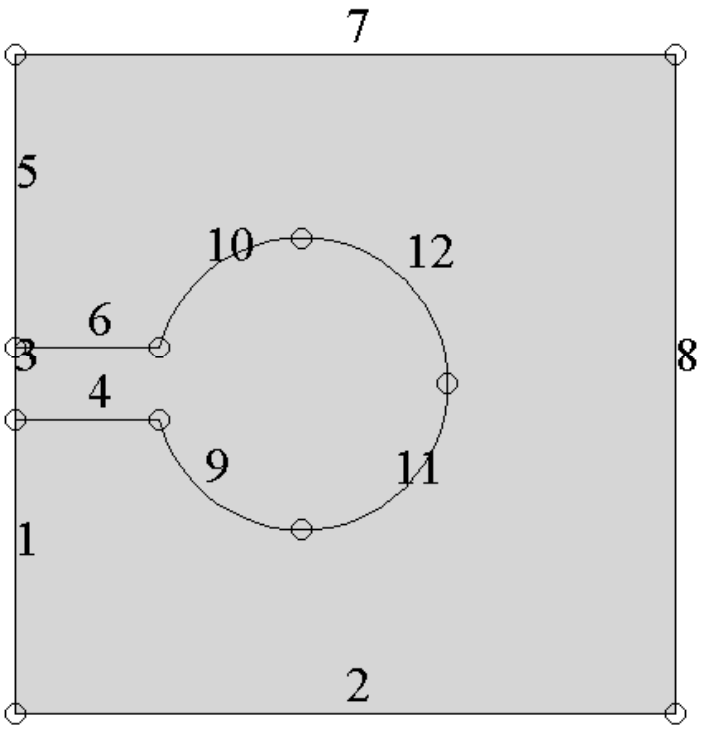

Figure 2.12: Geometric representation of the toroid in COMSOL. The whole structure including the computing window is divided into 2 sub-domains and the boundary is divided into 11 segments.

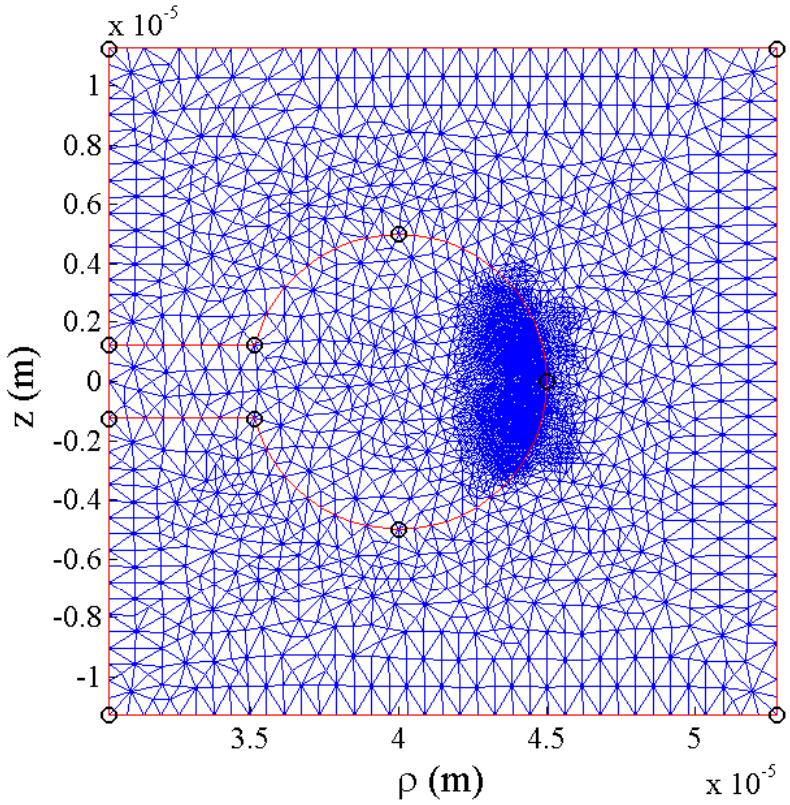

Figure 2.13: An adaptive mesh solution of a microtoroid by COMSOL Multiphysics.

The silica microtoroid under investigation has a major radius of 40-μm and a minor radius of 5-μm. The surrounding environment is filled with water. The system is simulated over a spectrum from 230-nm to 1080-nm. Complex refractive indices of silica and water are adopted [69, 37] to represent the lossy property of the materials. The computation time and resources it takes depends on the setting of the mesh scheme. Denser mesh scheme returns solutions with higher accuracy but in turn consumes more computing resources and time. Optimized by the adaptive mesh, one typical run with 4 mesh refinements and a total mesh element number of 6296 takes about 1 min on a conventional computer with 1.73 GHz CPU and 4 GB memory.

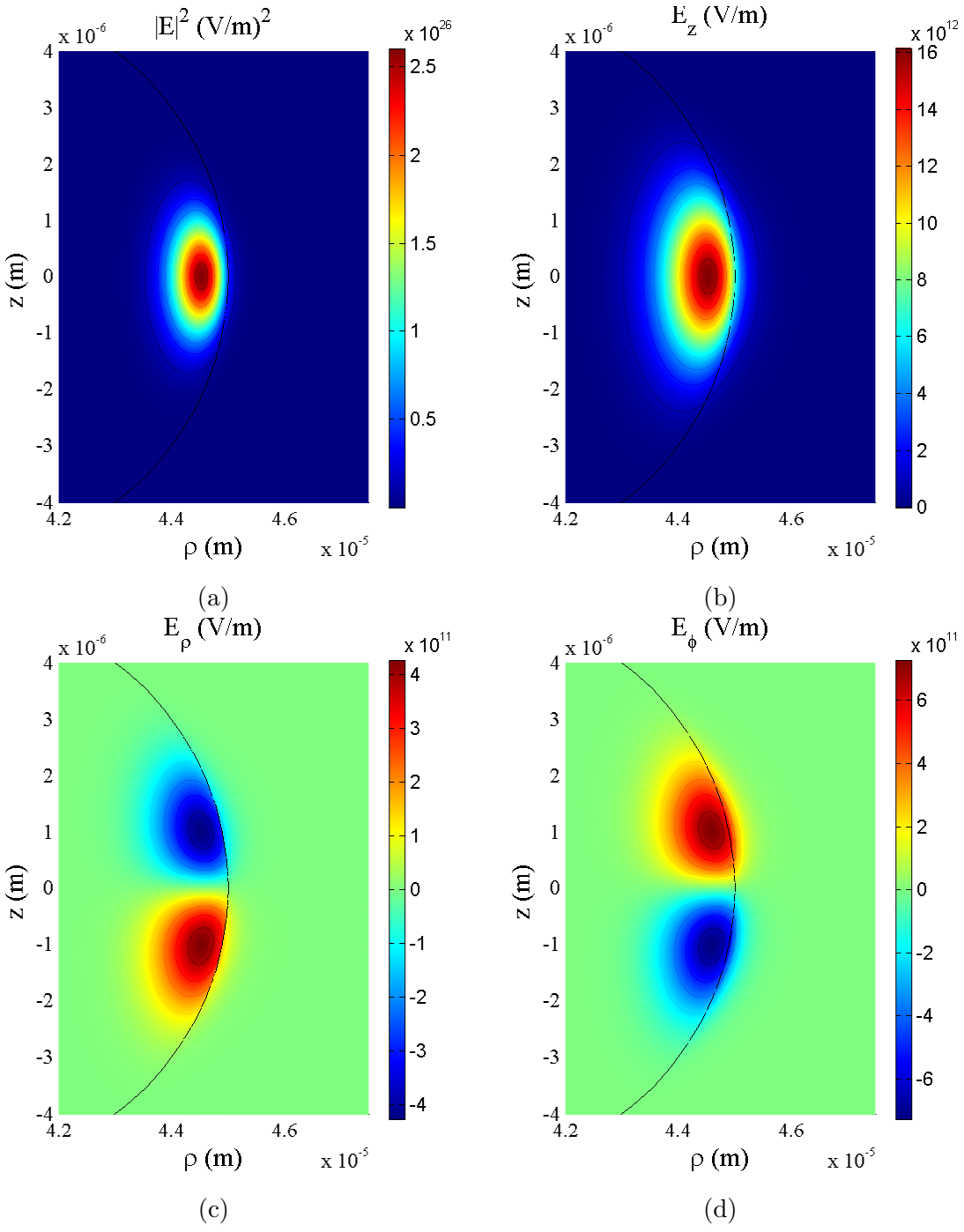

Figure 2.14: The 636^{th} fundamental quasi-TE mode of a microtoroid with a resonant wavelength of 632.74-nm: (a) Electric field intensity $|\mathbf{E}|^2$. (b) axial electric field component E_z. (c) radial electric field component E_ρ. (d) azimuthal electric field component E_ϕ.

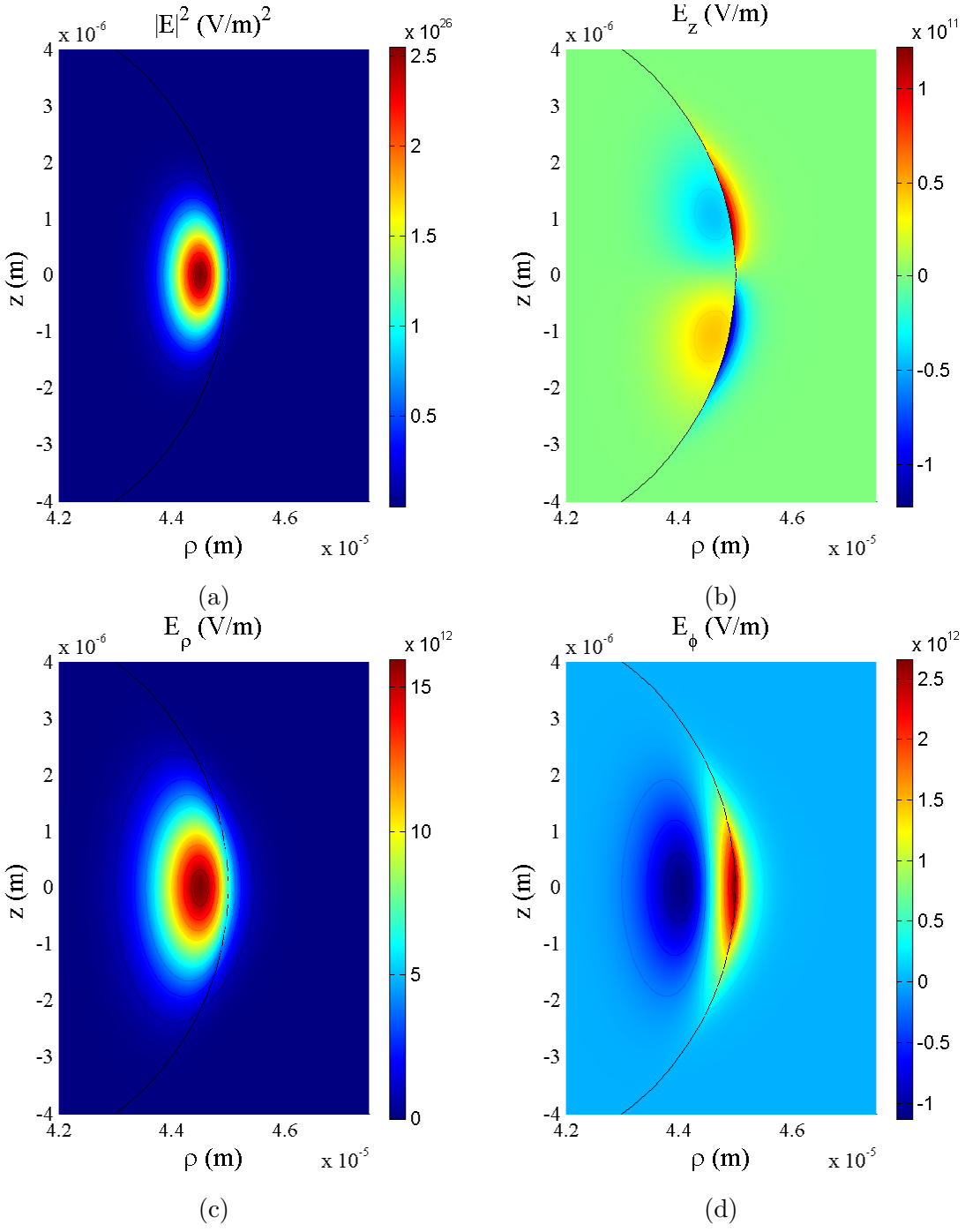

Figure 2.15: The 636^{th} fundamental quasi-TM mode of a microtoroid with a resonant wavelength of 632.41-nm: (a) Electric field intensity $|\mathbf{E}|^2$. (b) axial electric field component E_z. (c) radial electric field component E_ρ. (d) azimuthal electric field component E_ϕ.

The returning of the mode solver is a set of modes corresponding to the given

mode order M. Fig. 2.14 and Fig. 2.15 show the mode patterns of the 636^{th} fundamental modes with the electric field intensity ($|\mathbf{E}|^2$) distribution as well as all three electric field components E_z, E_ρ and E_ϕ. The displayed mode patterns are normalized according to (2.20). Both of the fundamental modes have small azimuthal components (carrying power smaller than 0.1%) and are called fundamental quasi-TE and fundamental quasi-TM modes respectively. The fundamental quasi-TE mode has an electric field mainly polarized along the rotational axis ($\hat{\mathbf{z}}$ direction), while the fundamental quasi-TM mode has a magnetic field mainly polarized along $\hat{\mathbf{z}}$.

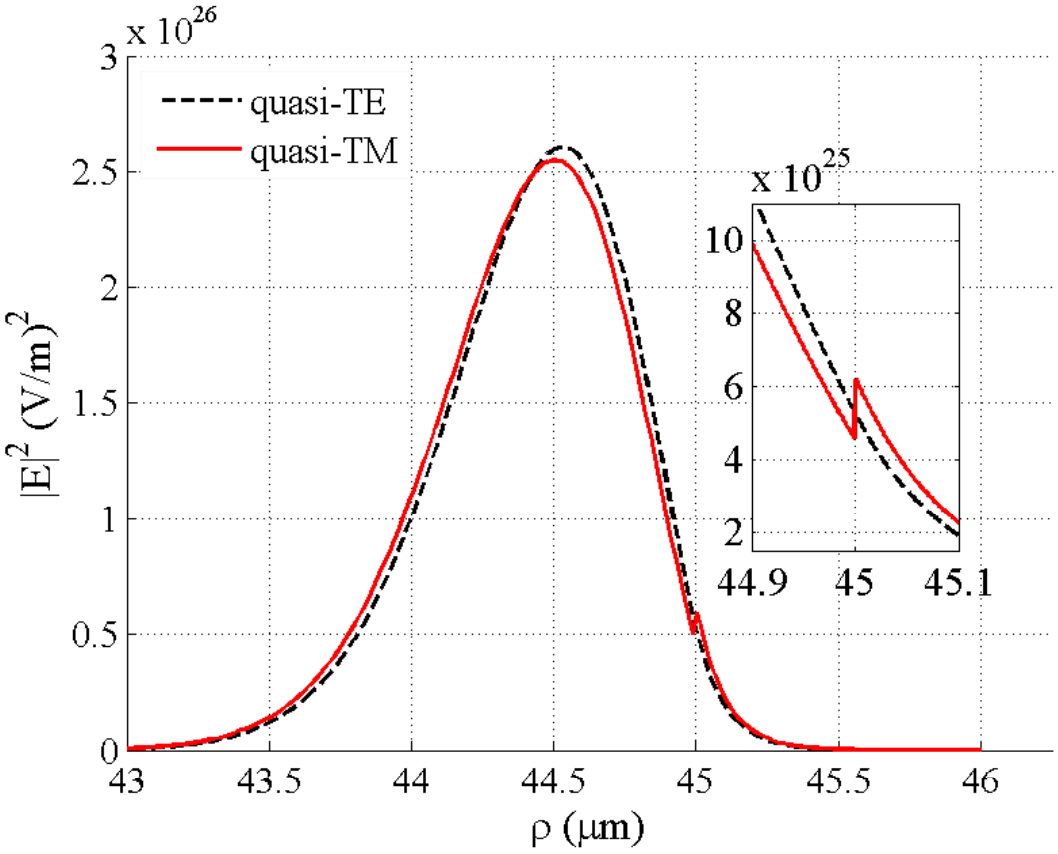

Figure 2.16: A 1D cross-sectional intensity plot of the fundamental modes along the ρ axis. While the toroid sits at the origin, the toroid surface ends at $\rho = 45$-μm. The insert provides a zoomed-in view of the intensity across the silica-water interface.

Fig. 2.16 provides a 1-D cross-sectional plot of $|\mathbf{E}|^2$ along the radial axis of the toroid. The toroid is placed at the origin and the silica-water interface locates at $\rho = 45$-μm. The field intensity experiences a peak value at about 0.5-μm away from the toroid surface. The insert gives a zoomed-in plot at the silica-water interface.

Since the quasi-TE mode is mainly polarized along the direction tangential to the interface, no significant discontinuity is observed. The quasi-TM mode, however, has an electric field oscillating along the direction normal to the interface and a discontinuity is observed.

For a microtoroid with a diameter of 90-μm, its Q-factor is mainly determined by the material loss. The Q-factor of the toroid is calculated using (2.24) from 230-nm to 1080-nm and is plotted on the left axis of Fig. 2.17. A Q-factor of 6.6×10^9 is calculated at a wavelength of 530-nm and drops to below 10^7 at 970-nm. On the right axis of Fig. 2.17, the spectrum attenuation coefficient of water is plotted. It is observed that the attenuation coefficient curve of water resembles the inverse of the Q-factor plot. The Q-factor of a microtoroid in an aqueous environment is largely affected by the water absorption.

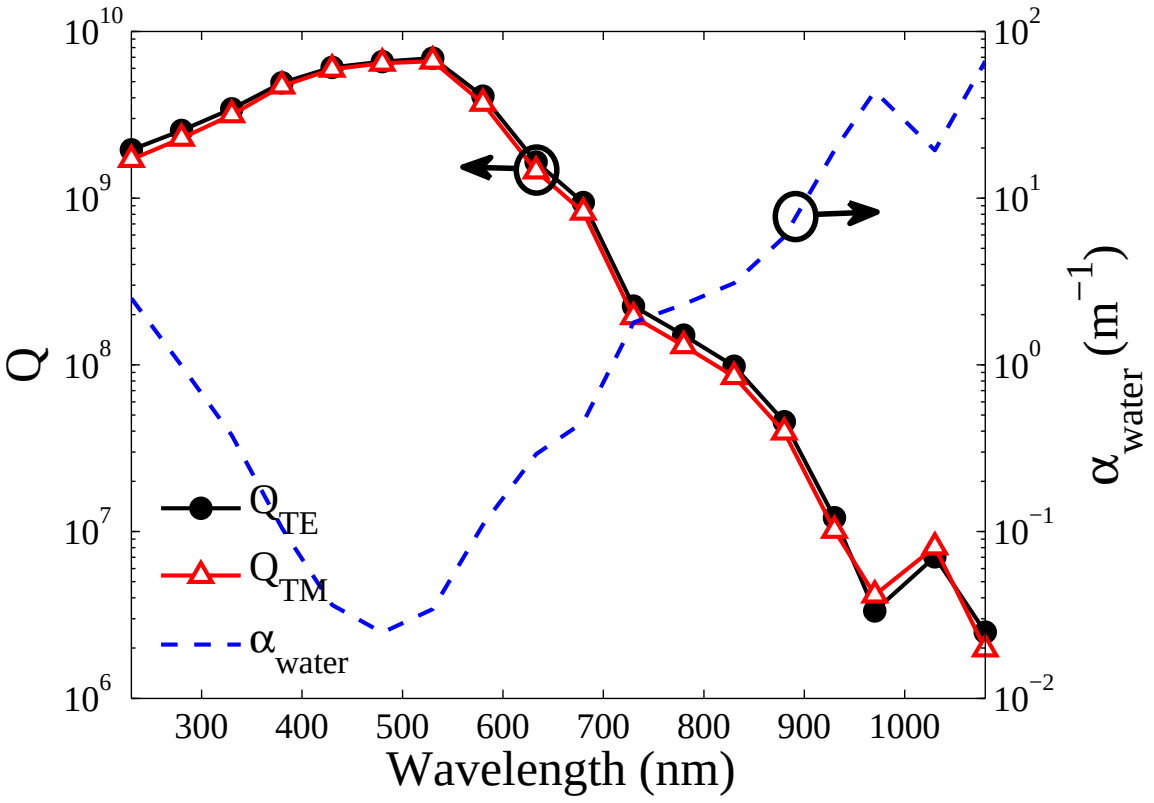

Figure 2.17: Q-factor of the fundamental quasi-TE and quasi-TM mode of a microtoroid at different wavelengths.

Fig. 2.18 displays the mode volumes calculated for the investigated toroid at different wavelengths. The fundamental modes of the toroid have mode volumes of a few hundred cubic micrometers. It is observed that the mode volume varies nearly linearly with wavelengths.

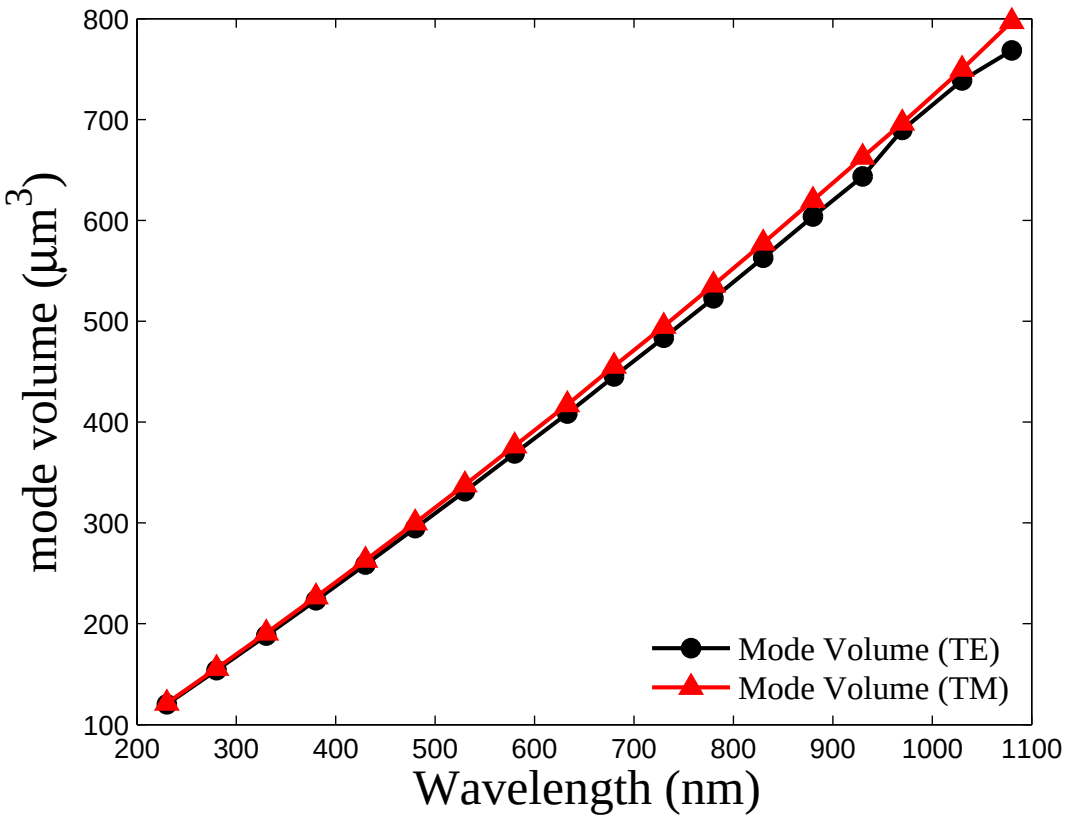

Figure 2.18: Mode volume of the fundamental quasi-TE and quasi-TM mode of a microtoroid at different wavelengths.

2.4.2 Wave Analysis Methods

While Oxborrow's weak form FEM modal simulates a perfectly axisymmetric WGM resonator with high accuracy and efficiency, numerical techniques are required for the analysis of the WGM resonators that do not possess axial-symmetries, such as WGM cavities bound with surface nanoparticles [70, 10], elliptical ring resonators [71], spiral cavities [25], and helical cavities [72]. In this section, several wave analysis methods attempting to solve these problems will be introduced.

First Order Perturbation Method

The first order perturbation method was developed to calculate the resonance shift of a WGM cavity upon surface bound nanoparticles [70, 17] with the assumption that the perturbation the surface inhomogeneity brings to the field is negligible. It is widely used for the ease of numerical application.

Starting from the Helmhöltz equation (2.7),

$$\nabla^2\mathbf{E} + \frac{\omega_0^2}{c^2} \cdot \epsilon_r\mathbf{E} = 0 \tag{2.36}$$

binding events are introduced as a perturbation to the field:

$$\nabla^2(\mathbf{E} + \delta\mathbf{E}) + \frac{(\omega_0 + \delta\omega)^2}{c^2}(\epsilon_r + \Delta\epsilon_r)(\mathbf{E} + \delta\mathbf{E}) = 0 \tag{2.37}$$

ω_0 is the unperturbed resonance angular frequency and $\delta\omega$ is the shift of angular frequency when perturbation occurs. The perturbation of the field is introduced by a surface inhomogeneity profile $\delta\epsilon$ which in this case is in a small volume.

Expand (2.37), introduce (2.36) and omit second order small terms. (2.37) becomes,

$$\nabla^2(\delta\mathbf{E}) + \frac{\omega^2}{c^2}\epsilon_r\Delta\mathbf{E} + \frac{\omega^2}{c^2}(\Delta\epsilon_r)\mathbf{E} + 2\frac{\omega\Delta\omega}{c^2}\epsilon_r\mathbf{E} = 0 \tag{2.38}$$

By subtracting $\mathbf{E}^*\cdot$(2.38) from $\delta\mathbf{E}\cdot$(2.36), and integrating over the entire space, we obtain:

$$\int_V \nabla(\delta\mathbf{E}\cdot\nabla\mathbf{E}^* - \mathbf{E}^*\nabla(\delta\mathbf{E}))\cdot dV - \frac{\omega^2}{c^2}\int_V \Delta\epsilon_r|\mathbf{E}|^2 dV - \frac{2\omega\Delta\omega}{c^2}\int_V \epsilon_r|\mathbf{E}|^2\cdot dV = 0 \tag{2.39}$$

The first term in (2.39) can be further written as,

$$\int_V \nabla(\delta\mathbf{E}\nabla\mathbf{E}^* - (\nabla\cdot\delta\mathbf{E})\mathbf{E}^*) = \int_S (\delta\mathbf{E}\cdot\nabla\mathbf{E}^* - \mathbf{E}^*\nabla(\delta\mathbf{E}))\cdot d\mathbf{S} \tag{2.40}$$

In (2.40) the first term $\delta\mathbf{E}\cdot\nabla\mathbf{E}^*$ contains the divergence of the mode, which is zero by definition. For the integration of the second term $\mathbf{E}^*\nabla(\delta\mathbf{E})$, we divide the boundary of the region S into two parts for generality: a perfect electric wall S' and a perfect magnetic wall S" (2.15).

Integral $\int_S(\nabla\delta\mathbf{E})\mathbf{E}^*\cdot d\mathbf{S}$ is zero on surface S", over which the electric field is tangential to the surface. Meanwhile, the contribution from the surface S' is propor-

tional to the net flux of the mode passing through the surface S'. As there is no net electron in the region and there is no flux escaping from S", this flux must be zero on S', resulting,

$$\int_S (\delta\mathbf{E} \cdot \nabla\mathbf{E}^* - \mathbf{E}^* \nabla(\delta\mathbf{E})) \cdot d\mathbf{S} = 0 \tag{2.41}$$

Finally, by substituting (2.40) to (2.39) we obtain

$$-\frac{\Delta\omega}{\omega} = \frac{\int_V \Delta\epsilon_r |\mathbf{E}|^2 dV}{2\int_V \epsilon |\mathbf{E}|^2 dV} \tag{2.42}$$

that describes the resonance shift of a single mode cavity upon small surface inhomogeneity. It is worth noting the numerator corresponds to the extra portion of energy it takes to polarize the binding particle. Thus, (2.42) can be interpreted as that the fractional resonance shift equals to the ratio of the energy it takes to polarize the surface inhomogeneity and the total energy stored in the cavity,

When the binding particle is small (under 100-nm, e.g.), the field over the binding particle can be further approximated as uniformly distributed. (2.42) can be further written as,

$$-\frac{\Delta\omega}{\omega} = \frac{\alpha}{2} \frac{|\mathbf{E}(\mathbf{r}_{NP})|^2}{\int_V \epsilon |\mathbf{E}|^2 dV} \tag{2.43}$$

where α is the excess polarizability of the binding particle and $\mathbf{E}(\mathbf{r}_{NP})$ is the electric field at the particle.

(2.42) and (2.43) are easy to implement with the FEM modal introduced in the previous session. Since (2.42) considers the field variance over the bead and consequently is more accurate than (2.43), an example of calculating the resonance shift due to polystyrene (PS) nano-beads of different radii using (2.42) will be given at an operational wavelength of 680-nm. To perform the volume integral, one first needs to recover the 2-D field solved by the mode solver back to 3-D by adding the azimuthal dependence $e^{jM\phi}$ back to the field. A 3-D geometry is built in COMSOL consisting a 3-D toroid and a sphere on its equator. Fig. 2.19 shows the 3-D work plane with an insert of a zoomed-in plot around the bead. The 2-D cross-sectional WGM is then projected to the 3-D structure using 'extrusion coupling variables' in COMSOL. Fig. 2.20 shows the projected field intensity on the midplane of the 25-nm radius bead. It is observed that there is about 30% variance of field intensity within the bead.

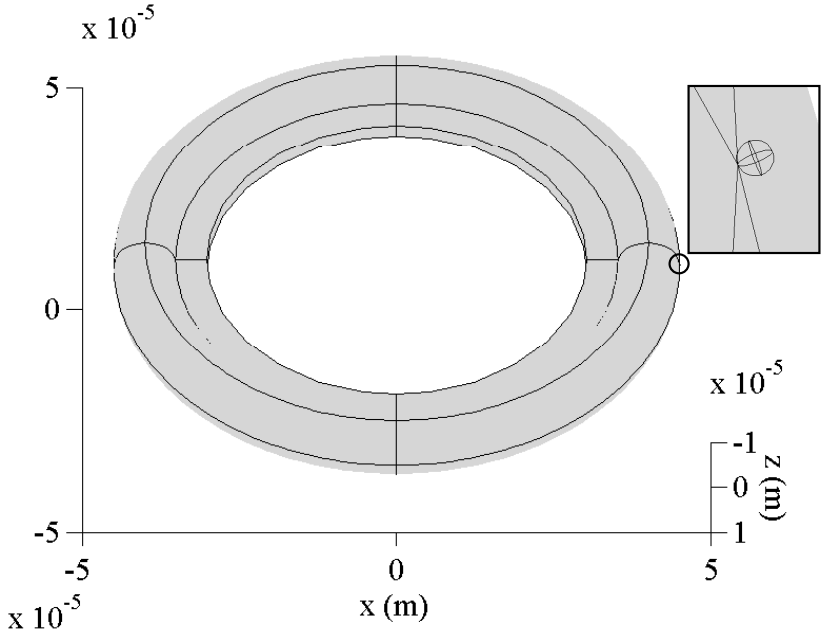

Figure 2.19: 3-D modeling of a microtoroid with a bound nanosphere on the equator in COMSOL. The insert provides a zoomed-in view of the sphere.

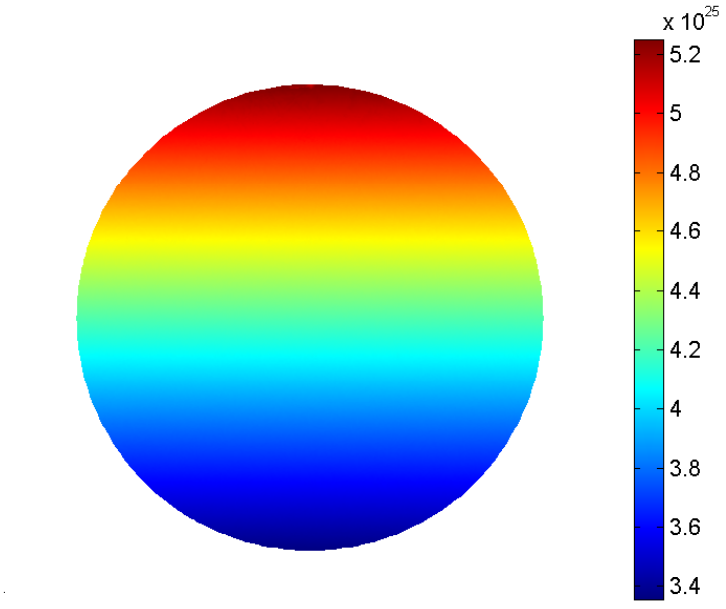

Figure 2.20: 2-D cross-sectional plot of the fundamental quasi-TE electric field intensity $|\mathbf{E}|^2$ projected to the bead sub-domain.

Fig. 2.21 shows the calculated resonance wavelength shift together with a comparison of the reported measurements in [9]. A wavelength shift of 19.42-fm is predicted by the perturbative method for a 50-nm radius PS bead and a shift as small as 0.42-fm is predicted for a 12.5-nm radius PS bead. The results given by the first order perturbation method is in close agreement with the reported measurements.

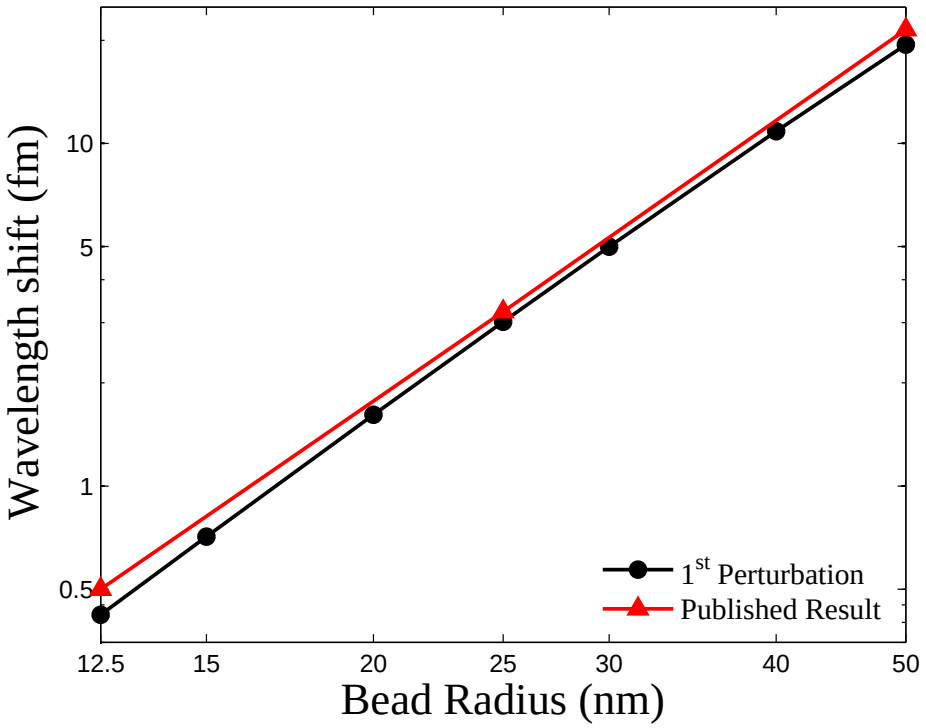

Figure 2.21: Binding shift due to a bound PS sphere for different radii at 680-nm. The black curve is calculated by the first order perturbation method and the red curve was reported in previous publication.

Other Methods

While the first order perturbation method yields highly accurate results for dielectric nanoparticles that do not trigger significant distortion to the cavity modal field. In the event that plasmonic nanoparticles land on the surface of a WGM cavity, the associated plasmonic effects focus the light around the bead, hence yielding larger inaccuracy. Such inaccuracy invalidates the perturbation approach in the case of large metallic beads or at a wavelength close to the plasmon resonance [18].

To circumvent this problem, a refinement scheme for the first order perturbation

approach was proposed [10, 73] to model the WGM cavities with bound plasmonic particles. By approximating the WGM using a polarized plane wave, such a scheme employs an additional optical scattering solver to refine the field surrounding the bound particles. While such a refinement scheme provides an effective solution to nanoscale plasmonic and non-plasmonic binding problems, the plane wave approximation approaches its limit for larger particles when the field across the particle is no longer uniform. Further, perturbative approaches cannot simulate the resonance wavelength and the quality factor of a WGM cavity that does not exhibit axisymmetry under the current formalism [74, 75].

Alternatively, one may choose first-principle techniques that directly solve Maxwell's equations, Helmhöltz equations or Green functions with numerical techniques such as Finite-Difference, Finite-Element or Boundary-Element [76, 77, 54, 55, 56, 57, 58] methods to perform a full wave analysis over the three-dimensional WGM microcavities. Unfortunately, such techniques require the discretization of the WGM along all three spatial dimensions. This necessitates extensive computational resources compared to 2-D mode solver based techniques due to orders of magnitude increase in grid points. To accommodate such difficulties, first principle techniques are commonly used in conjunction with the effective index technique to approximate the three-dimensional WGM as a two-dimensional one. In [77], a new approach is proposed to simulate a WGM with a localized perturbation by treating the perturbed section of the WGM as a three-dimensional closed cavity, where artificial boundary conditions such as a perfect electrical wall are imposed at the input and output ends of the section. A three-dimensional mode of this perturbed section is then computed with the finite element method to approximate the distorted WGM field and other corresponding parameters. Such a method can yield better accuracy compared to a perturbation approach by applying a correction to the WGM field distorted by the bead. In this case, the number of grid points per computation step that are involved is larger than the perturbation approach yet fewer than first principle techniques. On the other hand, the boundary condition imposed in[77], as pointed out by the authors of that article, is based on the assumption that the light scattered by the adsorbed bead will quickly "heal" within the perturbed section and that the model "represents a resonator with many particles [located periodically] along the circumference." Such an assumption no longer holds for the binding of larger beads or for beads that are located at random positions, thereupon introducing a significant phase shift and amplitude distortion of the otherwise unperturbed WGM field. The field obtained from

this method is a standing wave pattern of the cavity, which departs from the realistic situation where a travelling wave is involved. Furthermore, the multi-scale nature of a WGM-nanoparticle system introduces additional challenges with these methods. For a large size perturbation such as a fiber taper placed close to the cavity, a large section is needed for the model. This causes the resulting mesh to become too large for a conventional computer to handle.

Chapter 3

Single-Mode Mode-Matching Analysis for Whispering Gallery Microcavities

To circumvent the problems encountered in the last section of the previous chapter, in this chapter the mode-matching formulas will be presented in the cylindrical coordinates for whispering gallery mode cavities. This formulation is fully vectorial, highly accurate, computationally efficient and able to deal with a general form of axial asymmetry.[1]

3.1 Mode-Matching Method

Mode-Matching Method is a computational electromagnetics modeling technique with high accuracy [79, 80]. MMM has been used in modeling waveguide discontinuities[81, 19, 79, 82], filters[20], fiber optics and optical devices[83].

MMM simulates the propagation of the electromagnetics (EM) field by expanding it onto a set of local eigenmodes at the cross section of the structure. For efficiency, only a subset of eigenmodes are usually used in MMM analysis. On the other hand, MMM can be fully vectorial for higher accurate.

Scattering matrix (S-matrix) technique can be further implemented to join the different parts of the waveguide. The scattering matrix of the two sides of a discontinuity can be calculated by examining the continuity relation of the electric field (E

[1]The work presented in this chapter was published in [78]

field) and the magnetic field (H field). For a continuously varying structure along the propagating direction like a tapered fiber, the device needs to be dicretized into different sections.

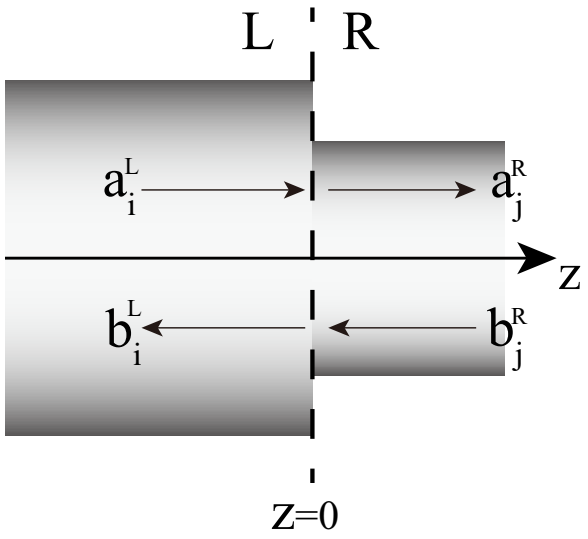

Figure 3.1: A 3-D waveguide structure with a discontinuity at z=0. EM wave propagates bidirectionally inside the waveguide.

Fig. 3.1 shows a 3-D waveguide discontinuity at z=0. The left-hand section of the discontinuity is named L and the right-hand section is named R. $\hat{\mathbf{e}}_i^L$ and $\hat{\mathbf{h}}_i^L$ ($\hat{\mathbf{e}}_j^R$ and $\hat{\mathbf{h}}_j^R$) form the orthonormal eigenmode set of L (R). Here i and j are the mode indices. The orthonormality of the waveguide modes can be expressed as [79],

$$\frac{1}{2}\int(\hat{\mathbf{e}}_i \times \hat{\mathbf{h}}_j)\cdot\hat{\mathbf{z}}\cdot dS = \delta_{ij} \tag{3.1}$$

In Fig. 3.1, a_i denotes the complex amplitude of the forward propagating mode and b_i indicates that of the backward propagating mode. The EM field on the left hand side can be decomposed into the basis set of eigenmodes ($\hat{\mathbf{e}}_i^L$,$\hat{\mathbf{h}}_i^L$) in the cross section of L while on the right hand side the field can be decomposed into the eigenmodes ($\hat{\mathbf{e}}_j^R$,$\hat{\mathbf{h}}_j^R$) in the cross section of R.

for z<0

$$\begin{cases} \mathbf{E}^L = \sum_{i=1}^{N} (a_i^L e^{-j\beta_i^L z} + b_i^L e^{j\beta_i^L z}) \hat{\mathbf{e}}_i^L & (3.2a) \\ \mathbf{H}^L = \sum_{i=1}^{N} (a_i^L e^{-j\beta_i^L z} - b_i^L e^{j\beta_i^L z}) \hat{\mathbf{h}}_i^L & (3.2b) \end{cases}$$

for z>0

$$\begin{cases} \mathbf{E}^R = \sum_{j=1}^{N} (a_j^R e^{-j\beta_j^R z} + b_j^R e^{j\beta_j^R z}) \hat{\mathbf{e}}_j^R & (3.3a) \\ \mathbf{H}^R = \sum_{j=1}^{N} (a_j^R e^{-j\beta_j^R z} - b_j^R e^{j\beta_j^R z}) \hat{\mathbf{h}}_j^R & (3.3b) \end{cases}$$

at z=0, the continuity of the tangential E field and H field requires that $\mathbf{E}_t^L = \mathbf{E}_t^R$ and $\mathbf{H}_t^L = \mathbf{H}_t^R$.

$$\begin{cases} \sum_{i=1}^{N} (a_i^L + b_i^L) \hat{\mathbf{e}}_{it}^L = \sum_{j=1}^{N} (a_j^R + b_j^R) \hat{\mathbf{e}}_{jt}^R & (3.4a) \\ \sum_{i=1}^{N} (a_i^L - b_i^L) \hat{\mathbf{h}}_{it}^L = \sum_{j=1}^{N} (a_j^R - b_j^R) \hat{\mathbf{h}}_{jt}^R & (3.4b) \end{cases}$$

Here t denotes the transverse components of the field. By taking the cross product of (3.4a) with $\hat{\mathbf{h}}_{it}^L$ and (3.4b) with $\hat{\mathbf{e}}_{it}^L$, performing a surface integral at the cross section z=0, and utilizing the orthonormality condition (3.1) we obtain,

$$\begin{cases} a_i^L = \sum_{j=1}^{N} a_j^R \left(\frac{\langle \hat{\mathbf{e}}_j^R, \hat{\mathbf{h}}_i^L \rangle + \langle \hat{\mathbf{e}}_i^L, \hat{\mathbf{h}}_j^R \rangle}{2} \right) + \sum_{j=1}^{N} b_j^R \left(\frac{\langle \hat{\mathbf{e}}_j^R, \hat{\mathbf{h}}_i^L \rangle - \langle \hat{\mathbf{e}}_i^L, \hat{\mathbf{h}}_j^R \rangle}{2} \right) & (3.5a) \\ b_i^L = \sum_{j=1}^{N} a_j^R \left(\frac{\langle \hat{\mathbf{e}}_j^R, \hat{\mathbf{h}}_i^L \rangle - \langle \hat{\mathbf{e}}_i^L, \hat{\mathbf{h}}_j^R \rangle}{2} \right) + \sum_{j=1}^{N} b_j^R \left(\frac{\langle \hat{\mathbf{e}}_j^R, \hat{\mathbf{h}}_i^L \rangle + \langle \hat{\mathbf{e}}_i^L, \hat{\mathbf{h}}_j^R \rangle}{2} \right) & (3.5b) \end{cases}$$

Here we define the inner product as,

$$\langle \hat{\mathbf{e}}, \hat{\mathbf{h}} \rangle = \frac{1}{2} \int \hat{\mathbf{e}} \times \hat{\mathbf{h}} \cdot \hat{\mathbf{z}} dS \tag{3.6}$$

We can write the transmitting equations (3.5) in the matrix form as,

$$\begin{pmatrix} A^L \\ B^L \end{pmatrix} = \begin{pmatrix} T_{11RL} & T_{12RL} \\ T_{21RL} & T_{22RL} \end{pmatrix} \begin{pmatrix} A^R \\ B^R \end{pmatrix} = T_{RL} \begin{pmatrix} A^R \\ B^R \end{pmatrix} \tag{3.7}$$

where A^R,B^R,A^L and B^L are the mode amplitude vectors $(a_1^R, a_2^R, ...a_N^R)$, $(b_1^R, b_2^R, ...b_N^R)$, $(a_1^L, a_2^L, ...a_N^L)$, and $(b_1^L, b_2^L, ...b_N^L)$, respectively. T_{RL} is the transfer matrix across the discontinuity z=0. The scattering matrix technique can further be applied by rewriting (3.7) as,

$$\begin{pmatrix} A^R \\ B^L \end{pmatrix} = \begin{pmatrix} T_{LR} & R_{RL} \\ R_{LR} & T_{RL} \end{pmatrix} \begin{pmatrix} A^L \\ B^R \end{pmatrix} = S_{LR} \begin{pmatrix} A^L \\ B^R \end{pmatrix} \tag{3.8}$$

This way the scattering matrix across the discontinuous interface is constructed. The complete scattering matrix of the whole device, which may contain multiple discontinuities or periodic structure, can be acquired by cascading the scattering matrices across the junctions and the propagation matrices[84, 85].

3.2 MMM analysis of WGM Cavities

3.2.1 Ideal Whispering-Gallery-Mode Microcavities

An ideal or axisymmetric whispering-gallery-mode microcavity has a complex refractive profile $\tilde{n}(\rho, z, \phi)$ independent of the azimuthal angle ϕ (ie. $\tilde{n}(\rho, z, \phi) = \tilde{n}(\rho, z)$) in a concentric cylindrical coordinate system, as shown in Fig. 2.3. The electric field $\tilde{\mathbf{E}}(\rho, z, \phi)$ of light at wavelength λ_0 that propagates inside the cavity has the form

$$\tilde{\mathbf{E}}(\rho, z, \phi) = \tilde{A}(\phi) \cdot \hat{\tilde{\mathbf{e}}}(\rho, z) \tag{3.9}$$

where $\hat{\tilde{\mathbf{e}}}(\rho, z)$ is the whispering-gallery-mode profile obtainable from the corresponding mode equations

$$\left[\frac{\partial^2}{\partial \rho^2} + \frac{1}{\rho} \frac{\partial}{\partial \rho} + \frac{\partial^2}{\partial z^2} + \left(k_0^2 \tilde{n}^2(\rho, z) - \frac{\tilde{m}^2}{\rho^2} \right) \right] \hat{\tilde{\mathbf{e}}}(\rho, z) = \mathbf{0} \tag{3.10}$$

The mode profile is normalized according to the area integral at the cavity cross section normal to the $\hat{\phi}$ direction. That is, $\frac{1}{2\eta_0}\int \tilde{n}_r(\rho,z)\hat{\tilde{e}}^*(\rho,z)\hat{\tilde{e}}(\rho,z)d\sigma = 1$[2] such that the field amplitude square $\tilde{A}(\phi)^* \cdot \tilde{A}(\phi)$ represents the power at ϕ in units of Watts. Here $\eta_0 = 377$ Ohms is the free space impedance and $\tilde{n}_r(\rho,z)$ is the real part of the refractive index at ϕ. $\tilde{m} = \tilde{m}_r + j\tilde{m}_i$ is a constant complex number whose real part $\tilde{m}_r$ encompasses the phase change of the wavefront and the imaginary part $\tilde{m}_i$ characterizes the loss of the wave along the propagation direction. In the case of an ideal WGM cavity, $\tilde{A}(\phi) = \tilde{A}(\phi = 0)e^{j\tilde{m}\phi}$. When λ_0 coincides with the cavity resonance wavelength $\tilde{\lambda}_{res}$, $\tilde{m}_r$ becomes an integer M whose value determines the azimuthal order of the mode. The loss of the cavity can be estimated by the quality factor $Q_{tot} = M/2\tilde{m}_i$ with the value contributed by cavity material absorption ($\tilde{Q}_{abs} = M/2\tilde{m}_{abs}$), radiation loss ($\tilde{Q}_{rad} = M/2\tilde{m}_{rad}$), surface roughness ($\tilde{Q}_{surf} = M/2\tilde{m}_{surf}$), and cavity to tapered waveguide coupling ($\tilde{Q}_{couple} = M/2\tilde{m}_{couple}$). In summary,

$$\begin{aligned} \frac{1}{\tilde{Q}_{tot}} &= \frac{2\tilde{m}_i}{M} = \frac{1}{\tilde{Q}_{abs}} + \frac{1}{\tilde{Q}_{rad}} + \frac{1}{\tilde{Q}_{surf}} + \frac{1}{\tilde{Q}_{couple}} \\ \tilde{m}_i &= \tilde{m}_{abs} + \tilde{m}_{rad} + \tilde{m}_{surf} + \tilde{m}_{couple} \end{aligned} \tag{3.11}$$

3.2.2 Non-ideal Whispering-Gallery-Mode Microcavities

In general, a whispering-gallery-mode microcavity may have a ϕ-dependent refractive index profile $n(\rho,z,\phi)$ if particle binding occurs, surface imperfections exist, a waveguide taper is placed close to the cavity, or other geometrical disturbances are introduced. For simplicity, we drop ˜ symbols for all the physical quantities to distinguish them from those defined in an ideal WGM.

[2] In this work presented in [78] a plane wave approximation is applied. Latter it is discovered that the normalization condition 2.20 for cavity modes gives more rigorous results as will be presented in chapter 4.

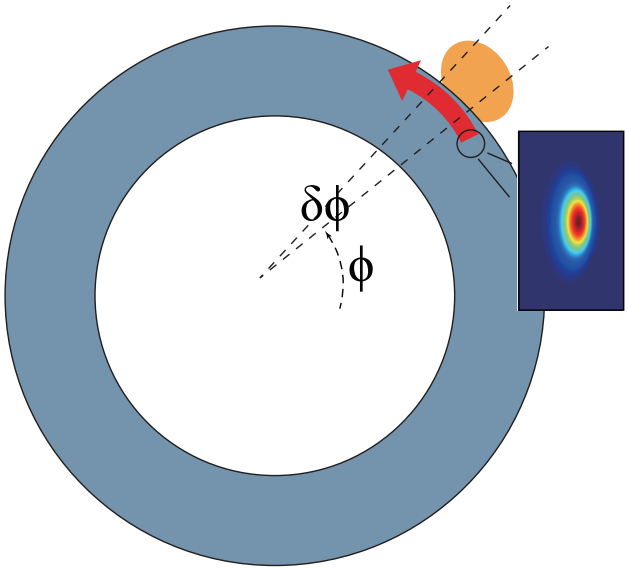

Figure 3.2: Light propagating from ϕ to $\phi + \delta\phi$ as it passes by a bound particle.

At an azimuthal angle ϕ_0, the electrical field distribution at the cross section $\mathbf{E}(\rho, z, \phi_0)$ can be expanded onto the normalized WGM mode $\hat{\mathbf{e}}(\rho, z, \phi_0)$ at ϕ_0 according to

$$\mathbf{E}(\rho, z, \phi_0) = A(\phi_0) \cdot \hat{\mathbf{e}}(\rho, z, \phi_0) \tag{3.12}$$

Note that by analogy to the MMM in Cartesian coordinates, we may obtain a complete set of orthogonal modes at the azimuthal angle ϕ_0 that satisfies the mode equation of a perfect WGM cavity

$$\left[\frac{\partial^2}{\partial\rho^2} + \frac{1}{\rho}\frac{\partial}{\partial\rho} + \frac{\partial^2}{\partial z^2} + \left(k_0^2 n^2(\rho, z, \phi_0) - \frac{m(\phi_0)^2}{\rho^2}\right)\right] \hat{\mathbf{e}}(\rho, z, \phi_0) = \mathbf{0} \tag{3.13}$$

where both the mode profile and m have become ϕ-dependent. Additionally, given that (3.13) is identical to (3.10) for any fixed angle ϕ_0, one may find the M^{th} order resonant wavelength $\lambda_r(\phi)$ at ϕ_0 by replacing k_0 with $2\pi/\lambda_r$, m with M, and solving the mode equation above using a two-dimensional mode solver for ideal WGM's (such as that in[14]). Note $\lambda_r(\phi)$ is also a ϕ-dependent quantity. After propagating an infinitesimal azimuthal angle $\delta\phi$ (Fig. 3.2), we obtain the electrical field at $\phi_0 + \delta\phi$

$$\mathbf{E}(\rho, z, \phi_0 + \delta\phi) = A(\phi_0) \cdot \hat{\mathbf{e}}(\rho, z, \phi_0) e^{jm(\phi_0)\delta\phi} \tag{3.14}$$

Under the approximation that, on average, photons in the mode travel the same optical path length and experience the same loss as those at the resonance wavelength $\lambda_r(\phi_0)$, we can obtain the real m_r and imaginary m_i part of $m(\phi_0)$ after infinitesimal rotation $\delta\phi$ via

$$\begin{aligned} m_r(\phi_0) &= M \tfrac{\lambda_r(\phi_0)}{\lambda_0} \\ m_i(\phi_0) &= m_{abs}(\phi_0) + m_{rad}(\phi_0) \end{aligned} \tag{3.15}$$

Here, we ignore m_{couple} and m_{surf} for a purpose explained in a later section. On the other hand, $\mathbf{E}(\phi_0 + \delta\phi)$ can be expanded onto the normalized eigen mode $\hat{\mathbf{e}}(\rho, z, \phi_0 + \delta\phi)$, defined at $\phi_0 + \delta\phi$,

$$\mathbf{E}(\rho, z, \phi_0 + \delta\phi) = A(\phi_0 + \delta\phi) \cdot \hat{\mathbf{e}}(\rho, z, \phi_0 + \delta\phi) \tag{3.16}$$

By equating the right hand sides of (3.14) and (3.16), multiplying both sides by $\frac{1}{2\eta_0} n_r(\rho, z, \phi_0 + \delta\phi)\hat{\mathbf{e}}(\rho, z, \phi_0 + \delta\phi)$, and integrating over the cross section at $\phi_0 + \delta\phi$, we obtain the evolution of $A(\phi_0 + \delta\phi)$ according to

$$A(\phi_0 + \delta\phi) = A(\phi_0) \cdot e^{j[M + \delta m(\phi)]\delta\phi} \tag{3.17}$$

We may then obtain an additional loss term $m_m(\phi_0)$ characterized by

$$m_m(\phi_0) = -\lim_{\delta\phi \to 0} \frac{1}{\delta\phi} \ln \left[\int \frac{n_r(\rho, z, \phi_0 + \delta\phi)}{2\eta_0} \hat{e}^*(\rho, z, \phi_0 + \delta\phi)\hat{e}(\rho, z, \phi) d\sigma \right] \tag{3.18}$$

arising from the mode mismatch between $\hat{e}(\phi_0 + \delta\phi)$ and $\hat{e}(\phi_0)$ in addition to the absorption and radiation loss derived from m_i. For simplicity, we redefine $m_i(\phi_0) = m_m(\phi_0) + m_{abs}(\phi_0) + m_{rad}(\phi_0)$ and define a mode order detuning term $\delta m(\phi) = [m_r(\phi) - M] + jm_i(\phi)$. Consequently, the field $\mathbf{E}(\rho, z, 0) = A(0)\hat{\mathbf{e}}(\rho, z, 0)$ propagating from $\phi = 0$ to an azimuthal angle ϕ_0 can be expressed as

$$\mathbf{E}(\rho, z, \phi_0) = A(0) e^{j[M\phi_0 + \int_{\phi=0}^{\phi_0} \delta m(\phi) d\phi]} \hat{\mathbf{e}}(\rho, z, \phi_0) \tag{3.19}$$

To satisfy the resonance condition, the overall phase change of the field after propagating through a 2π azimuthal angle should be $2M\pi$:

$$\int_{\phi=0}^{2\pi} m_r(\phi)d\phi = 2M\pi \tag{3.20}$$

Together with (3.15) we obtain the resonance wavelength of the whispering-gallery-mode microcavity λ_{res} by simply taking the arithmetic mean of the resonance wavelengths $\lambda_r(\phi)$ at each cross section of the cavity, where $\lambda_r(\phi_0)$ at each ϕ_0 can be obtained from the WGM mode solver for the case of an ideal WGM whose cross-sectional refractive index profile is identical to that at ϕ_0.

$$\lambda_{res} = \frac{\int_0^{2\pi} \lambda_r(\phi)d\phi}{2\pi} \tag{3.21}$$

It is worth emphasizing that the simple expression in (3.21) is valid for all whispering-gallery-mode microcavities, including those with or without axisymmetric properties, those that are subject to dielectric or metallic particle binding, or those in the presence of a tapered fiber or any other structures. The equation above can be further simplified if the perturbation or non-axisymmetric parts of the microcavity are localized to a small region, as is demonstrated in the application section below. Similarly, one may derive the overall quality factor of an asymmetric or perturbed WGM cavity from the algebraic average of the imaginary part of δm as

$$\begin{aligned} \frac{1}{Q_{tot}} &= \frac{2\int_0^{2\pi}[m_m(\phi)+m_{abs}(\phi)+m_{rad}(\phi)]d\phi}{2\pi M} \\ &= \frac{1}{Q_m} + \frac{1}{Q_{abs}} + \frac{1}{Q_{rad}} \end{aligned} \tag{3.22}$$

As can be seen, in the absence of the axisymmetry, an additional loss term from the mode mismatch between neighbouring cross sections occurs. This yields the decrease of overall Q_{tot} factor from the inclusion of the mode mismatch Q_m.

3.3 Simulation Procedure

In this test case we examine the resonant wavelength shift and decrease of Q-factor when N nanoparticles land on the surface of a WGM cavity. Here we assume each nanoparticle i occupies a space lying between ϕ_i and $\phi_i + \Delta\phi_i$. From (3.21) and (3.22) we derive that the particle induced resonance wavelength shift $\Delta\lambda$ and quality factor

Q change follows the expression

$$\Delta\lambda = \frac{\sum_{i=1}^{N} \int_{\phi_i}^{\phi_i+\Delta\phi_i} [\lambda_r(\phi) - \tilde{\lambda}_{res}] d\phi}{2\pi} \tag{3.23}$$

$$\frac{1}{Q_{tot}} - \frac{1}{\tilde{Q}_{tot}} = \frac{2\sum_{i=1}^{N} \int_{\phi_i}^{\phi_i+\Delta\phi_i} [m_m(\phi) + m_{abs}(\phi) + m_{rad}(\phi) - \tilde{m}_i] d\phi}{2\pi M} \tag{3.24}$$

Equations (3.23) and (3.24) are numerically verified at an operational wavelength around 633-nm on a silica microtoroid platform [86]. The silica microtoroid under investigation has a major radius of 40-μm and a minor radius of 5-μm. The surrounding environment is filled with water. Polystyrene (PS) beads and gold (Au) beads are individually placed on the toroid equator and the refractive indices of silica ($1.457+(6.95 \times 10^{-11})j$), water ($1.33168+(1.47\times10^{-8})j$), PS ($1.583+(5.29\times10^{-4})j$), and Au ($0.1834+3.433j$) are taken from literature [69, 37, 87, 34]. We employed a full vector finite element whispering-gallery-mode solver according to [14] to obtain the mode at each cross section. The computation domain was meshed adaptively in order to improve the accuracy of the calculated eigen value. The trapezoidal rule is implemented to perform the integral (3.23) and (3.24) numerically to get the total resonant wavelength shift and Q factor degradation of the hybrid cavity mode. Note that for the same mesh density,[77] requires approximately 90 times more grid points than MMM in each computation step assuming a minimum-size slice of a half-wavelength in length along the cavity edge was adopted in [77]. It is demonstrated that one typical MMM simulation of a hybrid WGM-nano particle system for a 20-nm radius gold bead takes 33 seconds for a relative error of the calculated resonance shift around 0.3 when only two slices along the azimuthal angle are involved. Higher accuracy can be achieved with more densely packed slices along the azimuthal direction and a more accurate mode solver.

3.4 Simulation Results

Figure 3.4 shows the intensity of the normalized toroid-bead hybrid modes at the azimuthal cross section, where the center of the beads is located. As shown in Fig. 3.3, where a polystyrene bead was adsorbed at the equator of the toroid, the intensity

around the bead (c.f. Fig. 3.3 insets) displays little distortion from the unperturbed toroid mode. In this case, the resulting resonance shift of the cavity can be extracted with sufficient accuracy using first order perturbation theory [17]. Fig. 3.4 shows the WGM-SP hybrid mode excited at the gold-dielectric interface. As shown in Fig. 3.4's insets, there is strong field intensity stored in the surface plasmon resulting in two hot spots aligned along the same direction as that of the electric field (along the $\hat{z}$ direction for the TE mode and $\hat{\rho}$ direction along the TM mode). Such significant distortion to the WGM precludes the treatment of such problems with first order perturbation theory. On the other hand, MMM intrinsically incorporates the change in mode field distribution and yields accurate evaluations of the perturbed system.

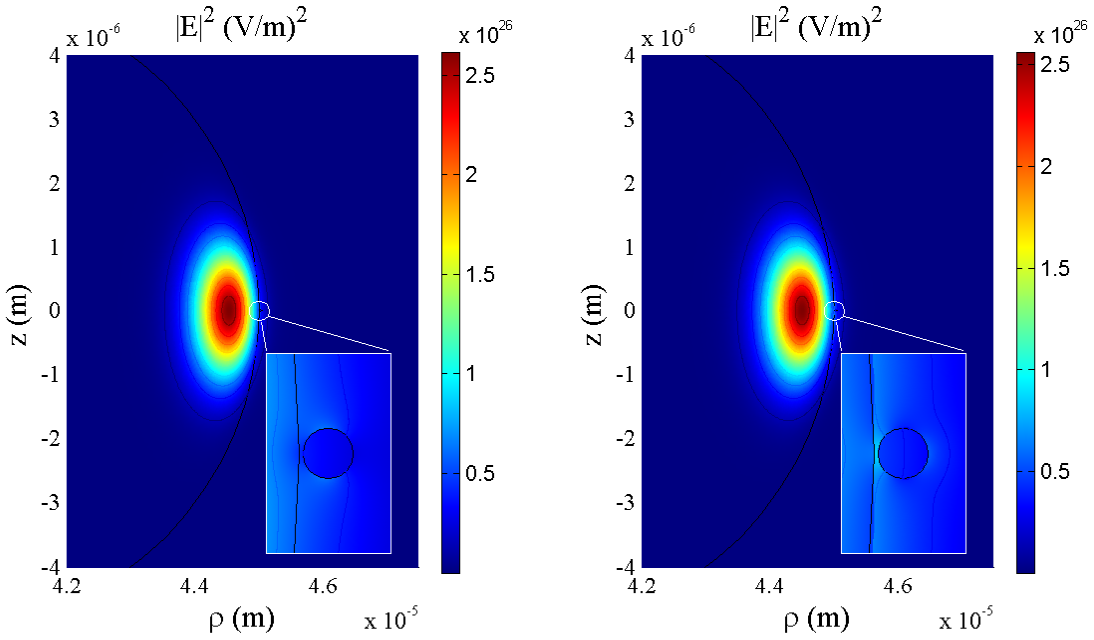

Figure 3.3: The fundamental (a)quasi-TE and (b) quasi-TM mode intensity distribution of a silica microtoroid with a polystyrene bead bound to the equator at a 633-nm wavelength. The modes are plotted at the azimuthal cross section where the center of the bead is located. The insets provide a zoomed-in view of the intensity distribution around the beads.

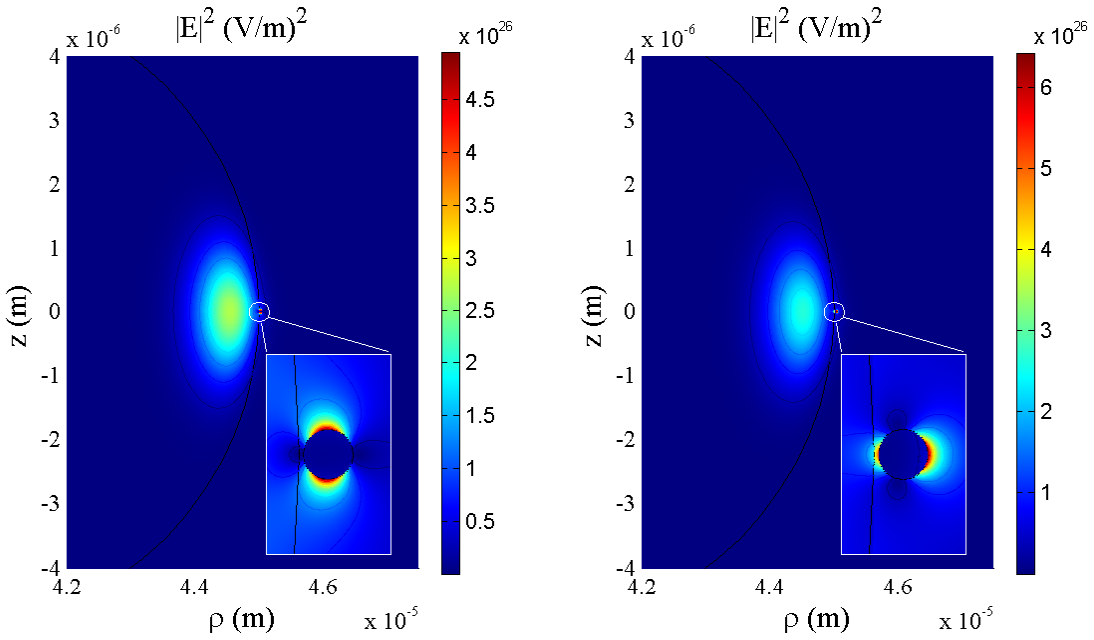

Figure 3.4: The fundamental (a) quasi-TE and (b) quasi-TM mode intensity distribution of a silica microtoroid with a gold bead bound to the equator at a 633-nm wavelength. The modes are plotted at the azimuthal cross section where the center of the bead is located. The insets provide a zoomed-in view of the intensity distribution around the bead.

Fig. 3.5 shows the one-dimensional (1-D) intensity plots along the -axis of the fundamental mode for gold and PS binding particles. It is observed that, due to the coupling of the WGM and surface plasmon, the field intensity outside the cavity is stronger than the field intensity inside the cavity.

Fig. 3.6 and 3.7 illustrate the calculated terms m_r, m_m, and m_{abs} arising from the PS (Fig. 3.6) and gold (Fig. 3.7) nanoparticles. It is observed that the mode mismatch loss dominates the degradation of the Q factor over material absorption in both cases.

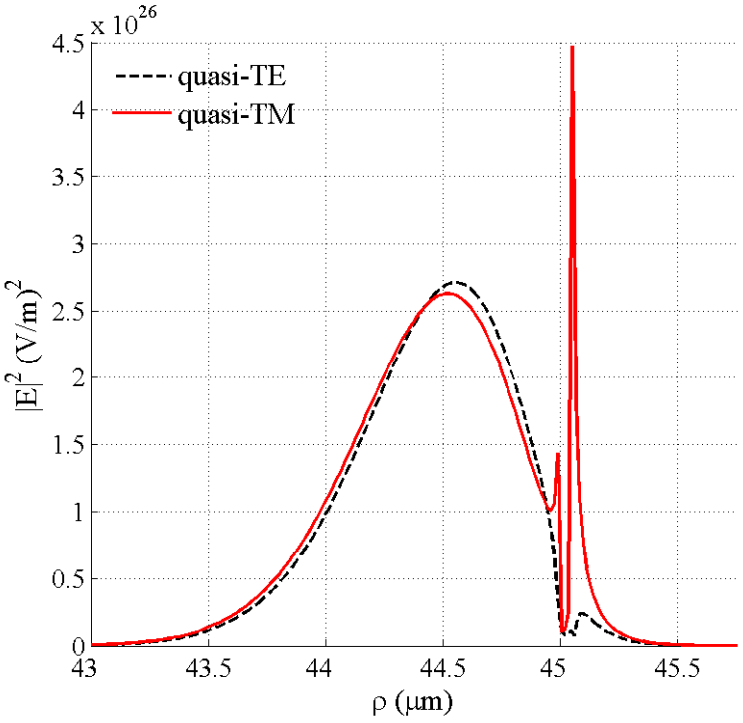

(a)

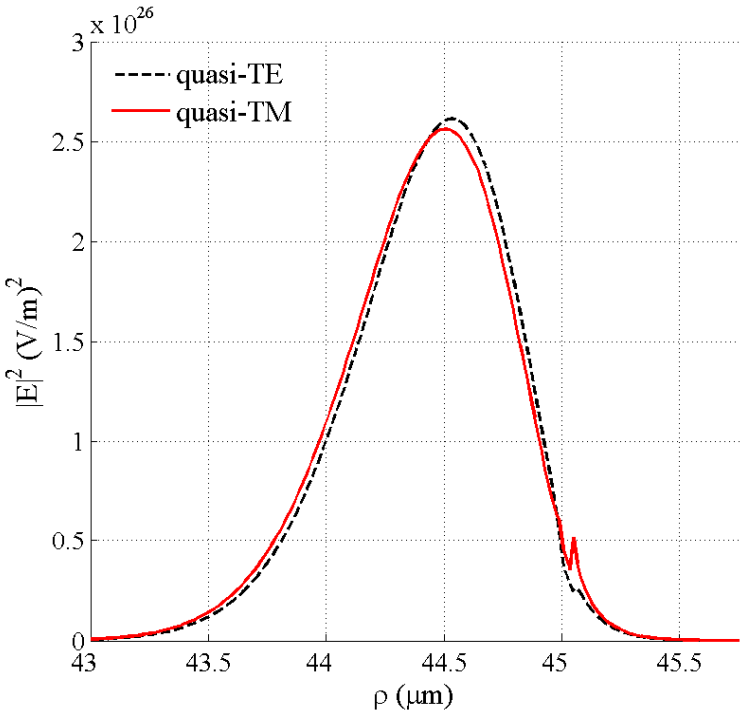

(b)

Figure 3.5: 1-D cross sectional intensity plot: (a) intensity profile of the fundamental quasi-TE and quasi-TM modes for a 25-nm radius gold nanoparticle at $\lambda = 633$-nm. The toroid surface ends at 45-μm.(b) the same as (a) for a 25-nm radius polystyrene nanoparticle.

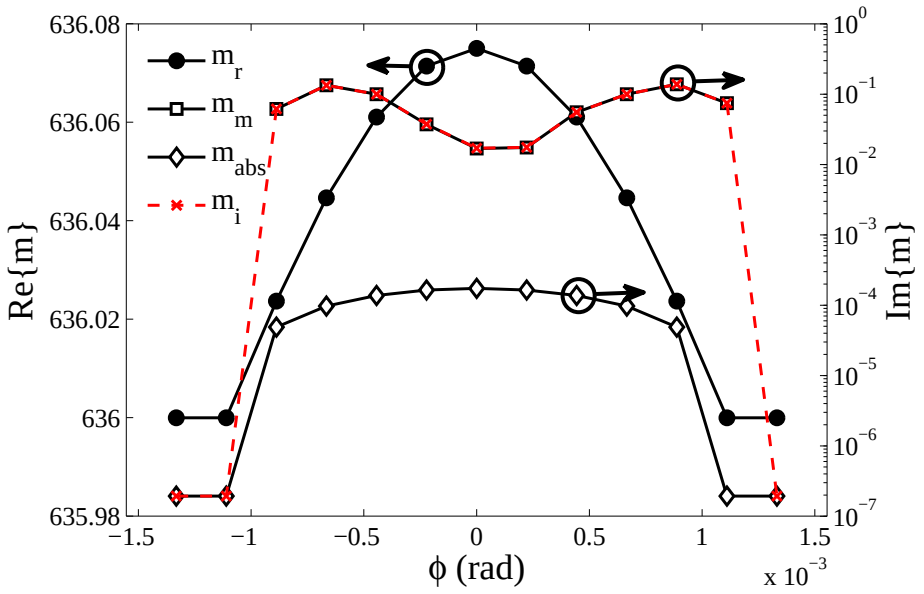

Figure 3.6: The real and imaginary part of the mode order m along the propagation direction when a 50-nm radius PS bead is placed at $\phi = 0$.

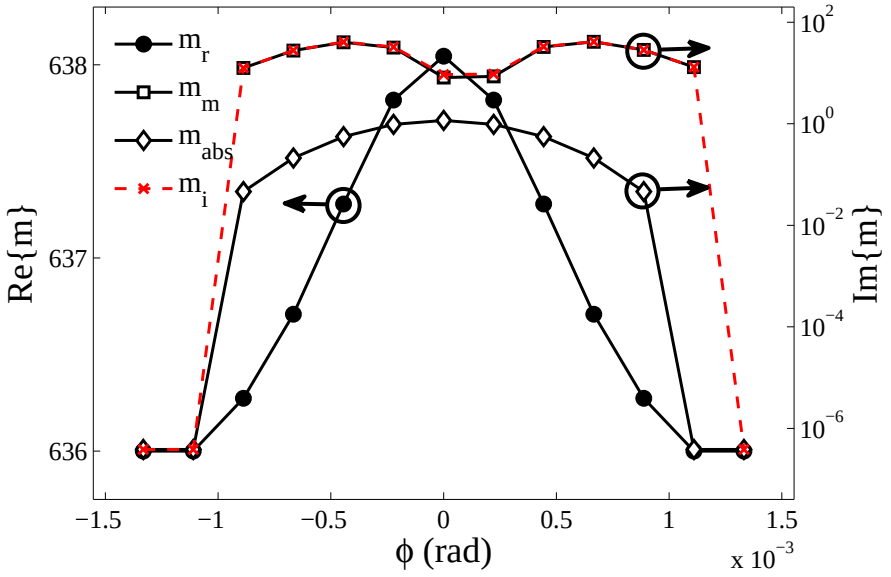

Figure 3.7: The real and imaginary part of the mode order m along the propagation direction when a 50-nm radius Au bead is placed at $\phi = 0$.

3.5 Numerical Error

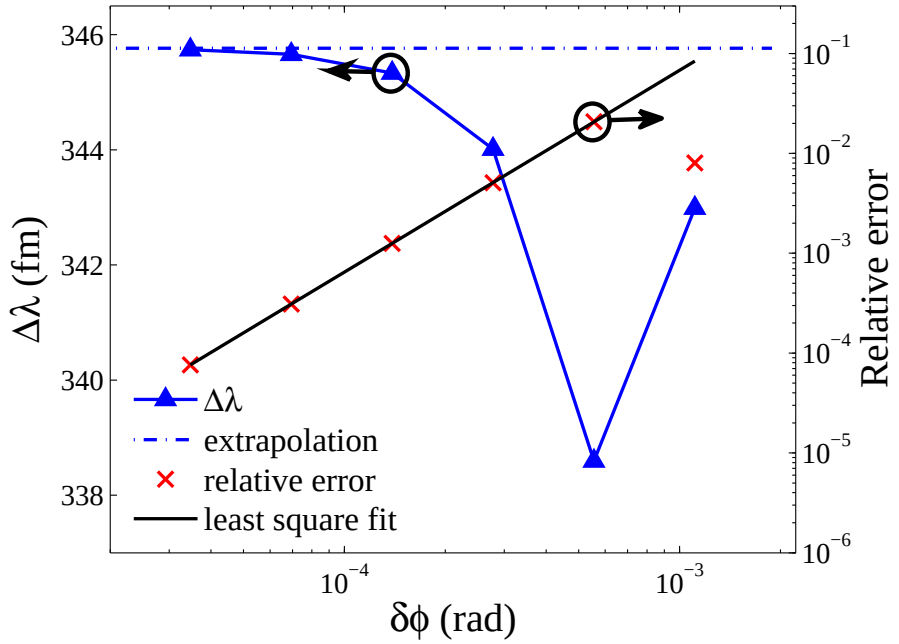

(a)

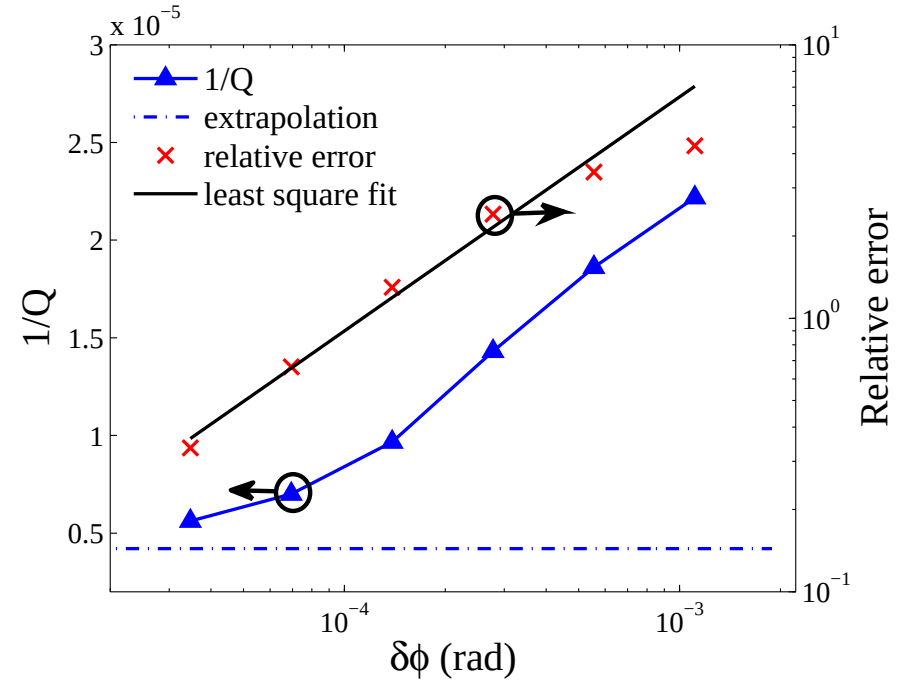

(b)

Figure 3.8: Shift and Q factor vs. grid spacing $\delta\phi$ along the $\hat{\phi}$ direction for a 50-nm radius gold bead. The last point is omitted for the creation of the line of best fit.

In Fig. 3.8 we further investigate the convergence rate of the calculated shift and Q-factor as a function of azimuthal angle discretization in the case of a 50-nm radius gold bead binding to the toroid. The percent error was calculated by comparing the results of each $\delta\phi$ to the expected result obtained through the Richardson extrapolation procedure (Appendix A.1). One can observe that the simulated resonance wavelength shift converges on the order of $O(\delta\phi^2)$ (black line in Fig. 3.8(a)) while the convergence rate of Q is $O(\delta\phi^{0.9})$(black line in Fig. 3.8(b)). A higher convergence rate is possible by implementing higher order integration procedures to evaluate (3.23) and (3.24).

3.6 Comparison with The First Order Perturbation Method

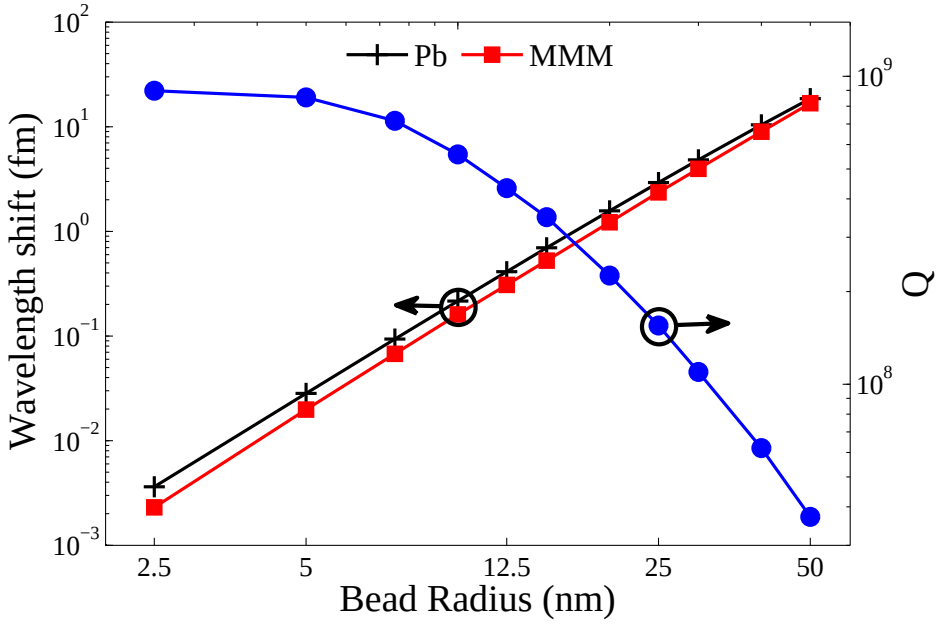

Figure 3.9: Binding shift and Q factor degradation due to a bound PS sphere for different bead radii.

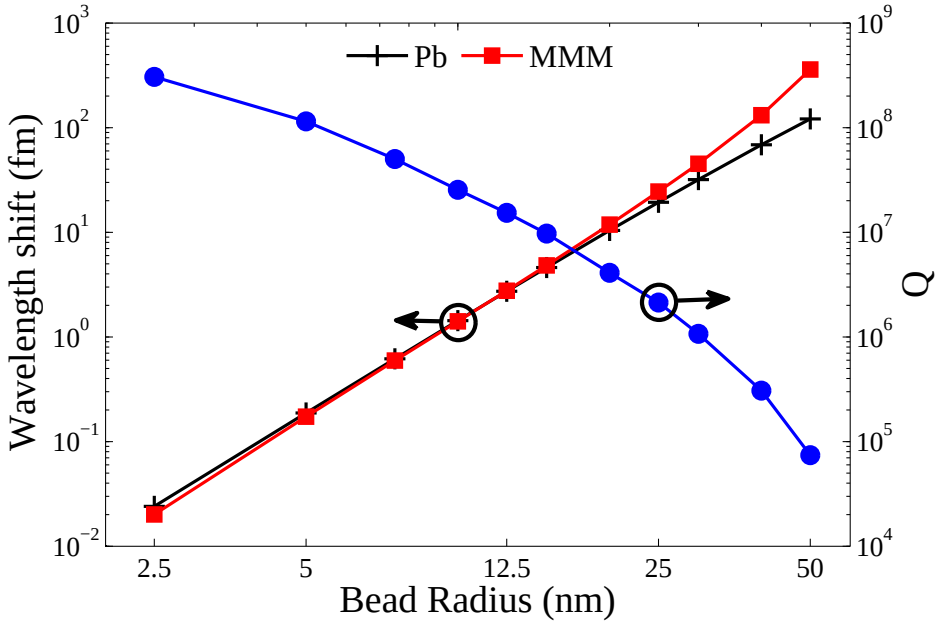

Figure 3.10: Binding shift and Q factor degradation due to a bound Au sphere for different bead radii.

In Fig. 3.9 and 3.10, we display the resonance wavelength shifts and the degraded Q factors due to the binding of a polystyrene and gold bead, respectively, of different radii, where an unperturbed toroid has a resonant wavelength of 632.747-nm and a theoretical Q factor of 1.65×10^9. The resonance shifts predicted by MMM (red solid square markers) are compared with those predicted by a first order perturbation method (black plus symbol markers). For PS beads, MMM predicts wavelength shifts which are in good agreement with those predicted by the first order perturbation method. The quality factor (blue solid circle markers) of the toroid is unaffected when a bead with radius smaller than 5-nm is attached to the surface, yet there is a drop to approximately 10^7 if a 50-nm radius bead is attached instead. The calculated wavelength shift and quality factor degradation is in line with the experimental observation reported in [9].

For the case of a gold bead simulation, the excess polarizability is given by $\alpha = 4\pi R^3 \epsilon_m(\epsilon_p - \epsilon_m)/(\epsilon_p + 2\epsilon_m)$ [33] where ϵ_p and ϵ_m are the permittivities of the particle and the medium, respectively. MMM predicts resonance shifts from 2×10^{-2} to 359-fm and Q factor degradation from 3×10^8 to 7.5×10^4 when the attached gold bead radius increases from 2.5-nm to 50-nm. As expected, at an off-plasmon resonance wavelength

of 633-nm, the perturbation method matches the MMM results when the bead size is below 20-nm yet for large beads yields greater errors due to the non-negligible field distortion from the bead.

In Fig. 3.11 we also compared the shifts calculated by the two methods as a function of wavelengths. As illustrated, near the surface plasmon resonance of a gold nanobead (540-nm, as shown in the insert), the accuracy of the perturbation method drops below 50% due to the strong surface plasmon effect that was similarly observed in [18].

To verify our formulation we further compared our results with reported experiments. We simulated the binding of 27.5-nm gold beads to a 50-μm radius microsphere with a 4-nm inter-particle gap as reported in [11, 47]. In this simulation, we obtained a resonance wavelength shift of 32.6-fm per bead adsorption. Compared to the total resonance shift in Fig. 1(d) of [11], we predict that a total of 10 beads are adsorbed to the microsphere surface. Knowing that an unperturbed cavity quality factor of 3×10^6 was reported in the same paper, we estimated that the quality factor will drop to 5.8×10^5 by the adsorption of 10 beads. This value is in good agreement with the reported experimental value on the order of 10^5.

It is worth noting that the MMM developed in this paper assumes that the cavity operates in a single whispering-gallery-mode. In practice, a WGM may contain multiple propagating modes and so omitting the coupling between different modes could decrease the accuracy of the model. A MMM formulation involving multiple WGM modes is possible, albeit at the expense of higher computational resource requirements.

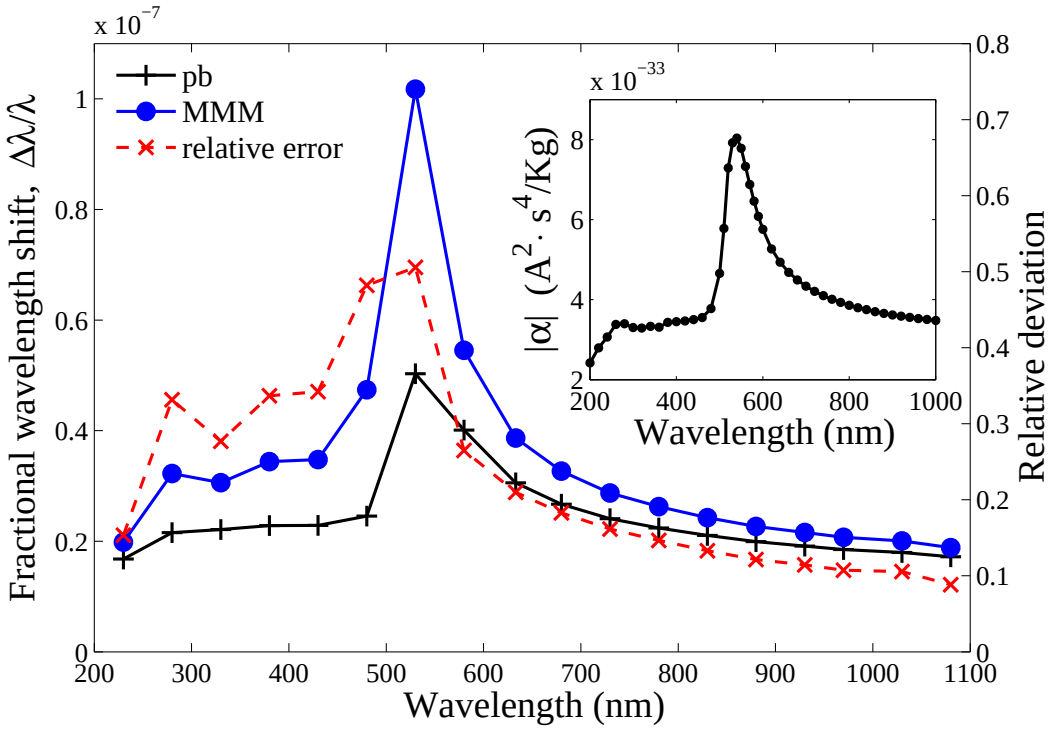

Figure 3.11: Cavity resonance shifts as a function of wavelengths for a 25-nm radius gold bead. The insert shows the excess polarizability of the bead at different wavelengths.

Chapter 4

Multi-Mode Mode-Matching Analysis

The single mode mode-matching-method presented in the previous chapter provides a simple, elegant, rigorous, and highly efficient solution for WGMs and WGM-nano particle hybrid modes. The coupling between different modes in the later case is negligible due to small sizes of the bound particles. For the purpose of generalization, in this chapter the mode matching method analysis involving multiple modes will be developed. To do so, the complete mode set is adopted in the local eigen mode expansion process. A numerical modal of a microtoroid resonator coupled to a silicon on insulator (SOI) waveguide will be presented. The example shows strong mutual coupling between the modal field.

4.1 Theoretical Formulations

Assume a M^{th}-order whispering gallery mode of an ideal or axisymmetric whispering-gallery-mode cavity has an electrical field distribution $\hat{e}'_M$ whose amplitude is normalized such that the energy stored in the cavity is 1 Joule. The resonance wavelength of this mode is λ_0 and the intrinsic quality factor is Q_0. If the axisymmetry of the cavity is perturbed between the azimuthal angle ϕ_0 and $\phi_0 + \Delta\phi$, the cavity will witness a shift in resonance and a degradation in the Q-factor. In the subsequent treatment, we presume that the light at a wavelength $\tilde{\lambda}$ close to the unperturbed cavity resonance wavelength is propagating inside the cavity.

For convenience, we further assume the light propagating in the M^{th}-order mode

in the unperturbed region of the cavity with an electrical field distribution $\mathbf{E}(\rho, z, \phi) = a\hat{e}'_M e^{jM\phi}$ and $|a|^2$ is the total energy stored in the cavity in the units of Joules. At the entrance angle of $\phi = \phi_0$ of the perturbed region, the electrical field can be expanded onto the normalized eigenmodes $\hat{\mathbf{e}}_l(\rho, z, \phi_0)$ at ϕ_0 according to:

$$\mathbf{E}(\rho, z, \phi_0) = \sum_l A_l(\phi_0)\hat{\mathbf{e}}_l(\rho, z, \phi_0) \tag{4.1}$$

Note here in contrast to the mode of the ideal cavity $\hat{e}'_M$, $\hat{\mathbf{e}}_l(\rho, z, \phi_0)$ is a complete set of orthonormal hybrid modes of an artificial ideal WGMs whose refrective index at any azimuthal cross section is identical to the profile at $\phi = \phi_0$. The orthonormality condition of the eigenmodes, for a Kronecker delta δ_{lk} with eigenmode indices l and k, is

$$\frac{1}{2}\epsilon_0 \int \epsilon_r(\rho, z, \phi_0 + \delta\phi)\hat{\mathbf{e}}_l(\rho, z, \phi_0) \cdot \hat{\mathbf{e}}^*_k(\rho, z, \phi_0) 2\pi\rho d\rho dz = \delta_{lk} \tag{4.2}$$

After propagating an infinitesimal azimuthal angle $\delta\phi$, we then obtain the electric field at $\phi_0 + \delta\phi$ by propagating the eigenmodes:

$$\mathbf{E}(\rho, z, \phi_0 + \delta\phi) = \sum_l A_l(\phi_0)\hat{\mathbf{e}}_l(\rho, z, \phi_0)e^{jm_l(\phi_0)\delta\phi} \tag{4.3}$$

where m_l is the complex azimuthal mode order of the l^{th} mode at the operating wavelength. Its real and imaginary parts are [78],

$$\begin{array}{rcl} \mathrm{Re}\{m_l(\phi_0)\} & = & M\frac{\lambda_{res,l}(\phi_0)}{\tilde{\lambda}} \\ \mathrm{Im}\{m_l(\phi_0)\} & = & m_{abs,l}(\phi_0) + m_{rad,l}(\phi_0) + ... \end{array} \tag{4.4}$$

On the other hand, $\mathbf{E}(\rho, z, \phi_0 + \delta\phi)$ can be expanded onto the new set of orthonormal modes at $\phi_0 + \delta\phi$:

$$\mathbf{E}(\rho, z, \phi_0 + \delta\phi) = \sum_l A_l(\phi_0 + \delta\phi)\hat{\mathbf{e}}_l(\rho, z, \phi_0 + \delta\phi) \tag{4.5}$$

By assigning a distinct mode index to (4.3), equating the right hand sides of (4.3) and (4.5), taking the dot product of both sides with $\frac{1}{2}\epsilon(\rho, z, \phi_0 + \delta\phi)\hat{\mathbf{e}}^*_k(\rho, z, \phi_0 + \delta\phi)$, and integrating over the whole space, we obtain the evolution of $A_k(\phi_0 + \delta\phi)$ according to

$$A_k(\phi + \delta\phi) = \sum_l A_l(\phi_0)e^{jm_l(\phi_0)\delta\phi}C_{k,l}(\phi_0) \tag{4.6}$$

where $C_{k,l}(\phi_0)$ is the coupling coefficient between the l^{th} mode at ϕ_0 and the k^{th} mode at $\phi_0 + \delta\phi$:

$$C_{k,l}(\phi_0) = \frac{1}{2}\epsilon_0 \int \epsilon_r(\rho, z, \phi_0 + \delta\phi)\hat{\mathbf{e}}_l(\rho, z, \phi_0) \cdot \hat{\mathbf{e}}_k^*(\rho, z, \phi_0 + \delta\phi)2\pi\rho d\rho dz \tag{4.7}$$

Thus the coefficient vector $\widetilde{A}(\phi_0 + \delta\phi) = [A_1(\phi_0 + \delta\phi)A_2(\phi_0 + \delta\phi)...]$ can be calculated from previous cross-sections as

$$\widetilde{A}(\phi_0 + \delta\phi) = \widetilde{C}(\phi_0) \cdot \widetilde{D}(\phi_0) \cdot \widetilde{A}(\phi_0) \tag{4.8}$$

where $\widetilde{C}(\phi_0)$ is the coupling matrix defined in (4.7) and $\widetilde{D}(\phi_0)$ is a diagonal propagation matrix with nonzero elements defined as

$$D_{kk}(\phi_0) = e^{jm_k(\phi_0)\delta\phi} \tag{4.9}$$

By propagating the field one round trip, one can calculate the overall resonance wavelength and quality factor of the cavity. For simplicity, a single mode $\hat{\mathbf{e}}_\mathbf{1}$ serves as the input at $\phi = 0$. After $N = 2\pi/\delta\phi$ steps (i.e. one round trip), the field can be computed by cascading (4.8):

$$\widetilde{A}(2\pi) = [\prod_{i=0}^{N-1}(\widetilde{C}_i \cdot \widetilde{D_i})] \cdot \widetilde{A}(0) \tag{4.10}$$

It is shown in (4.10) that there are multiple modes existing in the resonator due to modal coupling from ϕ_0 to $\phi_0 + \Delta\phi$; however, all modes other than the input mode, as will be shown later, are at low energy levels. For the input mode, specifically, we can write

$$A_1(2\pi) = e^{j\bar{m_1}2\pi}A_1(0) \tag{4.11}$$

$\bar{m_1}$ is the overall complex mode order of the input mode after one round trip. The resonance wavelength λ_{res} and quality factor Q of the input WGM can be calculated using the complex mode order $\bar{m_1}$ as follows:

$$\lambda_{res} = \tilde{\lambda}\frac{\mathrm{Re}\{m_1\}}{M} \tag{4.12}$$

$$Q = \frac{M}{2\mathrm{Im}\{m_1\}} \tag{4.13}$$

4.2 Simulatoin Results

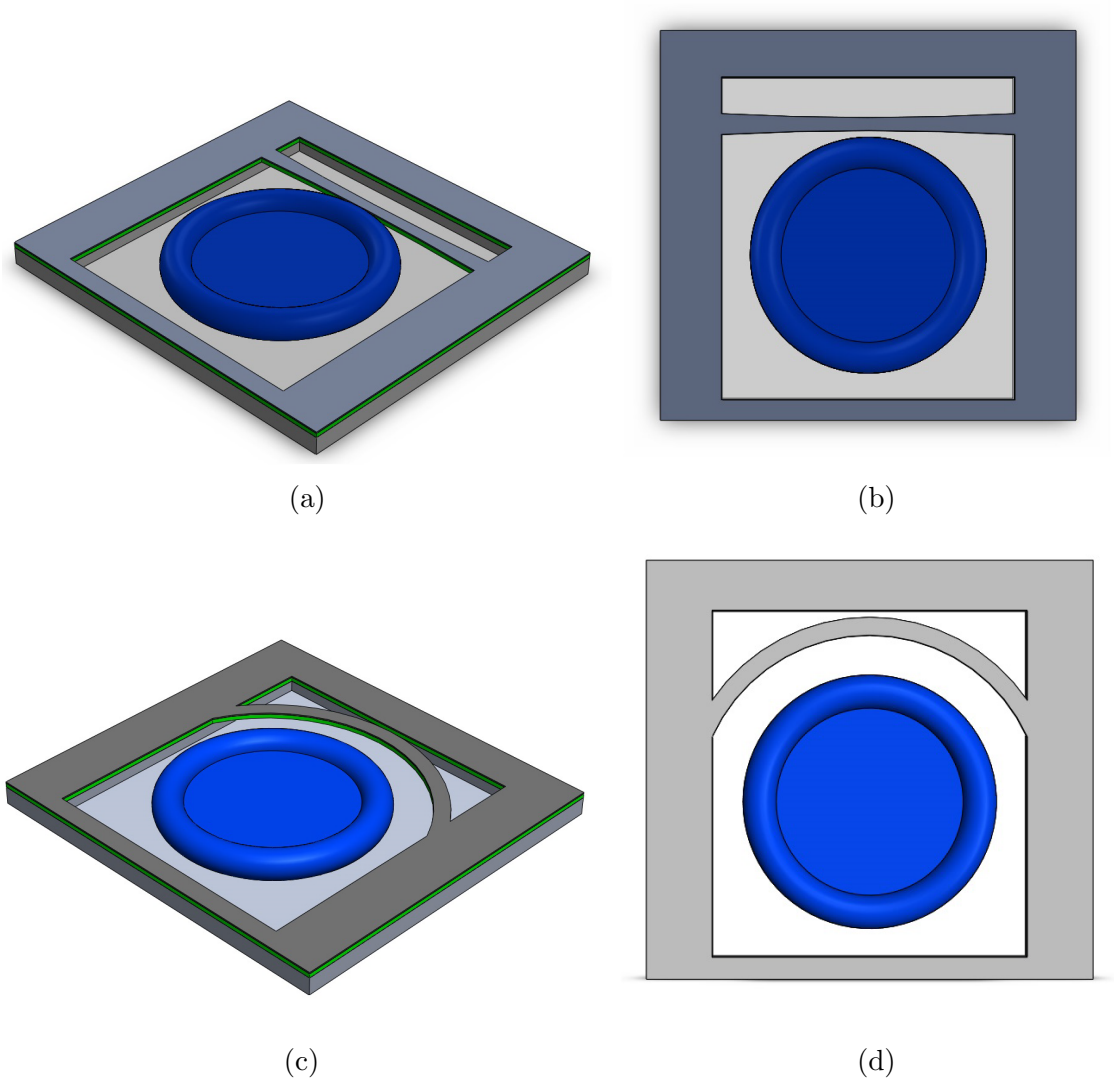

(a) (b)

(c) (d)

Figure 4.1: Coupling light into an on-chip microtoroid resonator using an SOI waveguide. (a) and (c) provides an isometric view of a straight and a convex bent waveguide configuration, respectively. (b) and (d) provides a top view.

In this test case we examine the coupling Q-factor of a microtoroid coupled to an SOI waveguide in air, as shown in Fig. 4.1. Such a coupling scheme is a promising avenue for on-chip integration of WGM microresonators. Equations (4.7-4.13) are

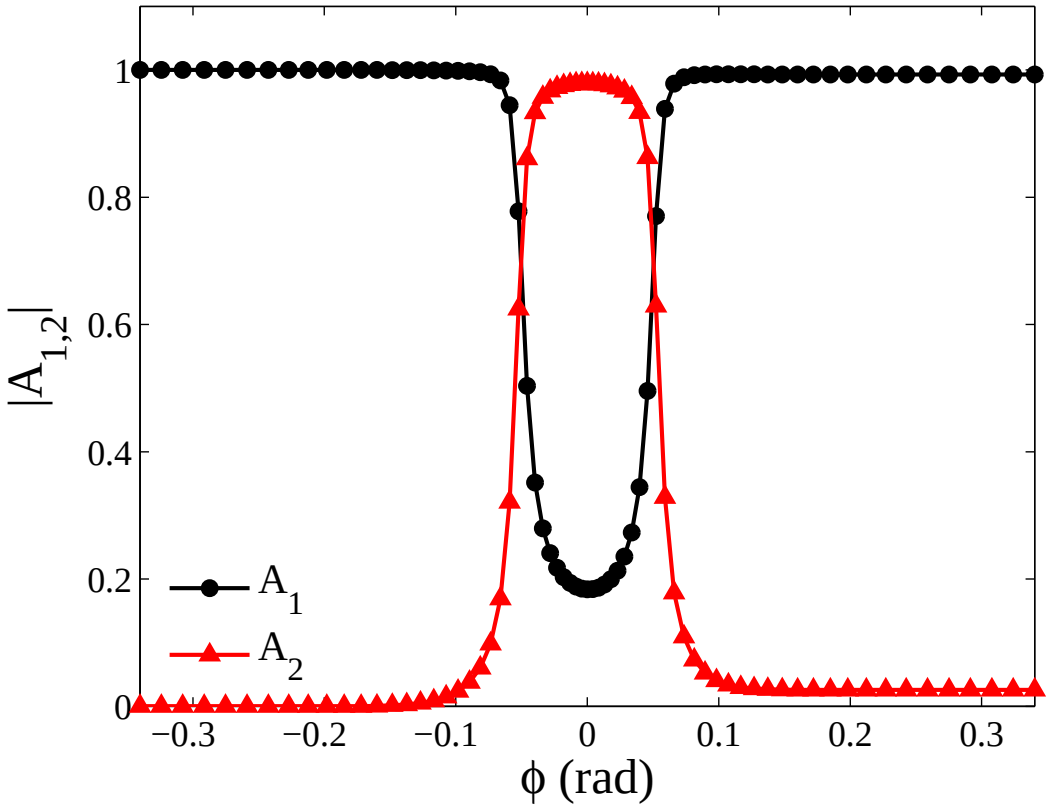

Figure 4.2: Evolution of the amplitudes $|A_1|$ and $|A_2|$ for the first two modes (i.e. the 289^{th} fundamental modes) along the propagation direction when a straight SOI waveguide is placed at the equator of a silica microtoroid. A fundamental quasi-TE cavity mode (mode 1) is launched at $\phi = -0.34$ rad and propagates along the $\hat{\phi}$ direction. Strong coupling between the 2 modes is witnessed from $\phi = -0.06$ to $\phi = 0.06$.

numerically verified at a wavelength of 1500-nm for a microtoroid with a major radius of 45-μm and a minor radius of 5-μm. The SOI waveguide under investigation has a width of 500 nm and is formed by an upper silicon layer of 220-nm thickness and a lower SiO_2 layer of 2-μm thickness. The refractive indices of silica (1.44462) and silicon (3.48206) are taken from literature [69, 88]. Two configurations for SOI waveguides are investigated: a straight SOI waveguide placed near the toroid (Fig. 4.1(a)(b)) and a concentric convex SOI waveguide placed at the toroid's equatorial plane (Fig. 4.1(c)(d)).

The first scenario consisting of the straight SOI waveguide contacting the microtoroid's equator is analyzed. The 289^{th} fundamental quasi-TE toroid mode is

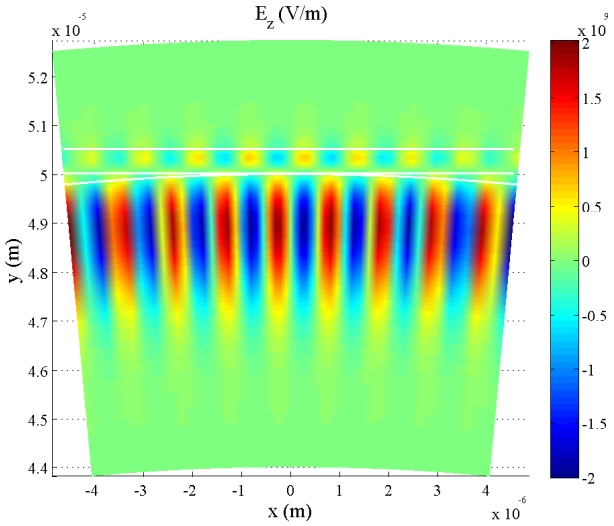

(a)

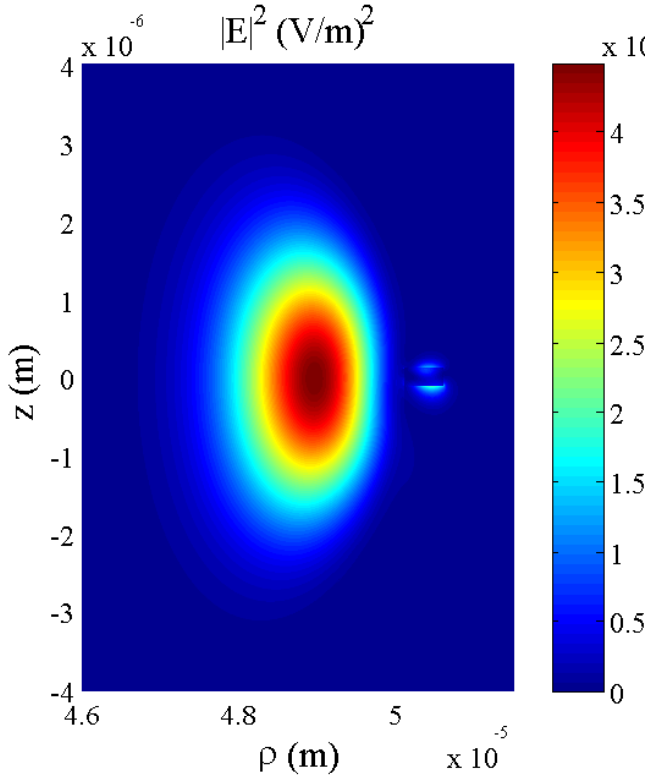

(b)

Figure 4.3: Field pattern for a straight fiber-toroid coupling system, where (a) is the top view and (b) is the cross-sectional view.

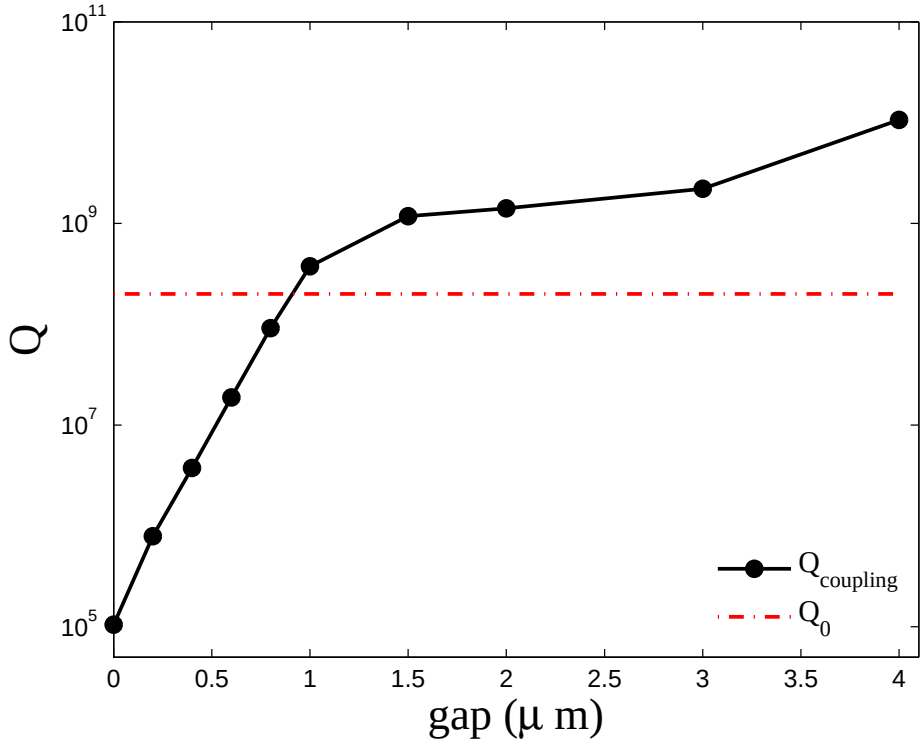

Figure 4.4: Coupling Q-factor of a microtoroid when a straight SOI waveguide is situated in the equatorial plane and separated from the cavity at different distances. The red dot-dashed line indicates the intrinsic Q-factor of the cavity.

launched at $\phi = -0.34$ rad, wherein the waveguide is 3 wavelengths away from the cavity. Beyond that point, the coupling between the cavity and the waveguide falls to a negligible level (with Q degradation below $10^{-8}\%$) and so it is disregarded. Fig. 4.2 shows the amplitudes of the first two modes during propagation. The first mode at the input and output is the fundamental quasi-TE mode and the second mode at the input and output is the fundamental quasi-TM mode. In the intermediate region (around $\phi = -0.06$ rad to $\phi = 0.06$ rad), these two modes become hybrid WGM-SOI modes and strong coupling takes place between them. Fig. 4.3 shows the field distribution in this region. Fig. 4.3(a) shows a top view of the cavity-waveguide coupling while Fig. 4.3(b) shows the cross-sectional field pattern.Energy is coupled back and forth between the first and second mode in a similar manner as that of a directional coupler. At the output end, the field is carried by both modes with A_1=0.9928 and A_2=0.0256 (i.e. energy carried by higher-order modes is further diminished), corresponding to a coupling Q-factor of 10^5.

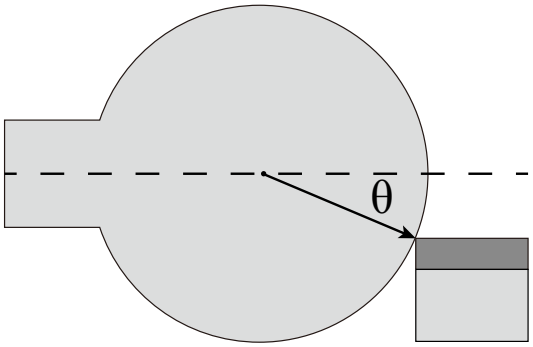

Figure 4.5: The angle θ used to specify the location of the contacting waveguide when it is placed off the equatorial plane.

We then shift our attention to the second scenario, wherein the SOI waveguide is displaced in the equatorial plane to determine a minimum gap distance between the waveguide and the toroid. The goal is to find the optimal location that satisfies the critical coupling condition, which in turn requires that the coupling Q-factor be equal to the intrinsic Q-factor of the cavity. Fig. 4.4 shows the coupling Q-factor as a function of the minimum gap distance. A $Q_{coupling}$ of 10^5 is computed when the waveguide touches the cavity surface and 10^{10} is computed at a gap size of 2.5 wavelengths. When the WGM resonator is placed in air, the absorption from the silica is small and consequently $Q_{coupling} = 10^{10}$. This Q-factor is in reality smaller than those due to other loss mechanisms, such as surface scattering and surface contamination (via water layer adsorption, etc.). An intrinsic Q-factor of 2×10^8, as has been measured in our group's laboratory, is adopted here. For a waveguide sitting in the equatorial plane, a gap size of 0.75 μm is also desirable in establishing critical coupling.

The precise control of gap sizes, however, can be challenging to accomplish in the fabrication process. Alternatively, one can keep the waveguide in contact with the cavity and move it vertically by adjusting the thickness of the insulator layer as to tune the value of the coupling Q-factor. In such configuration, we may pinpoint the location of the waveguide via an angle θ in respect to the equatorial plane, as illustrated in Fig. 4.5. The Q-factor as a function of θ is shown in Fig. 4.6, wherein

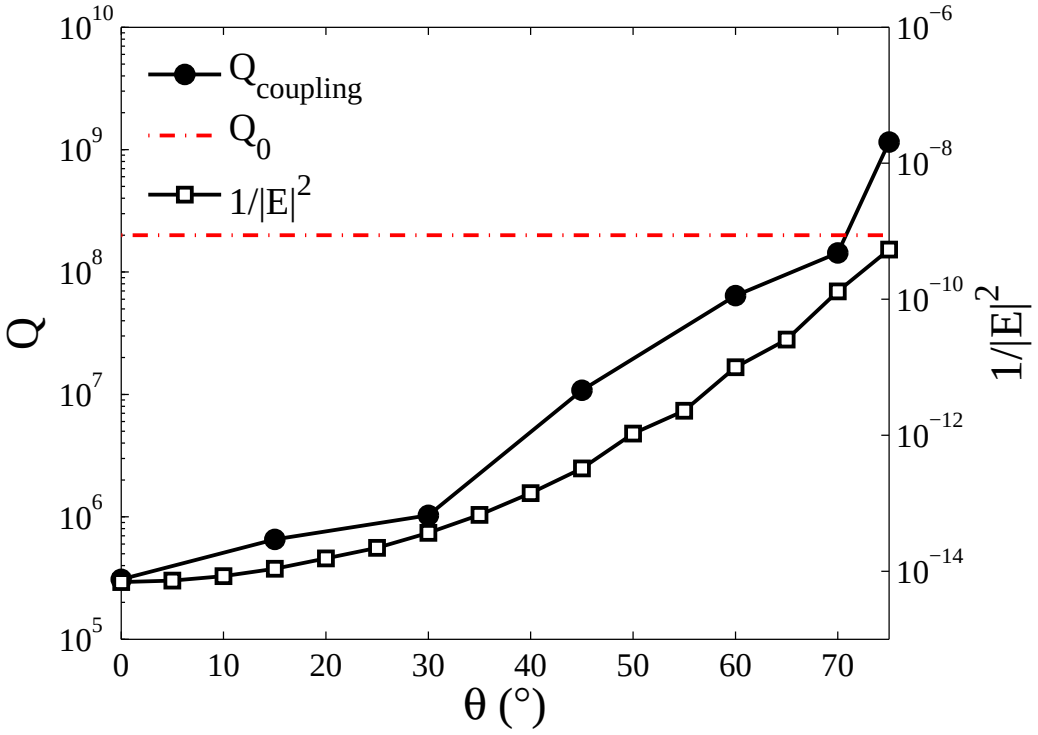

Figure 4.6: Coupling Q-factor of a microtoroid when a straight SOI waveguide mechanically contacts the cavity surface at different angles in respect to the equatorial plane. The axis to the right shows the reciprocal of the field intensity of the fundamental quasi-TE mode at different θ.

a Q-factor of 3×10^5 is calculated at $\theta = 0$. It is also worth mentioning that the $\theta = 0$ position (corresponding to the top surface of the SOI waveguide being aligned with the equator) is different from that in the previous case (i.e. the midplane of the silicon layer being aligned with the equator). At a larger θ, the local field intensity of the cavity mode is smaller. As a result, coupling between the cavity and the waveguide is weaker and a larger coupling Q-factor is observed. The right axis of Fig. 4.6 represents the inverse of the field intensity on the surface of the cavity at different θ. It is important to note that the Q-factor function resembles the intensity curve. For a straight SOI waveguide physically touching the toroid surface and that is placed below the equator, a waveguide location at $\theta = 65°$ is favourable for critical coupling purposes.

For the convex SOI waveguide configuration, a search is conducted to determine the optimal gap size when the waveguide is concentric with the microtoroid resonator

and situated in the equatorial plane. A coupling Q-factor of 2.7×10^4 is computed at a gap size of 0 and rises to $3.75 \times^1 0^{16}$ at a gap size of 2.5 wavelengths. An optimized gap distance for critical coupling is 1.1 μm in this case.

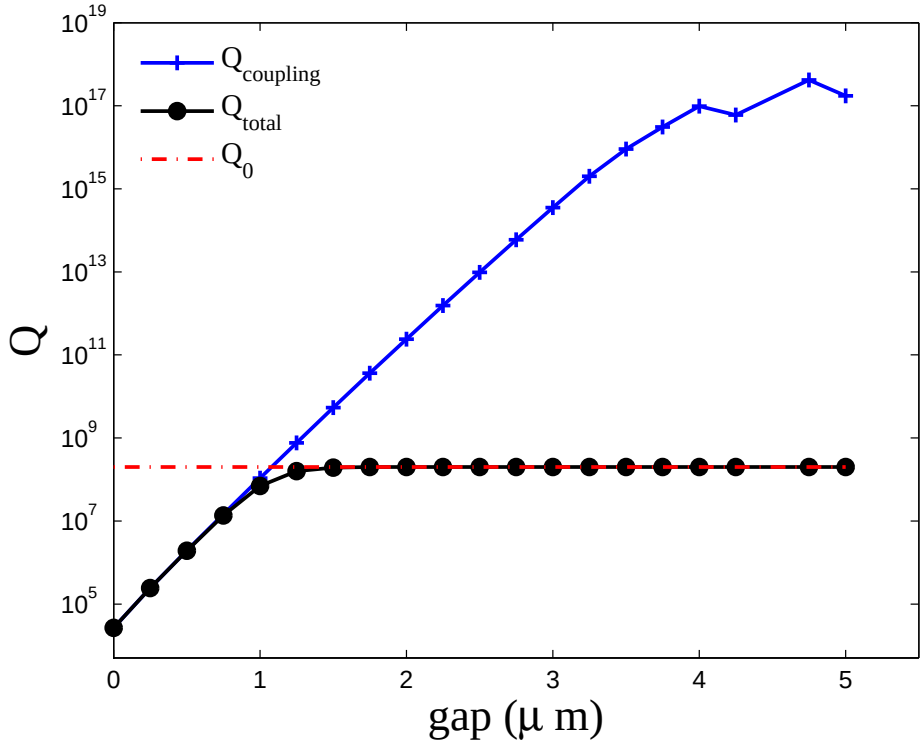

Figure 4.7: Q-factor of a silica microtoroid when a concentric convex SOI waveguide is situated in the equatorial plane at different gap sizes in respect to the resonator. The red dot-dashed line corresponds to the intrinsic Q-factor of the cavity.

4.3 Numerical Error

In Fig. 4.8 we inspect the convergence rate as a function of azimuthal angle discretization for a straight SOI waveguide at the toroid equator. The present error was estimated by comparing the results of each $\delta\phi$ to the expected result obtained through the Richardson extrapolation procedure. One can observe that the Q-factor convergence rate is $O(\delta\phi^{0.79})$ (depicted by the black line in Fig. 4.7).

Further, in Fig. 4.9 we investigate the convergence rate as a function of number of modes included in the calculation. Same as previous set up, a straight SOI waveguide is placed at the equator of the cavity. A convergence rate of $O(\delta\phi^{0.84})$ is observed.

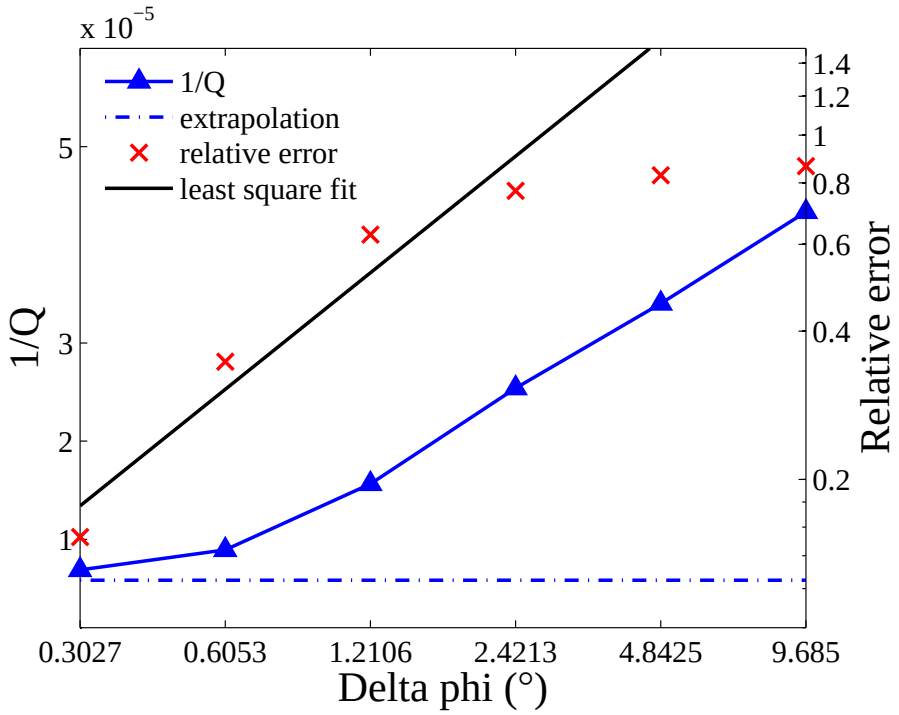

Figure 4.8: Q-factor versus grid spacing $\delta\phi$ along the $\hat{\phi}$ direction for a straight SOI waveguide placed at the equator of a microtoroid. The last two points are omitted for the creation of the line of best fit.

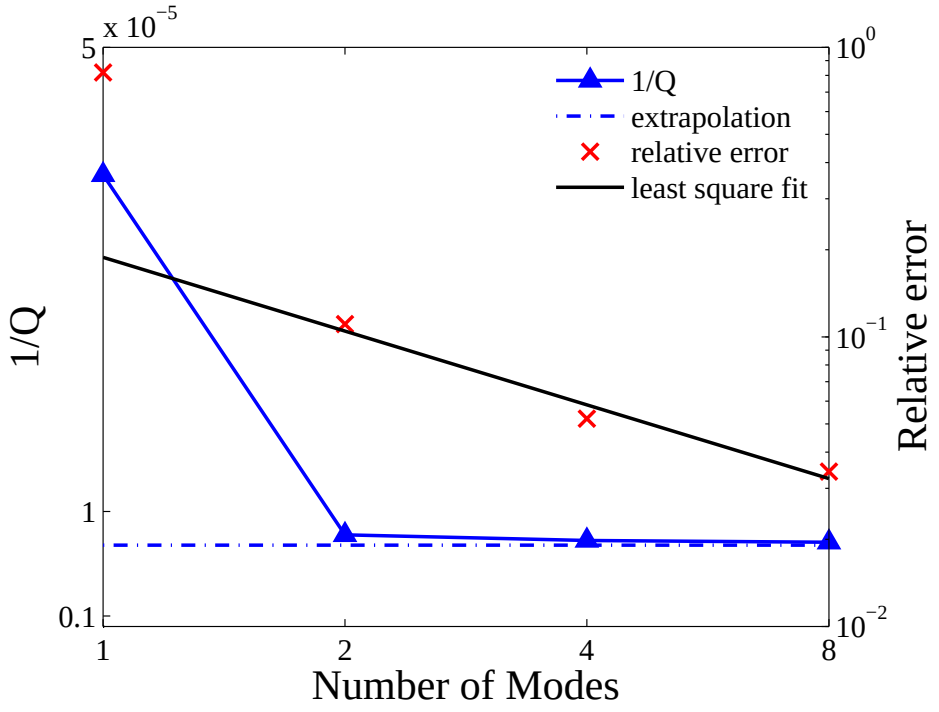

Figure 4.9: Q-factor versus number of modes involved in the calculation for a straight SOI waveguide placed at the equator of a microtoroid. The first point is omitted for the creation of the line of best fit.

Chapter 5

Conclusions

5.1 Summarization

A finite-element-method based mode-matching analysis for whispering-gallery-mode cavities has been developed. By expanding the total field onto the eigenmodes in each transverse cross section, such a method can simulate how light circulates inside the cavity. Firstly, it is demonstrated that the method is able to describe an ideal axisymmetric whispering-gallery-mode cavity, a case that has been thoroughly studied in previous work. All the conclusions from previous work can be repeated by the mode-matching formulations. Moreover, the method shows the capability to solve whispering-gallery-mode cavities that do no possess axial symmetries, a problem that has been haunting the academy for decades. By discretizing the 3-D structure over the azimuthal dimension, only 2-D mode solvers are required to search the local eigen modes. This way, the technique is highly computationally efficient. To verify the theory and formulations, two test cases are studied numerically.

Firstly, a single mode-matching analysis have been performed by tracing the fundamental mode in the cavity. The method shows an ease of numerical application and demonstrates high efficiency by reducing the consumed memory by a factor of 90 compared with a 3-D FEM modal [77]. To demonstrate the validity of the method, numerical results for a microtoroid bound with a plasmonic and non-plasmonic bead are presented. Results obtained from the simulation are consistent with those obtained through a first order perturbation method and experimental demonstrations. Finally, the numerical error that origins from the discretization of azimuthal direction $\hat{\phi}$ is discussed.

Furthermore, a multi-mode matching analysis has been developed by considering the coupling between modal field. The method is applied to design a whispering gallery cavity-silicon on insulator waveguide system. Two different SOI waveguide configurations are investigated and a set of optimum designs for critical coupling are discussed. A whispering gallery mode cavity-silicon on insulator waveguide coupling scheme is demonstrated to be achievable through the analysis.

Overall, the mode-matching-method for whispering-gallery-mode cavities developed in this thesis is demonstrated to be a powerful tool for the research and application of whispering gallery mode cavities. Current problems in this area that can be modeled by this technique includes: modeling a surface binding event [9, 70], designing a nano antenna-whispering gallery cavity bio-senser [50, 47], designing an optimum cavity-waveguide coupling system [32, 12], analyzing non-axisymmetric cavities [71], such as elliptical microcavities and spiral microcavities [25], and designing micoricavity arrays [89].

5.2 Future Work

A bi-directional mode-matching method needs to be developed to include both forward propagating and backward propagating modal field. Back scattering inside a whispering-gallery-mode cavity origins from the surface roughness and Rayleigh scattering. Because of the high Q property of the cavity, back-scattered light can build up high energy level. A bi-directional mode-matching-method will be able to modal the 'split frequency' phenomenon witnessed in previous work [9]. Moreover, a bi-directional mode-matching-method can include both transmission and reflection in the modal thus will complete the whole theory.

Bibliography

[1] Baron Rayleigh, John William Strutt. *The Theory of Sound*. New York, Dover Publications, 1st edition, 1878.

[2] R. D. Richtmyer. Dielectric resonators. *J. Appl. Phys.*, 10(6):391, December 1939.

[3] A. Ashkin and J. M. Dziedzic. Observation of resonances in the radiation pressure on dielectric spheres. *Physical Review Letters*, 38(23):1351–1355, June 1977.

[4] H. E. Benner, P. W. Barber, J. F. Owen, and B. K. Chang. Observation of structure resonances in the fluorescence spectra from microspheres. *Physical Review Letters*, 44(7):475–478, February 1980.

[5] V.B. Braginsky, M.L. Gorodetsky, and V.S. Ilchenko. Quality-factor and nonlinear properties of optical whispering-gallery modes. *Phys. Lett. A*, 137(7):393 – 397, 1989.

[6] J. R. Buck and H. J. Kimble. Optimal sizes of dielectric microspheres for cavity QED with strong coupling. *Phys. Rev. A: At., Mol., Opt. Phys.*, 67:033806, Mar 2003.

[7] S. M. Spillane, T. J. Kippenberg, and K. J. Vahala. Ultralow-threshold raman laser using a spherical dielectric microcavity. *Nature*, 415(6872):621–623, February 2002.

[8] Giora Griffel, Stephen Arnold, Dogan Taskent, Ali Serpengüzel, John Connolly, and Nancy Morris. Excitation of morphology dependent resonances of microspherical cavities using optical fibers. *Opt. Photon. News*, 6(12):21–22, Dec 1995.

[9] Tao Lu, Hansuek Lee, Tong Chen, Steven Herchak, Ji-Hun Kim, Scott E. Fraser, Richard C. Flagan, and Kerryra Vahala. High sensitivity nanoparticle detection using optical microcavities. *Proc. Natl. Acad. Sci. U. S. A.*, 2011.

[10] S. I. Shopova, R. Rajmangal, S. Holler, and S. Arnold. Plasmonic enhancement of a whispering-gallery-mode biosensor for single nanoparticle detection. *Appl. Phys. Lett.*, 98(24):243104, 2011.

[11] M.A. Santiago-Cordoba, S.V. Boriskina, F. Vollmer, and M.C. Demirel. Nanoparticle-based protein detection by optical shift of a resonant microcavity. *Appl. Phys. Lett.*, 99:073701, 2011.

[12] S.M. Spillane, T. J. Kippenberg, O. J. Painter, and K. J. Vahala. Ideality in a fiber-taper-coupled microresonator system for application to cavity quantum electrodynamics. *Phys. Rev. Lett.*, 91(4):043902, July 2003.

[13] M. L. Gorodetsky and V. S. Ilchenko. Optical microsphere resonators: optimal coupling to high-q whispering-gallery modes. *Journal of the Optical Society of America B: Optical Physics*, 16(1):147–154, Jan 1999.

[14] M. Oxborrow. Traceable 2-D finite-element simulation of the whispering-gallery modes of axisymmetric electromagnetic resonators. *IEEE Trans. Microwave Theory Tech.*, 55(6):1209 –1218, june 2007.

[15] Bing-Jing Li and Pao-Lo Liu. Numerical analysis of the whispering gallery modes by the finite-difference time-domain method. *Quantum Electronics, IEEE Journal of*, 32(9):1583–1587, 1996.

[16] Mohammad Amin Cheraghi Shirazi, Wenyan Yu, Serge Vincent, and Tao Lu. Cylindrical beam propagation modelling of perturbed whispering-gallery modemicrocavities. *Opt. Express*, 21(25):30243–30254, Dec 2013.

[17] Iwao Teraoka, Stephen Arnold, and Frank Vollmer. Perturbation approach to resonance shifts of whispering-gallery modes in a dielectric microsphere as a probe of a surrounding medium. *J. Opt. Soc. Am. B*, 20(9):1937–1946, Sep 2003.

[18] Matthew R Foreman and Frank Vollmer. Theory of resonance shifts of whispering gallery modes by arbitrary plasmonic nanoparticles. *New J. Phys.*, 15(8):083006, 2013.

[19] Kai Jiang and Wei-Ping Huang. Finite-difference-based mode-matching method for 3-d waveguide structures under semivectorial approximation. *J. Lightwave Technol.*, 23(12):4239–4248, 2005.

[20] Jingliang Zheng and Ming Yu. Rigorous mode-matching method of circular to off-center rectangular side-coupled waveguide junctions for filter applications. *IEEE Trans. Microwave Theory Tech.*, 55(11):2365–2373, 2007.

[21] Matt Biddulph. St paul's cathedral from the whispering gallery, July 2009.

[22] http://templeofheavenbeijing.com/tag/whispering gallery/, N.d.

[23] Gustav Mie. Beitrge zur optik trber medien, speziell kolloidaler metallsungen. *Annalen der Physik*, 330:377–445, 1908.

[24] P. Debye. Der lichtdruck auf kugeln von beliebigem material. *Annalen der Physik*, 335:57–136, 1909.

[25] Hansuek Lee, Tong Chen, Jiang Li, Oskar Painter, and Kerry J. Vahala. Ultra-low-loss optical delay line on a silicon chip. *Nat Commun*, 3:867–, May 2012.

[26] Hermann A. Haus. *Electromagnetic Noise and Quantum Optical Measurements*. Springer, 2000.

[27] M. L. Gorodetsky, A. A. Savchenkov, and V. S. Ilchenko. Ultimate Q of optical microsphere resonators. *Opt. Lett.*, 21(7):453–455, Apr 1996.

[28] KJ Vahala. Optical microcavities. *Nature*, 424(6950):839–846, AUG 14 2003.

[29] Kartik Srinivasan, Matthew Borselli, Oskar Painter, Andreas Stintz, and Sanjay Krishna. Cavity q, mode volume, and lasing threshold in small diameter algaas microdisks with embedded quantum dots. *Opt. Express*, 14(3):1094–1105, Feb 2006.

[30] J. Ctyroky, L. Prkna, and M. Hubalek. Rigorous vectorial modelling of microresonators. In *Transparent Optical Networks, 2004. Proceedings of 2004 6th International Conference on*, volume 2, pages 281–286 vol.2, 2004.

[31] Yasuki Ido, Yasuaki Masumoto, Fumio Sasaki, Masahiko Mori, Satoshi Haraichi, and Shu Hotta. Reduced lasing threshold in thiophene/phenylene co-oligomer crystalline microdisks. *Applied Physics Express*, 3(1):012702, 2010.

[32] Ming Cai, Oskar Painter, and Kerry J. Vahala. Observation of critical coupling in a fiber taper to a silica-microsphere whispering-gallery mode system. *Phys. Rev. Lett.*, 85(1):74–77, July 2000.

[33] Stefan A. Maier. *Plasmonics: Fundamentals and Applications*. Berlin: Springer, 2007.

[34] P. B. Johnson and R. W. Christy. Optical constants of the noble metals. *Phys. Rev. B: Condens. Matter Mater. Phys.*, 6:4370–4379, Dec 1972.

[35] R. Gordon. Surface plasmon nanophotonics: A tutorial. *Nanotechnology Magazine, IEEE*, 2(3):12–18, 2008.

[36] John David Jackson. *Classical Electrodynamics*. Wiley, 1975.

[37] George M. Hale and Marvin R. Querry. Optical constants of water in the 200-nm to 200-µm wavelength region. *Appl. Opt.*, 12(3):555–563, Mar 1973.

[38] Kuiru Li, Mark I. Stockman, and David J. Bergman. Self-similar chain of metal nanospheres as an efficient nanolens. *Phys. Rev. Lett.*, 91:227402, Nov 2003.

[39] Jiri Homola. Surface plasmon resonance sensors for detection of chemical and biological species. *Chemical Reviews*, 108(2):462–493, 2008. PMID: 18229953.

[40] Amanda J. Haes and Richard P. Van Duyne. A nanoscale optical biosensor:sensitivity and selectivity of an approach based on the localized surface plasmon resonance spectroscopy of triangular silver nanoparticles. *Journal of the American Chemical Society*, 124(35):10596–10604, 2002. PMID: 12197762.

[41] J. A. H. van Nieuwstadt, M. Sandtke, R. H. Harmsen, F. B. Segerink, J. C. Prangsma, S. Enoch, and L. Kuipers. Strong modification of the nonlinear optical response of metallic subwavelength hole arrays. *Phys. Rev. Lett.*, 97:146102, Oct 2006.

[42] Katrin Kneipp, Yang Wang, Harald Kneipp, Lev T. Perelman, Irving Itzkan, Ramachandra R. Dasari, and Michael S. Feld. Single molecule detection using surface-enhanced raman scattering (sers). *Phys. Rev. Lett.*, 78:1667–1670, Mar 1997.

[43] Shuming Nie and Steven R. Emory. Probing single molecules and single nanoparticles by surface-enhanced raman scattering. *Science*, 275(5303):1102–1106, 1997.

[44] Maurizio Righini, Giovanni Volpe, Christian Girard, Dmitri Petrov, and Romain Quidant. Surface plasmon optical tweezers: Tunable optical manipulation in the femtonewton range. *Phys. Rev. Lett.*, 100:186804, May 2008.

[45] D. M. Schaadt, B. Feng, and E. T. Yu. Enhanced semiconductor optical absorption via surface plasmon excitation in metal nanoparticles. *Applied Physics Letters*, 86(6):–, 2005.

[46] S. Arnold, D. Keng, S. I. Shopova, S. Holler, W. Zurawsky, and F. Vollmer. Whispering gallery mode carousel – a photonic mechanism for enhanced nanoparticle detection in biosensing. *Opt. Express*, 17(8):6230–6238, Apr 2009.

[47] Miguel A. Santiago-Cordoba, Murat Cetinkaya, Svetlana V. Boriskina, Frank Vollmer, and Melik C. Demirel. Ultrasensitive detection of a protein by optical trapping in a photonic-plasmonic microcavity. *J. Biophotonics*, 5(8-9):629–638, 2012.

[48] Lukas Novotny, Randy X. Bian, and X. Sunney Xie. Theory of nanometric optical tweezers. *Phys. Rev. Lett.*, 79:645–648, Jul 1997.

[49] S. I. Shopova, R. Rajmangal, Y. Nishida, and S. Arnold. Ultrasensitive nanoparticle detection using a portable whispering gallery mode biosensor driven by a periodically poled lithium-niobate frequency doubled distributed feedback laser. *Rev. Sci. Instrum.*, 81:103110, 2010.

[50] Stephen Arnold, Venkata Ramanaiah Dantham, Curtis Barbre, Bruce A. Garetz, and Xudong Fan. Periodic plasmonic enhancing epitopes on a whispering gallery mode biosensor. *Opt. Express*, 20(24):26147–26159, Nov 2012.

[51] Anthony J. Campillo Richard Kounai Chang, editor. *Optical processes in microcavities*. World Scientific, 1996.

[52] I. G. Wilson, C. W. Schramm, and J. P. Kinzer. High q resonant cavities for microwave testing. *Bell System Technical Journal*, 25(3):408–434, 1946.

[53] N.McN. Alford, J. Breeze, S.J. Penn, and M. Poole. Layered al2o3-tio2 composite dielectric resonators with tuneable temperature coefficient for microwave applications. *Science, Measurement and Technology, IEE Proceedings* -, 147(6):269–273, 2000.

[54] Jan Wiersig. Boundary element method for resonances in dielectric microcavities. *J. Opt. A: Pure Appl. Opt.*, 5(1):53, 2003.

[55] Chang-Ling Zou, Yong Yang, Yun-Feng Xiao, Chun-Hua Dong, Zheng-Fu Han, and Guang-Can Guo. Accurately calculating high quality factor of whispering-gallery modes with boundary element method. *J. Opt. Soc. Am. B*, 26(11):2050–2053, Nov 2009.

[56] Chang-Ling Zou, Harald G. L. Schwefel, Fang-Wen Sun, Zheng-Fu Han, and Guang-Can Guo. Quick root searching method for resonances of dielectric optical microcavities with the boundary element method. *Opt. Express*, 19(17):15669–15678, Aug 2011.

[57] Tao Lu and David Yevick. A vectorial boundary element method analysis of integrated optical waveguides. *J. Lightw. Technol.*, 21(8):1793–1807, August 2003.

[58] Tao Lu and David Yevick. Boundary element analysis of dielectric waveguides. *J. Opt. Soc. Am. A:*, 19(6):1197 – 1206, June 2002.

[59] J. Krupka, D. Cros, M. Aubourg, and P. Guillon. Study of whispering gallery modes in anisotropic single-crystal dielectric resonators. *Microwave Theory and Techniques, IEEE Transactions on*, 42(1):56–61, 1994.

[60] J.A. Monsoriu, M.V. Andres, E. Silvestre, A. Ferrando, and B. Gimeno. Analysis of dielectric-loaded cavities using an orthonormal-basis method. *Microwave Theory and Techniques, IEEE Transactions on*, 50(11):2545–2552, 2002.

[61] R.L.Courant. Variational methods for the solution of problems of equilibrium and viration. *Bull. Amer. Math. Soc*, 49(1):1–23, 1943.

[62] P.P.Silverster. Finite element solution of homogeneous waveguide problems. *Alta Freq.*, 38:313–317, 1969.

[63] Tobias Jan August Kippenberg. *Nonlinear Optics in Ultra-High-Q Whispering-Gallery Optical Microcavities*. PhD thesis, California Institute of Technology, 2004.

[64] M. Aubourg and P. Guillon. A mixed finite element formulation for microwave devices problems. application to mis structure. *Journal of Electromagnetic Waves and Applications*, 5(4-5):371–386, 1991.

[65] D.G. Santiago, R.T. Wang, G.J. Dick, R.A. Osegueda, J.H. Pierluissi, L.M. Gil, A. Revilla, and G.J. Villalva. Experimental test and application of a 2-d finite element calculation for whispering gallery sapphire resonators. In *Frequency Control Symposium, 1994. 48th., Proceedings of the 1994 IEEE International*, pages 482–485, 1994.

[66] J. F Lee, G.M. Wilkins, and R. Mitra. Finite-element analysis of axisymmetric cavity resonator using a hybrid edge element technique. *Microwave Theory and Techniques, IEEE Transactions on*, 41(11):1981–1987, 1993.

[67] R. Osegueda, J. Pierluissi, L. Gil, A. Revilla, G. Villalva, G. Dick, D. Santiago, and R. Wang. *Azimuthally-dependent Finite Element Solution to the Cylindrical Resonator*. Univ. Texas, EI Paso. and Jet Propulsion Lab, California Inst. Technol., Pasadena, 1994.

[68] MI Cheema and AG Kirk. Accurate determination of the quality factor and tunneling distance of axisymmetric resonators for biosensing applications. *Opt Express*, 21(7):8724–8735–, April 2013.

[69] I. H. Malitson. Interspecimen comparison of the refractive index of fused silica. *J. Opt. Soc. Am.*, 55(10):1205–1208, Oct 1965.

[70] S. Arnold, M. Khoshsima, I. Teraoka, S. Holler, and F. Vollmer. Shift of whispering-gallery modes in microspheres by protein adsorption. *Opt. Lett.*, 28(4):272–274, Feb 2003.

[71] Jens U. Nockel and A. Douglas Stone. Ray and wave chaos in asymmetric resonant optical cavities. *Nature*, 385(6611):45–47, January 1997.

[72] M. Sumetsky. Whispering-gallery-bottle microcavities: the three-dimensional etalon. *Opt. Lett.*, 29(1):8–10, Jan 2004.

[73] Jon D. Swaim, Joachim Knittel, and Warwick P. Bowen. Detection limits in whispering gallery biosensors with plasmonic enhancement. *Appl. Phys. Lett.*, 99(24):243109, 2011.

[74] Jonathan Y. Lee, Xianshu Luo, and Andrew W. Poon. Reciprocal transmissions and asymmetric modal distributions in waveguide-coupled spiral-shaped microdisk resonators. *Opt. Express*, 15(22):14650–14666, Oct 2007.

[75] Xianshu Luo and Andrew W. Poon. Coupled spiral-shaped microdisk resonatorswith non-evanescent asymmetric inter-cavitycoupling. *Opt. Express*, 15(25):17313–17322, Dec 2007.

[76] A. Massaro, V. Errico, T. Stomeo, R. Cingolani, A. Salhi, A. Passaseo, and M. De Vittorio. 3-d fem modeling and fabrication of circular photonic crystal microcavity. *J. Lightwave Technol.*, 26(16):2960–2968, 2008.

[77] Alex Kaplan, Matthew Tomes, Tal Carmon, Maxim Kozlov, Oren Cohen, Guy Bartal, and Harald G. L. Schwefel. Finite element simulation of a perturbed axial-symmetric whispering-gallery mode and its use for intensity enhancement with a nanoparticle coupled to a microtoroid. *Opt. Express*, 21(12):14169–14180, Jun 2013.

[78] Xuan Du, Serge Vincent, and Tao Lu. Full-vectorial whispering-gallery-mode cavity analysis. *Opt. Express*, 21(19):22012–22022, Sep 2013.

[79] Jianwei Mu and Wei-Ping Huang. Simulation of three-dimensional waveguide discontinuities by a full-vector mode-matching method based on finite-difference schemes. *Opt. Express*, 16(22):18152–18163, Oct 2008.

[80] JianWei Mu. *Modal methods for modeling and simulation of photonic devices*. PhD thesis, McMaster University, 2011.

[81] J. Petracek and J. Luksch. Bidirectional eigenmode propagation algorithm for 3d waveguide structures. In *Transparent Optical Networks (ICTON), 2011 13th International Conference on*, pages 1–4, 2011.

[82] Rui Wang, Lin Han, Jianwei Mu, and Weiping Huang. Simulation of waveguide crossings and corners with complex mode-matching method. *Lightwave Technology, Journal of*, 30(12):1795–1801, 2012.

[83] P. Bienstman and R. Baets. Optical modelling of photonic crystals and vcsels using eigenmode expansion and perfectly matched layers. *Opt. Quantum. Electron.*, 33(4-5):327–341, 2001.

[84] Lifeng Li. Formulation and comparison of two recursive matrix algorithms for modeling layered diffraction gratings. *J. Opt. Soc. Am. A*, 13(5):1024–1035, May 1996.

[85] Lifeng Li. Multilayer modal method for diffraction gratings of arbitrary profile, depth, and permittivity. *J. Opt. Soc. Am. A*, 10(12):2581–2591, Dec 1993.

[86] DK Armani, TJ Kippenberg, SM Spillane, and KJ Vahala. Ultra-high-Q toroid microcavity on a chip. *Nature*, 421(6926):925–928, FEB 27 2003.

[87] Xiaoyan Ma, Jun Q Lu, R Scott Brock, Kenneth M Jacobs, Ping Yang, and Xin-Hua Hu. Determination of complex refractive index of polystyrene microspheres from 370 to 1610 nm. *Phys. Med. Biol.*, 48(24):4165, 2003.

[88] Michael Bass, Casimer DeCusatis, Jay Enoch, Vasudevan Lakshminarayanan, Guifang Li, Carolyn Macdonald, Virendra Mahajan, and Eric Van Stryland. *Handbook of Optics, Third Edition Volume I: Geometrical and Physical Optics, Polarized Light, Components and Instruments(Set)*. McGraw-Hill, Inc., New York, NY, USA, 3 edition, 2010.

[89] Andrea L. Martin, Deniz K. Armani, Lan Yang, and Kerry J. Vahala. Replica-molded high-q polymer microresonators. *Opt. Lett.*, 29(6):533–535, Mar 2004.

[90] L. F. Richardson. The approximate arithmetical solution by finite differences of physical problems involving differential equations, with an application to the stresses in a masonry dam. *Philosophical Transactions of the Royal Society of London. Series A, Containing Papers of a Mathematical or Physical Character*, 210:pp. 307–357, 1911.

[91] Lewis F. Richardson and J. Arthur Gaunt. The deferred approach to the limit. part i. single lattice. part ii. interpenetrating lattices. *Philosophical Transactions of the Royal Society of London. Series A, Containing Papers of a Mathematical or Physical Character*, 226(636-646):299–361, 1927.

Appendix A

Additional Information

A.1 Richardson Extrapolation

Richardson Extrapolation is a numerical technique to improve the rate of convergence of a sequence. It was first proposed by Lewis Fry Richardson in the early 20^{th} century [90, 91].

For example, in chapter 3, the wavelength shift calculated by the single mode-matching modal is only an approximation of the true value due to numerical errors. To investigate how the azimuthal grid spacing $\delta\phi$ affects the accuracy of the modal, we can express the calculated wavelength shift $\Delta\lambda$ as a function of the step size $\delta\phi$. For simplicity here we use $A(h)$ to express this function wherein A is the wavelength shift and h is the azimuthal grid spacing. Usually, a smaller grid spacing h gives an approximation $A(h)$ closer to its true value A (in other words, of better accuracy). To investigate such procedure quantitatively, the error formula is written as,

$$A = A(h) + K_0 h^k + K_1 h^{k+1} + K_2 h^{k+2} + ... \tag{A.1}$$

with k being a known constant and K_0, K_1, K_2, ... being some other constants. A.1 can be simplified by the big O notation. $O(h^{k+1})$ is used to stand for 'a sum of terms of orders h^{k+1} and higher',

$$A = A(h) + K_0 h^k + O(h^{k+1}) \tag{A.2}$$

We can get a second such equation by using a different step size $h/2$,

$$A = A(h/2) + K_0(h/2)^k + O(h^{k+1}) \tag{A.3}$$

Taking 2^k times A.3 and subtracting A.2 gives

$$A = \frac{2^k A(h/2) - A(h)}{2^k - 1} + O(h^{k+1}) \tag{A.4}$$

So if we define

$$B(h) = \frac{2^k A(h/2) - A(h)}{2^k - 1} \tag{A.5}$$

then

$$A = B(h) + O(h^{k+1}) \tag{A.6}$$

$B(h)$ is a new approximation scheme of A which has an error estimate on the order of $k + 1$, one better than $A(h)$'s. Moreover, the previous procedure can be repeated with $B(h)$ to get an even better approximation.

A.2 Mode Patterns of a WGM-nano particle Hybrid Mode

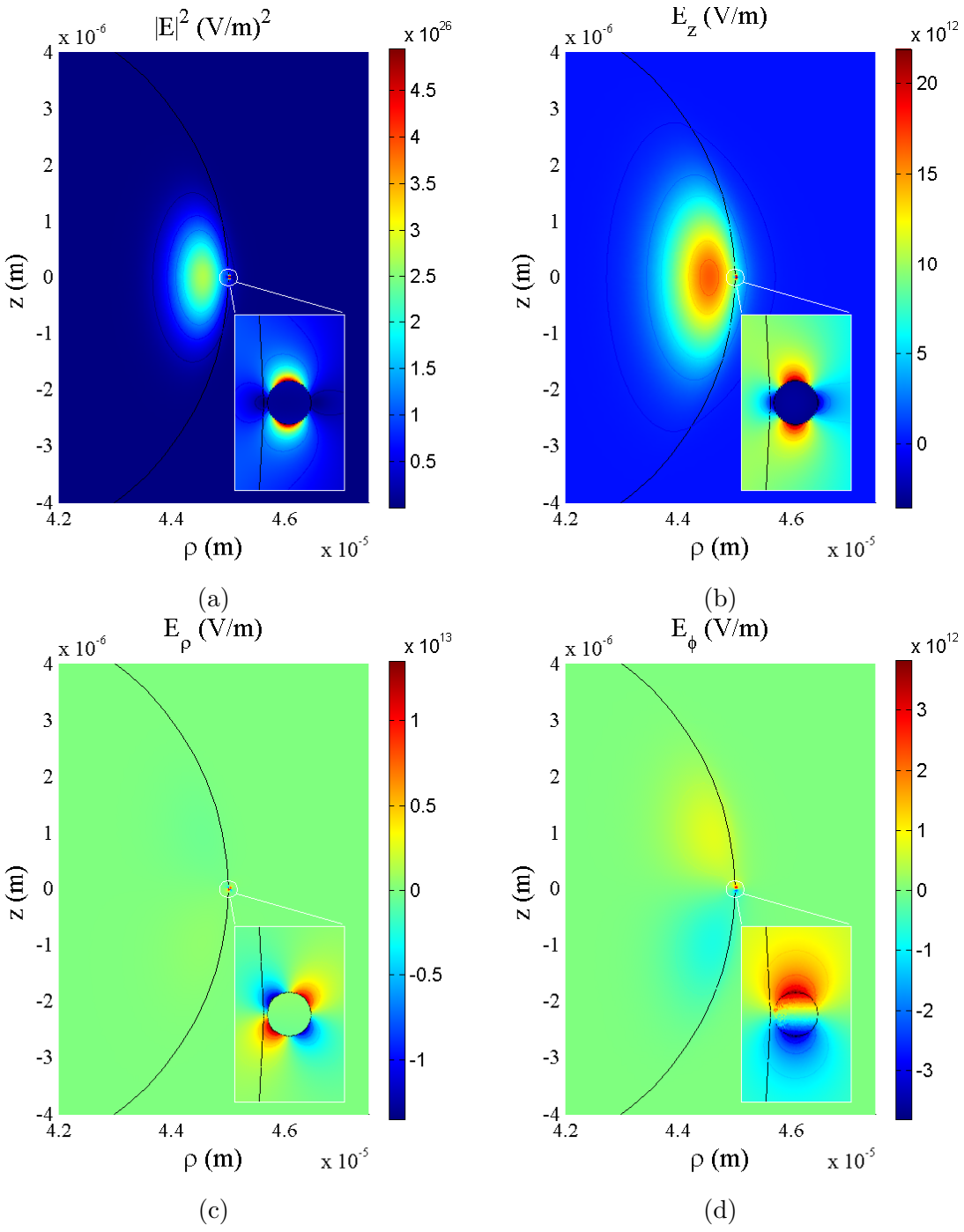

Figure A.1: The fundamental quasi-TE mode ((a) Electric field intensity $|\mathbf{E}|^2$, (b) axial electric field component E_z, (c) radial electric field component E_ρ, and (d) azimuthal electric field component E_ϕ) of a silica microtoroid with a gold bead bound to the equator at a 633-nm wavelength. The modes are plotted at the azimuthal cross section where the center of the bead is located. The insets provide a zoomed-in view of around the beads.

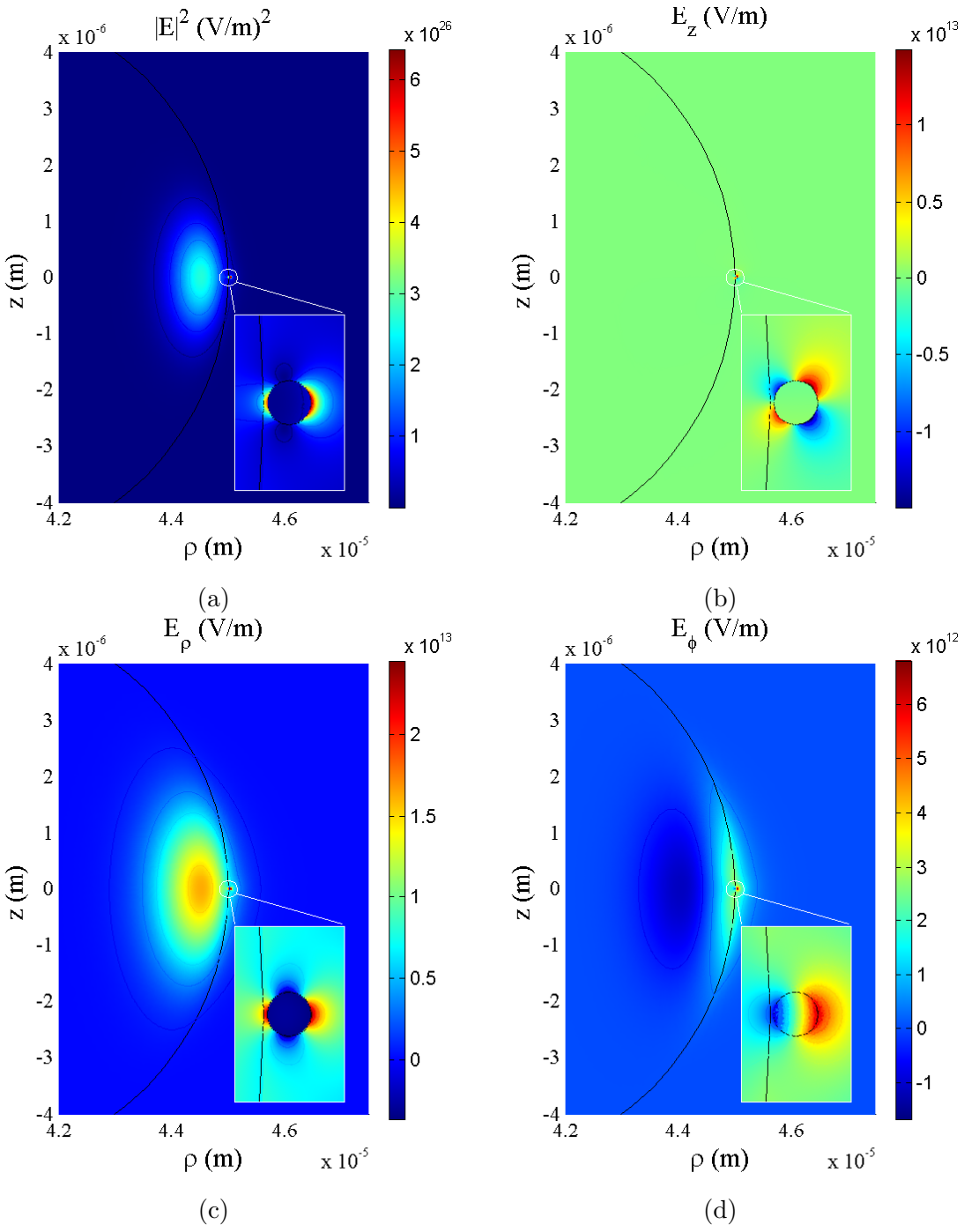

Figure A.2: The fundamental quasi-TM mode ((a) Electric field intensity $|\mathbf{E}|^2$, (b) axial electric field component E_z, (c) radial electric field component E_ρ, and (d) azimuthal electric field component E_ϕ) of a silica microtoroid with a gold bead bound to the equator at a 633-nm wavelength. The modes are plotted at the azimuthal cross section where the center of the bead is located. The insets provide a zoomed-in view of around the beads.

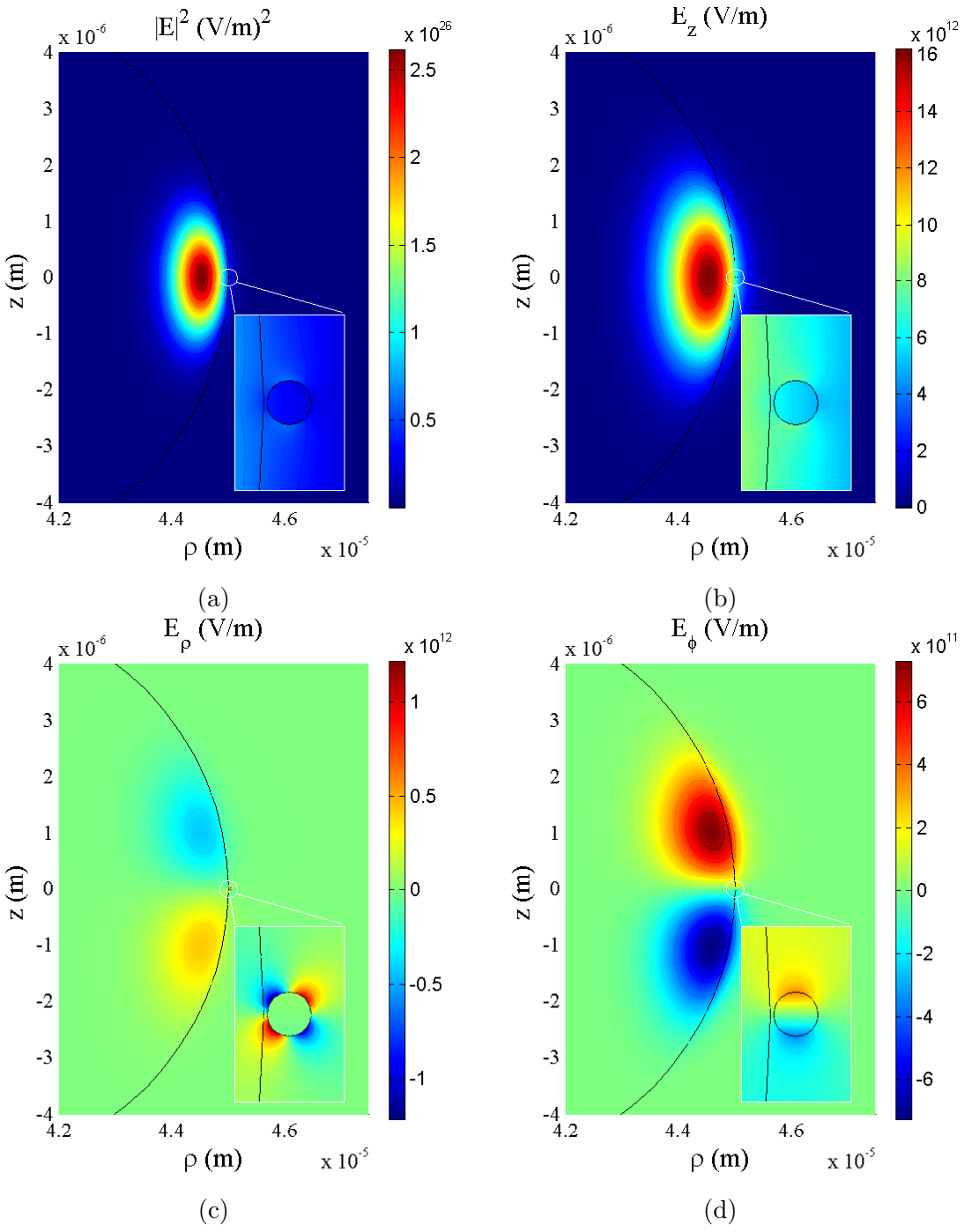

Figure A.3: The fundamental quasi-TE mode ((a) Electric field intensity $|\mathbf{E}|^2$, (b) axial electric field component E_z, (c) radial electric field component E_ρ, and (d) azimuthal electric field component E_ϕ) of a silica microtoroid with a PS bead bound to the equator at a 633-nm wavelength. The modes are plotted at the azimuthal cross section where the center of the bead is located. The insets provide a zoomed-in view of around the beads.

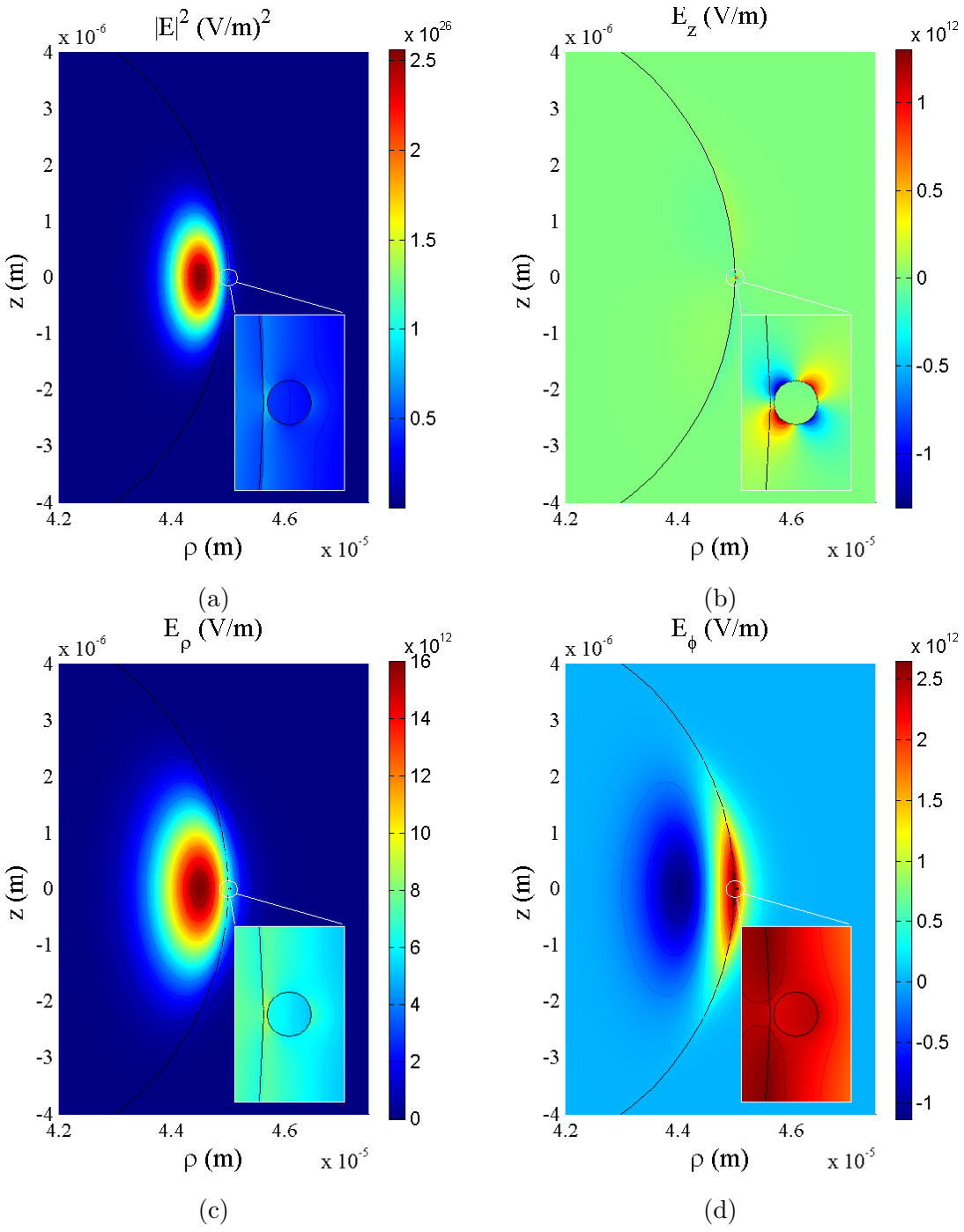

Figure A.4: The fundamental quasi-TM mode ((a) Electric field intensity $|\mathbf{E}|^2$, (b) axial electric field component E_z, (c) radial electric field component E_ρ, and (d) azimuthal electric field component E_ϕ) of a silica microtoroid with a PS bead bound to the equator at a 633-nm wavelength. The modes are plotted at the azimuthal cross section where the center of the bead is located. The insets provide a zoomed-in view of around the beads.